

PURDUE UNIVERSITY
GRADUATE SCHOOL
Thesis/Dissertation Acceptance

This is to certify that the thesis/dissertation prepared

By John D. Lorenz

Entitled

Formation of Deeply Bound LiRb Molecules via Photoassociation to Near Asymptotic States

For the degree of Doctor of Philosophy

Is approved by the final examining committee:

Daniel S. Elliott

Yong Chen

David Nolte

Francis Robicheaux

To the best of my knowledge and as understood by the student in the *Thesis/Dissertation Agreement, Publication Delay, and Certification/Disclaimer (Graduate School Form 32)*, this thesis/dissertation adheres to the provisions of Purdue University's "Policy on Integrity in Research" and the use of copyrighted material.

Daniel S. Elliott

Approved by Major Professor(s): _____

Approved by: Andrew S. Hirsch

06/24/14

Head of the Department Graduate Program

Date

FORMATION OF DEEPLY BOUND LIRB MOLECULES VIA
PHOTOASSOCIATION TO NEAR ASYMPTOTIC STATES

A Dissertation

Submitted to the Faculty

of

Purdue University

by

John D. Lorenz

In Partial Fulfillment of the

Requirements for the Degree

of

Doctor of Philosophy

August 2014

Purdue University

West Lafayette, Indiana

For Suzanne (and Mr. Porthouser)

ACKNOWLEDGMENTS

Thanks to all those who helped on this project. First and foremost, I'd like to thank the other graduate students who worked on creating the ultracold LiRb molecule in our group, Adeel Altaf and Sourav Dutta. I'd like to acknowledge the students working towards the next generation of ultracold LiRb work here at Purdue, Ian Stevenson and David Blasing. I'd also like to thank other graduate students that worked in our lab, Dionysios Antypas, and more recently Jungu Choi, and George Toh. Several undergrads have helped along the way including Roger Ding, Danny Barjum, Nadia Lustig, Kristen Brockway, and Bo Yuan. Of course the project would not have been possible with the help of my advisors Dan Elliott and Yong Chen. I must thank those who came before me, Art Mills, Rekishu Yamazaki, and Mevan Gunawardena. Art was especially generous with time and advice to help us navigate his old lab even after many years. Their help made it so that our project could succeed using the equipment available. Also, special thanks goes to Dan Leaird from Dr. Andrew Weiner's group. He set up and maintains the frequency comb used in these experiments, and has helped us with other equipment needs. He also generously helped run optical fiber between labs and has been a consultant for some of our optical fiber purchasing and cleaning needs.

I would also like to thank those closest to me, family and friends, some of whom may not have expected me to be here for so long. I even thank those friends, who, while they were comrades through the ordeal of graduate school, chose to selfishly graduate before I did. I thank those family members that finally learned to stop asking when I'd graduate, and even those who did not. Finally, I must thank the most important person, my wife Suzanne, who has supported me since long before we were married.

TABLE OF CONTENTS

	Page
LIST OF TABLES	vi
LIST OF FIGURES	vii
ABSTRACT	x
1 Experimental and Theoretical Interest in Cold Polar Molecules	1
1.1 Introduction	1
1.2 Ultracold Physics Beyond Atomic Samples	4
1.2.1 Photoassociation	5
1.2.2 Interactions Between Polar Molecules	8
1.2.3 Other Trapped Systems	10
1.3 Polar Molecules as a Medium for Quantum Computation	11
1.3.1 Qubits, Superposition States, and Entanglement	12
1.3.2 An AMO Quantum Computer: Using Polar Molecules as Qubits	15
1.4 Choice of LiRb for Study	18
2 Dual Species Magneto-optical Trap	21
2.1 Two-level Atoms in a Laser Field	22
2.2 Slowing Atoms Through Conservation of Momentum	23
2.3 Effects of Atomic Structure on Cooling and Trapping	27
2.3.1 One Dimensional MOT	27
2.3.2 Effect of ${}^7\text{Li}$ and ${}^{85}\text{Rb}$ Hyperfine Structure on MOT Operation	29
2.4 Temperature Limits	31
2.5 Capture Velocity and Loading Rates	33
2.6 Zeeman Slower	34
2.7 Dark SPOT	36
3 Experimental Setup	39
3.1 Cooling and Trapping Lasers	39
3.1.1 Frequency Stabilized Diode Lasers	43
3.1.2 Generating Repump Frequencies for Lithium	53
3.1.3 MOT Setup	60
3.2 Photoassociation Laser System	62
3.2.1 Frequency Comb Assisted Spectroscopy	64
3.3 Ionization Laser	65
3.4 Vacuum System and Ion Detection	66
3.5 Ion Counting Electronics	72

	Page	
3.5.1	Experimental Timing	74
3.5.2	Laser Scanning Control and Calibration	76
3.5.3	Accuracy of Ion Counting	79
3.6	Conclusion and Future Upgrades	81
4	Previous Theoretical and Experimental Results in LiRb	83
4.1	Correspondence between Hund's case (a) or (b) and Hund's case (c)	84
4.2	LiRb PECs: Theoretically and Experimentally Determined	86
4.3	Previous Photoassociation Results	90
4.4	Previous REMPI Results from PA to the $2(0^-)$ Potential	91
4.5	Calculations of LiRb ⁺ Potential	95
5	REMPI Spectra of the X ¹ Σ ⁺ State	97
5.1	Experimental Conditions and Resulting Spectra	97
5.1.1	REMPI scans	99
5.1.2	$v'' = 5$ Spectra and Choice of J	100
5.1.3	Molecular Potentials Involved in REMPI	105
5.2	X ¹ Σ ⁺ → D ¹ Π Transitions	105
5.3	X ¹ Σ ⁺ → B ¹ Π Transitions	114
5.4	X ¹ Σ ⁺ → C ¹ Σ ⁺ Transitions	119
5.5	Lack of Evidence for Observing Decay at Large Internuclear Separation	120
5.5.1	FCF Calculations Based on Spectra from Heat Pipe Results	122
5.5.2	Theoretical Properties of the $(4)^1\Sigma^+$ Potential	124
5.5.3	Observed Differences in REMPI Spectra from Different J states	125
5.6	Production Rates	128
5.7	Conclusion	129
6	Conclusion and Future Work	131
A	Electronic Transitions in Diatomic Molecules	139
A.1	Electronic States of Diatomic Molecules	140
A.2	Selection Rules for Electronic Transitions in Diatomic Molecules . .	141
A.2.1	Labeling of Electronic States	143
A.3	Vibrational Levels in Diatomic Molecules	144
A.3.1	Consideration of Vibrational Levels in Electronic Transitions	145
A.4	Hund's Coupling Cases	147
B	Observed and Calculated LiRb transitions	153
	LIST OF REFERENCES	165
	VITA	171

LIST OF TABLES

Table	Page
1.1 Research done on bialkali molecules.	19
2.1 Temperature limits for ${}^7\text{Li}$ and ${}^{85}\text{Rb}$	32
3.1 Frequency and power parameters for MOT lasers.	62
3.2 Comparison of ion counting methods.	80
4.1 Correspondence from Hund's case (a) or (b) to Hund's Case (c)	85
4.2 Observed vibrational levels in heat pipe experiments.	88
4.3 Summary of PA previous PA spectroscopy.	91
4.4 Calculations of $\text{LiRb}^+ \text{X}^2\Sigma^+$ potential	96
5.1 PA resonances used for REMPI scans.	98
A.1 Hund's Coupling Cases.	149
A.2 Molecular transition selection rules.	151
B.1 Possible one color REMPI transitions sorted by progression (Part I) . .	156
B.2 Possible one color REMPI transitions sorted by progression (Part II) .	157
B.3 Possible one color REMPI transitions sorted by energy (Part I)	158
B.4 Possible one color REMPI transitions sorted by energy (Part II)	159
B.5 Observed lines and assignments (Part I)	160
B.6 Observed lines and assignments (Part II)	161
B.7 Observed lines and assignments (Part III)	162
B.8 Observed lines and assignments (Part IV)	163
B.9 Observed lines and assignments (Part V)	164
B.10 Observed progressions in REMPI spectra	164

LIST OF FIGURES

Figure	Page
1.1 PA in LiRb	7
1.2 Four different cases of dipole-dipole interactions.	9
1.3 DeMille's quantum computation scheme using polar molecules.	17
2.1 Spontaneous force vs. Detuning for $s_0 = 1, 10, \text{ and } 50$	25
2.2 Population vs. Doppler shift based on the Maxwell-Boltzmann distribution at 300 K for Li and Rb.	26
2.3 Model for 1D MOT	29
2.4 The energy levels of ^{85}Rb and ^7Li	30
2.5 Dark MOT vs. normal MOT operation	37
3.1 Diagram of the atomic cool and trapping laser system	40
3.2 Saturated Absorption schemes.	44
3.3 Saturated absorption spectra for ^{85}Rb and ^{87}Rb	45
3.4 Locking signals for ^{85}Rb MOT repump and trapping lasers	47
3.5 ^{87}Rb $F = 1$ transitions	48
3.6 Li MOT frequencies	50
3.7 AOM Control Circuit	51
3.8 Generating Li trapping and repump frequencies via injection locking	59
3.9 Schematic of MOT optics	61
3.10 Measuring PA laser frequency	63
3.11 Schematic of vacuum system	67
3.12 Photo of vacuum system	68
3.13 Atom cloud over field plate	69
3.14 Arrival of ions to the MCPs	71
3.15 Ion counting electronics	73

Figure	Page
3.16 Experimental timing signals	77
4.1 Long Range potentials for LiRb	87
4.2 Diabatic PECs for LiRb	89
4.3 REMPI from $v'' = 5$ of the $2(0^-)$	93
4.4 Autocorrelation functions of $2(0^-)$ REMPI spectra	94
5.1 REMPI spectra for PA to the $v' = 3, J = 2$ level of the $4(1)$ state . . .	101
5.2 REMPI spectra for PA to the $v' = 4, J = 1$ level of the $4(1)$ state . . .	102
5.3 REMPI spectra for PA to the $v' = 5, J = 1$ level of the $4(1)$ state . . .	103
5.4 Normalized REMPI scans	104
5.5 REMPI Pathways	106
5.6 Autocorrelation function for $X^1\Sigma^+$ REMPI scans	107
5.7 Vibration level spacing in the $D^1\Pi$ potential.	108
5.8 $v'' = 15$ transitions to $D^1\Pi$	110
5.9 $v'' = 7, 9-13$ transitions to $D^1\Pi$	111
5.10 $v'' = 14, 15, 17, 19, 20, 21$ transitions to $D^1\Pi$	112
5.11 Progressions from the $X^1\Sigma^+$ to $D^1\Pi$ not seen in spectra	115
5.12 Vibration level spacing in the $B^1\Pi$ potential.	116
5.13 Transitions to $B^1\Pi$ states	118
5.14 Vibration level spacing in the $C^1\Sigma^+$ potential.	120
5.15 Transitions to $C^1\Sigma^+$ states	121
5.16 FCFs between $B^1\Pi$ and $X^1\Sigma^+$ potentials	123
5.17 Vibration level spacing in the $(4)^1\Sigma^+$ potential.	125
5.18 Differences in spectra depending on J state of PA to the $4(1)$ potential	127
5.19 Differences in PA spectra depends on REMPI frequency	128
6.1 PA to $v' = 6$ or the $4(1)$ potential	133
6.2 Depletion spectroscopy schematic	134
6.3 Population transfer via STIRAP and Pump-Dump	136

Figure	Page
6.4 Possible population transfer via a two step STIRAP process for LiRb rovibrational ground state.	137
A.1 Schematic representation of Franck-Condon factors.	146

ABSTRACT

Lorenz, John D. Ph.D., Purdue University, August 2014. Formation of Deeply Bound LiRb Molecules via Photoassociation to Near Asymptotic States. Major Professors: Daniel S. Elliott and Yong P. Chen.

We present the results of a spectroscopic study LiRb molecules created via photoassociation (PA) to vibration levels of the $4(1)$ potential. Atoms are first cooled and trapped in a dual species ${}^7\text{Li}/{}^{85}\text{Rb}$ magneto-optical trap (MOT) at temperatures of ≈ 1 mK or less. In a cold sample of sufficient density, PA occurs when a resonant laser field induces a free-bound transition to create molecules in an excited electronic potential. After spontaneous emission the molecules decay to a mixture of free atoms and bound molecules depending on the Franck-Condon factors (FCFs) of the excited and ground state vibrational wavefunctions. While excited LiRb^* has been previously detected by trap loss fluorescence detection, ionization spectroscopy is required to determine the population of ground state levels after decay. We present evidence that molecules formed by PA to vibrational levels near the $\text{Li } 2\text{S}_{1/2} + \text{Rb } 5\text{P}_{3/2}$ asymptote decay to deeply bound vibrational levels. We use PA to form LiRb^* in states of the $4(1)$ potential (corresponding to the $\text{B}^1\Pi$ at close range) which then decay to levels of the $\text{X}^1\Sigma^+$ potential. We detect ground state molecules via resonantly enhanced multiphoton ionization (REMPI) where a two photon ionization transition is enhanced by an intermediate resonance. The intermediate resonances match progressions from the $\text{D}^1\Pi$ and possibly $\text{B}^1\Pi$ potentials, many of which have known energies obtained from previous heat pipe experiments. This is contrary to the expectation that weakly bound LiRb^* should primarily decay to weakly bound levels of the ground state and could point to a possible path for creating molecules in the rovibronic ground state.

1. Experimental and Theoretical Interest in Cold Polar Molecules

1.1 Introduction

In atomic, molecular, and optical (AMO) physics, the experimental trend since the advent of atomic laser cooling and trapping techniques (for which Cohen-Tannoudji, Chu, and Phillips won a Nobel Prize in 1997) is to study colder and more highly controlled systems. To achieve cold temperatures in solid state systems, one would usually rely on a dilution refrigerator to achieve mK temperatures. Spin systems can be cooled to μK temperature through magnetic refrigeration. Laser cooling can, in general, cool atomic systems to μK temperatures, much faster and much cheaper than the previously mentioned refrigeration techniques. Evaporative cooling techniques further lowered achievable temperatures to the nK range as experiments began to produce quantum degenerate systems (for which Wieman, Ketterle, and Cornell won a Nobel Prize in 2001).

The main advantage of ultracold atomic systems is they provide a very clean system in which to perform measurements. Atomic structure has been very well studied and interactions between atoms and fields and atoms and other atoms are quite well understood. Such systems are ideal for making precision measurements. The level of control over such systems by external fields has developed to the point that they have been proposed as building blocks for quantum information and quantum computation as well as the study of quantum phase transitions, quantum gas dynamics, and to simulate the quantum mechanical nature of other systems, including condensed matter systems, relativistic particles, and even astrophysical phenomena. The behavior for a variety of systems can be mapped onto atomic systems by engineering the

appropriate Hamiltonian, allowing exotic phenomena to be observed from a table top AMO experiment that can be cleanly controlled and measured.

Recent interest in using cold polar molecules in these systems instead of atoms has developed [1–37]. Polar molecules have long range anisotropic interactions that had not been studied in a trapped ultracold environment until recent work. Production of ultracold heteronuclear molecules has led to the study of chemistry in new temperature regimes and the investigation of controlled reactions at low temperatures [23]. There are experiments that seek to use the permanent electric dipole moment (EDM) of polar molecules to perform precision measurements of fundamental constants, time variation of fundamental constants, permanent dipole moments of fundamental particles and to explore parity violation in these systems [1]. Most experiments to date have dealt with merely the creation and trapping of cold polar molecules, which compared to free atoms have quite a complicated quantum structure. Once the structure of the molecules is well understood, population can be transferred to the absolute rovibronic (rotational, vibrational, electronic) ground state where the physics of this novel system is best explored [6,21]. Proposed experiments seek to take advantage of the dipole-dipole interactions and the extra degrees of freedom (vibrational/rotation) that molecules have [11]. These same extra degrees of freedom that make polar molecules interesting, also make them difficult to cool and trap.

This thesis covers our work in producing ultracold heteronuclear molecules from a mixture of ${}^7\text{Li}$ and ${}^{85}\text{Rb}$ via photoassociation (PA). Until recently, ultracold LiRb had not yet been observed [12,13] nor had much spectroscopy been done to study the structure of the molecule [38–40]. To use polar molecules as a means of exploring the physics previously noted requires the molecules to be prepared in a long lived quantum state. This means that the first step towards using polar molecules to explore new physics is to find a way to create samples in the rovibronic ground state ($v'' = 0, J'' = 0$ of the ground electronic potential). The dipole moment of a molecule also depends on its vibrational state and increases for lower v'' , where the internuclear

separation is smaller. Thus, the effect of dipole-dipole interactions is strongest when molecules are in the vibrational ground state.

We first examine the motivating factors for the study of cold polar molecules. In this introductory chapter, we present an overview of ultracold atomic and molecular systems, how to create cold molecules, and the properties of polar molecules that should give rise to new physics. A very brief primer on quantum computation is given along with a proposed scheme for using polar molecules as qubits. Finally, we present our rationale for choosing LiRb for investigation.

In Chapter 2, we present the theory behind a magneto-optical trap (MOT), the experimental tool for creating a cold sample of trapped atoms. We require a dual species MOT to create heteronuclear molecules via PA. In Chapter 3, we give an overview of the experimental system we use to create molecules via PA, which we have detected either through trap loss or ion detection. Chapter 4 summarizes the theoretical and experimental results that have informed the interpretation of new data, which we present in Chapter 5. We present new LiRb spectra taken using resonantly enhanced multiphoton ionization (REMPI). These spectra show evidence of population in deeply bound vibration states of the ground $X^1\Sigma^+$ electronic potential after molecules spontaneously decay from weakly bound states in the $4(1)$ potential formed via PA. The concluding chapter gives possible directions for future work that could lead to production of LiRb molecules in the rovibronic ground state.

Background theory of diatomic molecules required for this thesis (selection rules, Frank-Condon factors, Hund's coupling cases, etc.) can be found in Appendix A. Appendix B is a collection of tables of the assignments made to spectral lines and other data to aid in the interpretation of the observed spectra presented in Chapter 5.

1.2 Ultracold Physics Beyond Atomic Samples

Most experiments of current interest in AMO physics requires that atomic or molecular samples be prepared into a specific quantum state. In general, this requires that the state be long lived and that the atoms or molecules be ultracold. Until recently, LiRb had only been formed at high temperatures in heat pipe experiments [38–40]. High temperatures are needed to raise the vapor pressure of the atomic species, especially lithium [41], and produce inelastic three body collisions that can result in molecular formation. However, high temperature systems are not desirable for a number of reasons. For example, resolution of spectral lines is limited by large Doppler broadening. Spectroscopic techniques have been developed to reduce motional effects. Counterpropagating beam geometries can be used to probe only atoms or molecules with zero longitudinal velocity to eliminate Doppler broadening. Collimated atomic or molecular beams can be probed nearly Doppler free with a perpendicular beam as velocities in transverse directions should be minimal. To solve the problem of minimizing motion in all three dimensions, laser cooling and trapping techniques were developed for atomic systems.

Most laser cooling and trapping from high temperatures down to the μK regime relies on the simple principle of conservation of momentum. As we discuss in greater detail in Chapter 2, atoms can preferentially absorb photons from a laser while travelling in the direction opposite beam propagation by detuning the frequency of the light to the red of an atomic transition. Such preferential absorption means the atom will be slowed as it travels into the laser beam as the momentum of the photons is transferred to the atom. Recoil momentum due to spontaneous emission averages to zero due to its random isotropic nature. This is the mechanism behind optical molasses and magneto-optical traps which have been successful in creating dense ultracold samples of various atomic species for several decades [42–52]. Cooling beyond the Doppler limit in MOTs can be achieved through Sisyphus or polarization-gradient cooling [43]. Even further cooling can be done by evaporative means using magnetic

traps for paramagnetic species or optical dipole traps — as the trap depth is lowered allowing the hottest atoms to leave the sample. This has allowed for cooling all the way nK temperatures, which results in a quantum degeneracy for a sufficiently dense trap.

While techniques to cool, trap, and study atomic samples are well established, they rely on the relatively simple energy structure of atoms. Only a fraction of atomic species can be cooled and trapped with lasers and alkali metals are used in most experiments involving laser cooling. Alkali metals have a single valence electron and a simple hydrogen-like energy structure. While cold atoms have been the basis for many AMO physics experiments, ground state neutral atoms are usually very weakly interacting systems. They essentially only experience collisional interactions through van der Waals forces. The potential for these types of interactions is proportional to $1/r^6$ for heteronuclear collisions and $1/r^3$ for homonuclear collisions, where r is the internuclear spacing [35]. The interactions are also isotropic so atomic orientation has no meaning in a field-free environment, reducing the number of degrees of freedom that can be explored. Despite the weak strength of these interactions, many atoms can be readily trapped, and a cold dense sample of one or more atomic species is usually the starting point for most experiments in the ultracold regime. The primary method that has been used to create ultracold molecules is to start with a sample of ultracold atoms and to use a laser or magnetic field to bind them into ultracold molecules.

1.2.1 Photoassociation

While some research has been done into direct cooling and trapping of molecules [28,29], so far the most effective method of creating ultracold molecules has been to start with a sample of ultracold atoms. PA is a method of creating molecules during the process of an ultracold collision. At high temperatures diatomic molecules are normally created by three body collisions. Conserving momentum and energy while

creating a bound molecule is impossible for a two body collision. A third particle must be introduced to carry away the binding energy. In cold systems, these three body collisions are negligible and creating a sample of bound dimers requires a different method of removing the binding energy during the collision.

Photoassociation binds ultracold atoms into molecules by using a laser field with photon energy $\hbar\omega_1$ to induce a molecular transition from a scattering state (two unbound atoms) to an electronically excited but bound molecular state. If the spontaneous emission photon energy, $\hbar\omega_2$, upon decay is such that $\hbar\omega_2 \leq \hbar\omega_1$, then the molecule decays back into an unbound scattering state. There is, however, a significant chance that on decay $\hbar\omega_2 > \hbar\omega_1$ in which case it decays to a bound state. The scattered photon carries away the binding energy of the molecule. Note that PA relies on the molecules being ultracold. The initial energy state needs to be nearly equal to the atomic asymptote of the molecular state, which is the state of unbound atoms with no kinetic energy. Higher temperatures cause only an insignificantly small number of atoms to collide at near zero temperatures that have significant wavefunction overlap (also known as the Franck-Condon factor) between scattering states and bound states. The first evidence of PA was seen in 1991 in a system of ultracold Na [53], with other homonuclear species created in the years following. Later, once multispecies traps were developed, studies began on heteronuclear molecules [54]. Our PA route is shown in figure 1.1. A PA transition is evidenced through a loss of population in the atomic trap because the trap is species specific. Evidence of decay to a bound state requires observing transitions from the final bound state after decay — we accomplish this through resonantly enhanced multiphoton ionization (REMPI).

We briefly note a second way to bind ultracold molecules, called magnetoassociation (MA). MA relies on Feshbach resonances, a resonance that occurs when a bound state is degenerate with an unbound state [56]. For cold atoms, a magnetic field can be used to shift the Zeeman levels of the atoms so that they can collide along an unbound channel, but the degeneracy with a bound channel created by the Zeeman shifting creates a pseudobound molecule. Slowly ramping the magnetic field back to

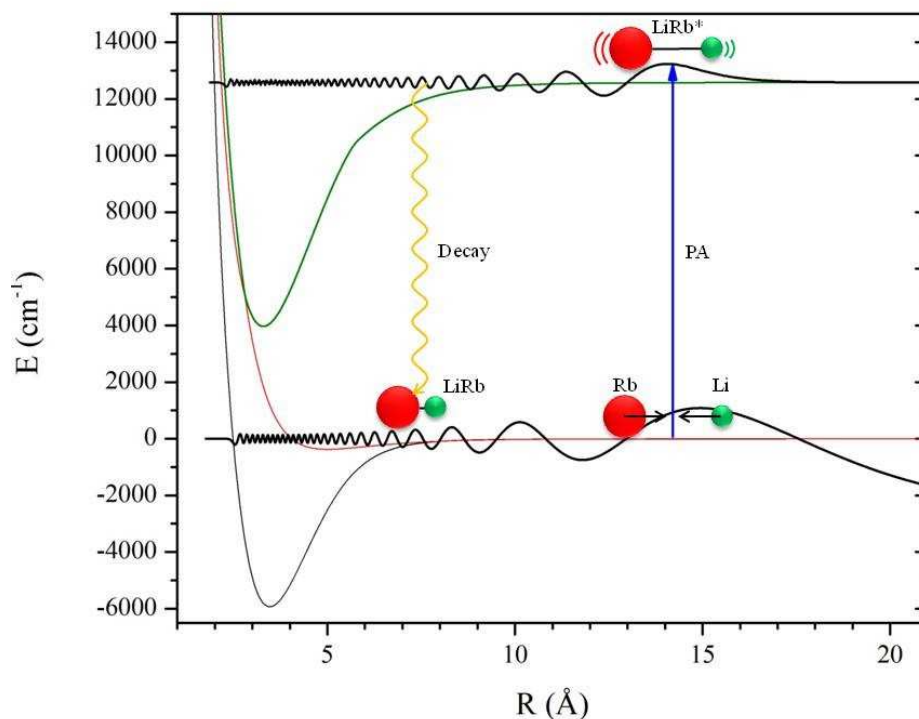


Figure 1.1. PA in LiRb. Li and Rb collide along the ground state atomic asymptote. When a PA laser field is present, it can be excited to a bound molecular state that has sufficient wavefunction overlap. One decay path is back to ground state molecules which can be detected by REMPI. Figure adapted from Adeel Altaf's thesis [55]. Wavefunction calculations courtesy of Jesús Pérez-Ríos.

zero adiabatically transfers the molecules into the least bound vibrational state of the molecule [21]. MA is generally done in quantum degenerate samples of gases at lower temperatures than would be required for PA and an optical pathway similar to PA is required to transfer population to more deeply bound molecules. The advantage is that all the sample of molecules are all created in the same quantum state, whereas the spontaneous emission from PA populates a variety of levels based on the allowed transitions. For previously unstudied molecules like LiRb, allowing the molecules to decay via spontaneous emission gives a picture of the transition strength between

states by looking at the population of vibrational states after decay, which can be valuable information.

Because electronic transitions are vertical, (The transition is assumed to be instantaneous meaning the position and momentum of the nuclei is assumed to remain unchanged during the transition — see A.3.1.) PA occurs at internuclear spacings within the classical outer turning point of the excited molecular potential, generally $< 40a_0$. This means the PA rate will depend upon the average spacing between nuclei and thus the densities each of the atomic species being bound together to form dimers. Feshbach resonances can also be used to enhance PA because the pseudobound states formed by Feshbach resonances spend more time at close internuclear spacing [24].

1.2.2 Interactions Between Polar Molecules

The energy of dipole-dipole interactions between polar molecules is:

$$E_{\text{dd}} = \frac{\vec{p}_1 \cdot \vec{p}_2 - 3(\hat{r} \cdot \vec{p}_1)(\hat{r} \cdot \vec{p}_2)}{4\pi\epsilon_0|\vec{r}|^3} \quad (1.1)$$

where \vec{p}_1 and \vec{p}_2 are the dipole moments of the molecules, \vec{r} is the relative position vector between the two dipoles, and $\hat{r} = \vec{r}/|\vec{r}|$, the unit vector in the direction of \vec{r} [57]. There are several important characteristics of this interaction that should be noted. The strength of the interaction scales as $1/r^3$, the same scale as homonuclear van der Waals interactions, but with a much larger proportionality constant. The interaction also depends on the relative orientation of the dipoles. This makes relative *alignment* and *orientation* important parameters in a system of interacting dipoles.

Alignment is defined by the angle between molecular axes. As polar molecules evolve and rotate, quantum mechanically the alignment of a molecular ensemble can be expressed in terms of $\langle \cos^2 \theta \rangle$ where θ is the angle of the molecular axis with respect to an external field. In theory, this field can be the electric field due to an adjacent dipole. However, in practice, experiments have measured θ in macroscopic samples with respect to an applied electric field or laser polarization axis. In these studies, $\langle \cos^2 \theta \rangle = 1$ indicates perfect alignment of molecules while $\langle \cos^2 \theta \rangle = 1/3$ implies

random alignment. For random alignment the probability distribution $P(\theta) = 1/4\pi$ so the average value of $1/3$ comes from

$$\langle \cos^2 \theta \rangle = \int P(\theta) \cos^2 \theta d\Omega = \frac{1}{4\pi} \int \cos^2 \theta d(\cos \theta) d\phi = \left[\frac{1}{4\pi} \frac{\cos^3 \theta}{3} 2\pi \right]_{\cos \theta = -1}^1 = 1/3.$$

Orientation accounts for the directions the dipole moment is pointing, and is given by $\langle \cos \theta \rangle$, which can vary between -1 and 1. Classically, parallel dipoles are aligned and have the same orientation. The quantum description for this situation would be $\langle \cos^2 \theta \rangle = 1$ and $\langle \cos \theta \rangle = 1$. Antiparallel dipoles are still be aligned, but have opposite orientation, which is described quantum mechanically as $\langle \cos^2 \theta \rangle = 1$ and $\langle \cos \theta \rangle = -1$. There have been a variety of studies on various methods to control the orientation and alignment of polar molecules [58–61].

Finally, dipole-dipole interactions are also anisotropic. Not only does E_{dd} depend on how the dipoles are aligned and oriented, but also on the relative position of them. If their dipole moments of molecules with the same orientation are perpendicular to the line between them, they will experience a repulsive force. If they are parallel to the line, they will experience an attractive force (see figure 1.2).

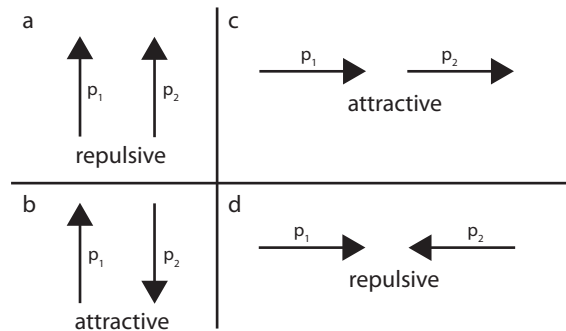


Figure 1.2. Four different cases of dipole-dipole interactions. The unit relative position vector, \hat{r} , is not pictured, but points from one dipole to another. a) The dipoles are aligned and perpendicular to \hat{r} , repelling each other. b) The dipoles are anti-aligned and perpendicular to \hat{r} , attracting each other. c) The dipoles are aligned and parallel to \hat{r} , attracting each other. d) The dipoles are anti-aligned and parallel to \hat{r} , repelling each other.

These aspects of dipole-dipole interactions allow degrees of freedom that cannot be achieved in atomic systems and gives rise to new physics in the ultracold regime. Just like atoms, polar molecules will be either fermions or bosons, and provided the molecular system is cold and dense enough, molecules could be cooled to a degenerate Fermi gas or BEC depending on the species. The behavior and stability of a polar BEC should be very different from an atomic BEC. For instance, dipole interactions will make 3D BECs unstable. Polar molecules loaded into optical lattices will go beyond the Bose-Hubbard model and give rise to exotic new phases of matter such as supersolids and quantum liquid crystals [62]. Control of alignment and orientation could be used to control interactions in these systems and has been proposed as a means of creating a scalable quantum computer (section 1.3).

1.2.3 Other Trapped Systems

There are other avenues for studying long range interacting cold particles beyond polar molecules. Atoms, especially rare earth elements, can have a permanent magnetic dipole moment, and the potential energy between magnetic dipoles has the same form as the electric dipole-dipole interaction:

$$E_{\text{dd,magnetic}} = \frac{\mu_0}{4\pi} \frac{\vec{m}_1 \cdot \vec{m}_2 - 3(\hat{r} \cdot \vec{m}_1)(\hat{r} \cdot \vec{m}_2)}{|\vec{r}|^3} \quad (1.2)$$

Until recently, these atoms had not been cooled or trapped. However, a dysprosium MOT and BEC has been recently achieved [62]. Such magnetic dipole systems could be used in place of electric dipole systems to simulate some of the same physics. Generally, interactions between electric dipoles are stronger by a few orders of magnitude, making them more desirable for situations requiring strongly interacting particles.

Trapped ions can also be used as a controlled interacting system. Ions can be trapped in harmonic electrostatic traps. Laser sideband cooling can be used to drive ions into the ground state of these traps [63]. Methods have been developed to control interactions with nearby ions. Like atoms, these interactions are isotropic. The interaction between ions is given by Coulomb's Law, which has a $1/r$ potential.

Ions repel each other strongly, making it difficult to use them for many-body problems. But, this strong interaction presents both challenges and benefits; single ions are easier to manipulate and measure. There has been some success in using them as qubits for quantum computation because of the relative ease of controlling their interactions [64]. However, the strong interactions of ions has made scalability from small to large numbers of qubits an issue thus far.

1.3 Polar Molecules as a Medium for Quantum Computation

In 1982, Richard Feynman proposed a Universal Quantum Simulator, which relies not only on being able to manipulate the quantum state of a system, but to use short range interactions to simulate a many-particle system [65]. In essence, this is an effort to gain not only experimental control over the state of a quantum system, but also the Hamiltonian governing its evolution. These ideas were further developed by David Deutsch and others into the field of Quantum Computation which relies on interacting two-state quantum systems called qubits to store and process information [66]. It has been shown that quantum computers hold the capability to perform tasks exponentially faster than is possible with classical algorithms [66,67]. However, to date, only small scale (on the order of 10 qubits through NMR techniques) implementations of quantum computation schemes have been achieved [68].

The first quantum computing algorithm was developed by Deutsch in 1992 [66]. His algorithm determined whether a function, $f(x)$, that acted on a qubit was constant — that is to see whether $f(0) = f(1)$. The algorithm required only a single measurement of a qubit, whereas a classical algorithm would be required to make two measurements — to check both $f(0)$ and $f(1)$. This seemingly trivial triumph of quantum mechanics demonstrated how superposition states of qubits could process outcomes in parallel, gaining a computational advantage over classical methods. In time, more complex (and useful) quantum algorithms were developed. The Grover search algorithm can search an unsorted list of length N in $\sqrt{N} \ln N$ steps where

it would take on average $\frac{N}{2}$ steps classically [69]. Perhaps the most well known algorithm in quantum computation is Shor’s Algorithm, which can factor numbers in exponentially fewer steps than classical factoring algorithms [67]. These algorithms exploit unique quantum properties such as interference and entanglement that have no classical analog. We will not examine any quantum algorithms in detail, but rather focus on the building blocks of quantum computation and demonstrate why polar molecules may be an attractive system for realizing operations on large numbers of qubits.

1.3.1 Qubits, Superposition States, and Entanglement

Bits are the building blocks of classical computing. A bit is simply a system which can exist in two states — commonly represented as 1 and 0. Quantum computation is based on quantum bits, or qubits — a two level system represented in Dirac notation as $|1\rangle$ and $|0\rangle$. The fundamental difference between bits and qubits is the ability of a quantum system to exist in a superposition state:

$$|\Psi\rangle = \alpha|0\rangle + \beta|1\rangle \tag{1.3}$$

where α and β are complex numbers such that $|\alpha|^2 + |\beta|^2 = 1$. Since the qubit can have characteristics of the $|0\rangle$ and $|1\rangle$ simultaneously, the information contained in each state can be processed in parallel, resulting in large computational gains over classical methods. However, it should be noted that not all problems are well suited for a quantum computational approach and a physically realized quantum computer would not replace transistor based computers.

Rather than using arbitrary complex numbers α and β , superposition states are often defined in the following manner:

$$|\Psi\rangle = \cos \frac{\theta}{2} |0\rangle + e^{i\phi} \sin \frac{\theta}{2} |1\rangle \tag{1.4}$$

where θ defines the amplitude of each state and ϕ defines the phase relationship between them. Written in this manner, a qubit can be represented by a point on a

unit sphere, usually called a Bloch sphere for a two level quantum system. The polar angle is given by θ and the azimuthal angle by ϕ . Defining qubits in this manner is also convenient because superposition states created through Rabi oscillations will take this form [63]. Rabi oscillations occur in a variety of two level systems. Examples include spin 1/2 particles in a rotating B-field or a two level atom or molecule in an oscillating electromagnetic field. For the special case where the external field is resonant with the energy spacing between the two states, the population will be coherently driven from one state to the other and back, oscillating as a function of time of interaction. In this case, modifying equation (1.4) to be time dependent

$$|\Psi(t)\rangle = \cos\left(\frac{\Omega t}{2}\right) |0\rangle + \sin\left(\frac{\Omega t}{2}\right) |1\rangle \quad (1.5)$$

where $\theta = \Omega t$ describes the time evolution a system undergoing Rabi oscillations starting from the initial state $|\Psi(0)\rangle = |0\rangle$. The Rabi frequency, Ω is a controllable parameter that depends on the amplitude and detuning of an oscillating external field. The phase, ϕ is usually only important in that the phase relationship stays fixed, which is the case for 1.5. Thus, an arbitrary point on the Bloch sphere can be chosen for a qubit by controlling the length of time the Rabi oscillations are allowed to occur. This unitary transformation is often represented graphically by the rotation of a vector on the Bloch sphere [69].

The other important aspect of quantum computation is entanglement, which is achieved through a controlled NOT (cNOT) gate. Consider the tensor product between two qubits $|x\rangle = \frac{1}{\sqrt{2}}(|0\rangle + |1\rangle)$ and $|y\rangle = |0\rangle$. The wavefunction for this two qubit state is

$$|\psi\rangle = |x\rangle \otimes |y\rangle = \frac{1}{\sqrt{2}}(|0\rangle + |1\rangle) \otimes |0\rangle = \frac{1}{\sqrt{2}}(|00\rangle + |10\rangle). \quad (1.6)$$

This is known as a disentangled state because the wavefunction can be factored into separable qubit states. This is always the case when qubits are non-interacting. The cNOT gate is the fundamental means of interaction in quantum computation. A cNOT gate is an operator that acts on two qubits. The first qubit (which is always

left unchanged) is the control qubit. The value of the second qubit is changed if the control qubit is $|1\rangle$ and is left unchanged if the control qubit is $|0\rangle$. In the basis $\{|00\rangle, |01\rangle, |10\rangle, |11\rangle\}$, the cNOT gate is represented by the 4×4 matrix

$$\text{cNOT} = \begin{pmatrix} 1 & 0 & 0 & 0 \\ 0 & 1 & 0 & 0 \\ 0 & 0 & 0 & 1 \\ 0 & 0 & 1 & 0 \end{pmatrix} = \begin{pmatrix} I & 0 \\ 0 & \sigma_x \end{pmatrix} \quad (1.7)$$

The cNOT gate acting on the two qubit state from equation (1.6) will give

$$\text{cNOT}|\psi\rangle = \frac{1}{\sqrt{2}}(|00\rangle + |11\rangle). \quad (1.8)$$

This new state is entangled — it can no longer be factored into the tensor product of two separate qubit states. Entanglement is also a uniquely quantum phenomenon. Measurement of the state of one qubit gives the state of both qubits simultaneously. Entanglement was one of Einstein's chief objections to quantum theory — two entangled qubits can be arbitrarily far apart and a measurement on one qubit can collapse the entangled wavefunction, meaning information can seemingly be instantly gained on an entangled particle arbitrarily far away. Einstein called this spooky action at a distance. However, this has not been shown to violate locality as no information is actually transmitted by collapsing a wavefunction. Still, entangled quantum states have been an important area of research, resulting in novel applications such as quantum teleportation. In quantum computation, it has been proved that any unitary operation on N qubits can be decomposed into a product of cNOT gates and unitary transformations on single qubits. Transformations on one qubit can be achieved through Rabi oscillations or other well established means. Thus, what is required for a viable quantum computer (neglecting issues of decoherence) is the ability to realize a cNOT gate.

1.3.2 An AMO Quantum Computer: Using Polar Molecules as Qubits

Physically realizing a quantum computer has been a goal ever since its theoretical computational power was realized. The main difficulty is creating a system where the qubits interact strongly enough with each other to realize cNOT gates, but that will not interact with the surrounding environment. Interactions with the environment cause decoherence, which destroys the essential correlations and phase relationships between qubits. Quantum computation has been proposed (and occasionally achieved) in a number of systems including NMR [68], condensed matter [70] and AMO systems. In AMO physics, the most progress has been made using trapped ions while other systems that have been explored include cavity QED, BEC's, and optical lattices. The greatest issue facing quantum computing schemes is scalability. Demonstrations of cNOT gates and even entire quantum algorithms have been demonstrated for small numbers of qubits, but a large scale system consisting of hundreds of qubits or more has proven a difficult challenge.

An optical lattice filled with atoms or molecules acting as qubits is one promising path to quantum computation. There are a variety of methods available that can theoretically produce a cNOT gate. For example, exciting an atom to a high n quantum number, called a Rydberg atom, blocks nearby atoms from excitations to Rydberg states due to an increased range in molecular potential shifting energy levels. Known as Rydberg blockade, atomic transitions become dependent on proximity to a Rydberg atom creating entanglement [71]. Chin *et al.* are investigating using a pair of lattices — one filled in each site with Li, and the second a sparsely filled Cs lattice. Controlling the phase of the lattice light with an EOM allows the lattice sites, and the atoms they contain, to be moved. The Cs lattice acts as read/write head while information is stored in the Li lattice. When Li and Cs are brought into close proximity, they interact in a laser field, “writing” the Li state onto Cs, which is translated and in turn writes the information on another Li atom, entangling the two Li atoms [72].

We focus on the proposed use of polar molecules as qubits. DeMille proposed a scheme involving placing polar molecules in an optical lattice within a linearly varying electric field, \vec{E}_{ext} [11]. Dipoles oriented along the \vec{E}_{ext} represent state $|0\rangle$ and those oriented oppositely are state $|1\rangle$. The electric field at a given lattice site a depends on the external field and the electric field due to the neighboring dipoles, assuming nearest neighbor interaction only:

$$\vec{E}_a = \vec{E}_{ext}(x_a) + \sum_{b=a\pm 1} \frac{-\vec{p}_b}{4\pi\epsilon_0|x_a - x_b|^3} \quad (1.9)$$

where p_b refers to dipoles adjacent to position a . Each dipole will have a position dependent dipole energy $W_a = -\vec{p}_a \cdot \vec{E}_a$, meaning dipoles can be addressed by oscillating fields of frequency $\nu_a = \nu_0 + |\vec{p}_{|0\rangle} - \vec{p}_{|1\rangle}| |\vec{E}_a|/h$, where $h\nu_0$ is the energy difference of the two states in zero field and $\vec{p}_{|0\rangle,|1\rangle}$ are the dipole moments of the two respective qubit states. The Rabi frequency of the transition at each site depends on the orientation of adjacent dipoles leading to entanglement. Longer temporal pulses are needed for cNOT operations to resolve the energy splitting due to dipole-dipole interactions and shorter pulses can be used for single qubit operations. That is we assume $|\vec{p}_{|0\rangle} - \vec{p}_{|1\rangle}| |\vec{E}_a| \ll h\nu_0$; the former energy defines the timescale for a cNOT operation based on the Rabi frequency and the latter defines the Rabi frequency for single qubit operations. It should be noted that while the nearest neighbor coupling cannot be turned off, the problem has been addressed already in NMR quantum computation with the “refocusing” technique and can be applied similarly here. This system has advantages of not having any mechanical motion or coupling to short-lived excited states. Error correction, another fundamental challenge of quantum computation, can be implemented extending this to a 2D or 3D lattice.

Many challenges will be encountered in achieving a quantum computer or simulator based on polar molecules. The first being the challenge of achieving a cold, dense sample capable of being held in an optical lattice. In a deep optical lattice, atoms and molecules exist in a Mott insulator phase which has unity filling of lattice sites. For polar molecules, which interact more strongly than atoms, this should correspond

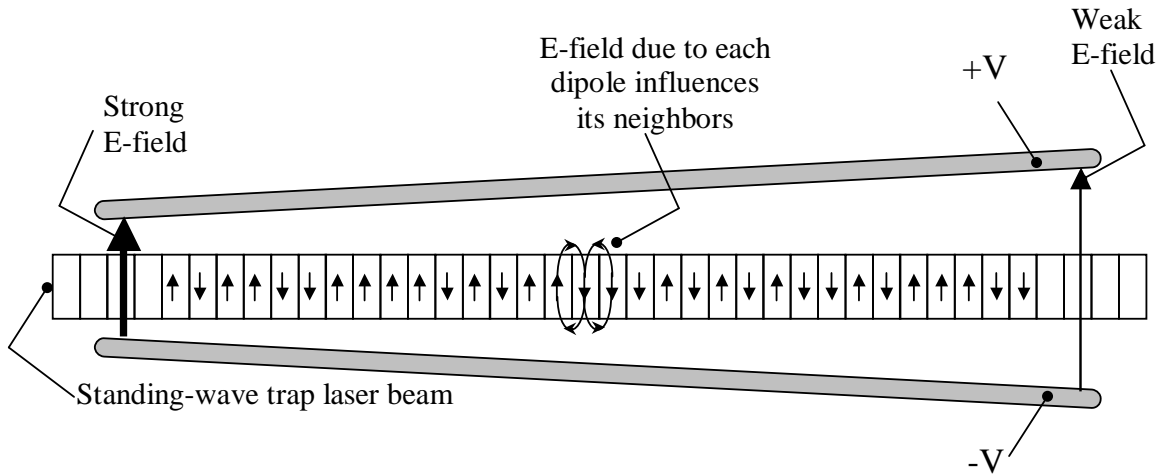


Figure 1.3. DeMille’s quantum computation scheme using polar molecules. Polar molecules are placed in a spatially varying electric field giving each site a different dipole dependent energy. Energy shifts due to dipole-dipole interactions with nearest neighbors allow for entanglement when an oscillating electric field drives a transition to a state where the dipole has the opposite alignment [11].

to a phase-space density of 10^{-3} — not quite BEC levels. Alternatively, theoretical studies suggest that two species can be placed in the same lattice with each lattice filled with one of each species, under the right conditions. This would allow molecule formation with unity probability at each site [14]. Another challenge is that in the lab frame, the molecule has no permanent dipole moment. Due to its rotational motion, it averages to zero. Creation of a superposition state either through an external electric field or through optical preparation will cause mixing between even and odd rotational states leading to a net average dipole moment. Mixing between the $J = 0$ and $J = 1$ state creates a dipole moment in the lab frame. In the rotational frame of the molecule, the dipole moment depends on the vibrational energy of the molecule, which will be greatest in its lowest $v = 0$ vibrational state of the ground electronic state. Thus, most experiments exploring polar molecules for quantum computation or simulation require the molecules to be prepared in the lowest internal singlet en-

ergy state, $|v = 0, J = 0\rangle$, which is non-trivial to access. The hyperfine structure of the molecule may also have to be considered, which can be considered a benefit as it provides more degrees of freedom to study, or a challenge when attempting to drive all molecules to the same state.

1.4 Choice of LiRb for Study

We now focus on our polar molecule of choice — LiRb. Most cold molecule research has been done on bialkali species. Because of their popularity, inexpensive diode lasers are available at the wavelengths of the D_1 and D_2 lines for each alkali metal species [73–80]. Production of cold molecules is not limited to bialkali elements, and any two atomic species that can be cooled and trapped in a MOT have the potential to produce cold molecules through PA or MA. Heteronuclear bialkalis have a permanent dipole moment, which makes them good candidates to study dipole interactions in cold and ultracold environments. Production of molecules through PA is most efficient for atoms with similar excitation energies. However, the dipole moment is greatest for atoms with the most different excitation energies, meaning a tradeoff between number of molecules created and dipole moment size. If interaction strength is the important parameter in a polar molecule study, as is likely the case for quantum computation, LiRb is a good candidate. With a dipole moment of 4.2 D in the ground state, only LiCs (5.5 D) and NaCs (4.6 D) have greater dipole moments among bialkali species [81]. There is also a certain amount of interest in filling in the missing parts of the bialkali molecule picture. There remain open questions from previous experimental results and LiRb will help give a better picture of the similarities and differences between various bialkali species. Also, we have recently found that LiRb has the highest observed PA rate among bialkali molecules [13].

Table 1.1 gives a partial summary of references for recent experiments being conducted on various heteronuclear bialkali molecules. KRb is perhaps the most studied and well understood molecule. In 2008, Ni et al. reported coherently driving KRb

molecules to the absolute ground state through stimulated Raman adiabatic passage (STIRAP) [21]. Ground state molecules have also been reported in LiCs from spontaneous decay following PA. Exploring the structure of LiRb will give insight in to general laws governing these types of molecules. For example, it is predicted that all LiX bialkali species along with KRb can undergo chemical reactions even in the absolute molecular ground state even at nK temperatures [37]. This can be tested in LiRb. The production of ground state LiCs molecules from spontaneous decay was rather surprising and is still not well understood [9]. Outside of bialkalis, there has also been work done in creating ultracold molecules from alkali-Yb mixtures [32].

Table 1.1
Research done on bialkali molecules.

Molecule	Reference
LiK	[25]
NaLi	[82]
LiRb	[13, 39, 40, 55, 83]
LiCs	[6, 7]
NaK	[84]
NaCs	[16]
KRb	[3, 21]
KCs	[85]
RbCs	[27]

2. Dual Species Magneto-optical Trap

Our first step towards producing ultracold polar molecules is to generate a collection of ultracold atoms using a magneto-optical trap (MOT). Laser cooling of molecules proves difficult due to the complicated energy structure of even the simplest dimers. Laser cooling techniques for atoms rely on atomic transitions that have a limited number of decay channels. Because such cycling transitions do not generally exist for molecules, the most common method for producing cold molecules is to start with a sample of cold atoms and induce a transition from an atomic scattering state to a bound molecule. This can be done either through photoassociation or magnetoassociation. Our work focuses on photoassociation. Magnetoassociation generally becomes more useful when the molecular structure is well known and transitions to a desired molecular state are easier to find.

Before discussing MOT theory, we mention some research into direct cooling of molecules via light. Ye *et al.* have proposed direct cooling of TiO in a molecular MOT similar to traditional atomic MOTs [29]. Optical Doppler cooling has been experimentally observed in SrF [28]. Another approach currently studied by Raizen *et al.* could be generally applied to any paramagnetic atomic or molecular sample. First, a supersonic atomic or molecular beam is slowed by pulsed magnetic fields, like a coilgun in reverse. Cooled sufficiently, the atoms can be further cooled and contained in a “one-way wall of light.” The scheme cools while the atoms or molecules scatter only a single photon on average, negating the need for a cycling transition on which traditional laser cooling is based [86]. These new cooling and trapping schemes, while promising, are largely untested or are still orders of magnitude away from producing atoms and molecules in densities comparable to those produced starting with dual species MOTs. In this chapter, we focus on the methods used to cool and trap ${}^7\text{Li}$ and ${}^{85}\text{Rb}$ simultaneously.

Many of the experimental techniques used to trap rubidium are covered in the thesis of Arthur Mills [87] and many other experiments. Here we summarize the operating principles of a MOT and make note of certain aspects that affect our specific experimental system. We note that our choices of atomic isotopes are purely based on natural abundances. For lithium, ${}^7\text{Li}$ is 92% abundant and ${}^6\text{Li}$ is 8%. For rubidium, the abundances are 72% for ${}^{85}\text{Rb}$ and 28% for ${}^{87}\text{Rb}$ [88]. We currently work with ${}^7\text{Li}$ and ${}^{85}\text{Rb}$ in order to trap as many atoms of each species as possible. The different masses of isotopes have a small effect on the energy levels of the atoms, so we could switch to trapping ${}^6\text{Li}$ or ${}^{87}\text{Rb}$ simply by adjusting the laser frequencies. This would result in greater losses from collisions with untrapped background atoms unless we were to use isotopically pure samples to achieve better MOT performance — most groups working with fermionic ${}^6\text{Li}$ use an isotopically enriched sample [89]. Alternatively, these background effects could be limited by having a primary and secondary MOT in different sections of the vacuum chamber, but this would require a much larger and more expensive chamber. Isotopic effects should slightly change molecular hyperfine levels, similar to atomic systems. Perhaps of greater interest, lithium has both a fermionic (${}^6\text{Li}$) and bosonic (${}^7\text{Li}$) species, meaning LiRb can be studied both as a boson and fermion.

2.1 Two-level Atoms in a Laser Field

While atoms are not two-level systems, we can use a two-level model to explain much of the physics behind laser cooling and trapping. In this model, all other energy levels except for a ground state and excited state with energy separation, $E = \hbar\omega_0$, are ignored. The atom is placed in a resonant laser field, $\vec{E} = \vec{E}_0 \cos(\omega t)$. Starting from the Schrödinger equation, it has been shown that the steady state population (normalized to 1) of the excited state will be

$$\rho_e = \frac{(\Omega/\Gamma)^2}{1 + 4(\Delta/\Gamma)^2 + 2(\Omega/\Gamma)^2} \quad (2.1)$$

where Δ is the the detuning of the laser $\omega - \omega_0$, Γ is the excited state decay rate,

$$\Gamma = \frac{(2\pi)^3 \mu^2}{3\pi \epsilon_0 \hbar \lambda^3}, \quad (2.2)$$

and Ω is the Rabi frequency, defined as

$$\Omega = \vec{\mu} \cdot \vec{E}_0 / \hbar, \quad (2.3)$$

where $\vec{\mu}$ is the dipole moment of the atomic transition. Often, equation (2.1) is written in terms of the saturation parameter or normalized laser intensity, s_0 ,

$$\rho_e = \frac{s_0/2}{1 + 4(\Delta/\Gamma)^2 + s_0}, \quad (2.4)$$

where $s_0 = 2(\Omega/\Gamma)^2 = I/I_{sat}$, where I is the intensity of the laser field ($I = \epsilon_0 c |\vec{E}|^2/2$) and the saturation intensity is given by

$$I_{sat} = \frac{\epsilon_0 c \hbar^2 \Gamma^2}{4\mu^2} = \frac{2\pi^2 \hbar c \Gamma}{3\lambda^3}. \quad (2.5)$$

The scattering rate for this atom due to spontaneous emission is proportional to the excited state population,

$$\gamma_p = \Gamma \rho_e = \frac{s_0 \Gamma / 2}{1 + 4(\Delta/\Gamma)^2 + s_0}. \quad (2.6)$$

We proceed using this two-level model as the basis for studying atoms in a magneto-optical trap, pointing out shortcomings in the model where appropriate.

2.2 Slowing Atoms Through Conservation of Momentum

We demonstrate how atoms traveling into a laser beam can be slowed. Each photon in an optical field carries momentum $p = \hbar k$, where $k = (2\pi)/\lambda$ is the magnitude of the wavevector \vec{k} . When an atom in a laser field is excited to a higher energy level, it absorbs a photon from the laser field. The momentum of the photon must be conserved and is transferred to the atom. As the atom decays back down to the ground state, it emits a photon. Momentum must once again be conserved so that a single excitation and decay will result in a net momentum change of

$$\Delta \vec{p} = \hbar \vec{k} - \hbar \vec{k}_{emitted} \quad (2.7)$$

where \vec{k} is the wavevector of the absorbed photon and $\vec{k}_{emitted}$ is the wavevector of the emitted photon. For the case of N such transitions, this becomes

$$\Delta\vec{p}_{net} = N\hbar\vec{k} - \hbar\sum_{i=0}^N\vec{k}_{emitted,i}. \quad (2.8)$$

Since spontaneous emission is a stochastic process, the emitted photons should be isotropic and random in direction. Thus,

$$\Delta\vec{p}_{net} = N\hbar\vec{k} - \hbar\sum_{i=0}^N\vec{k}_{emitted,i} = N\hbar\vec{k} - 0. \quad (2.9)$$

Excitations followed by stimulated emission result in zero net momentum change and can be ignored. Thus, the force exerted on the atom, which goes by a variety of names but we will call the spontaneous force, will be the photon momentum multiplied by the scattering rate due to spontaneous emission from equation (2.6):

$$\vec{F}_{sp} = \hbar\vec{k}\gamma_p = \hbar\vec{k}\Gamma/2\frac{s_0}{1 + 4(\Delta/\Gamma)^2 + s_0}. \quad (2.10)$$

There are two notable aspects of this force having to do with the saturation parameter, s_0 . First, as s_0 becomes very large, $\vec{F}_{sp} \rightarrow \hbar\vec{k}\Gamma/2$, giving an upper limit on the magnitude of the force. Secondly, while increasing intensity has diminishing returns when trapping on resonance ($\Delta = 0$), it does strengthen the force at larger detuning from resonance. This is known as power broadening (see figure 2.1). Power broadening essentially makes transition linewidths appear wider which can be troublesome for spectroscopy, but is an important aspect in cooling and trapping in a MOT.

Because the spontaneous force is a function of laser frequency, it becomes velocity dependent once the Doppler shift is considered. The one dimensional velocity distribution of a collection of atoms in a gas is given by the Maxwell-Boltzmann distribution,

$$f(v) = \sqrt{\frac{m}{2\pi k_B T}} e^{-mv^2/2k_B T}. \quad (2.11)$$

In the frame of the atom, the laser frequency is shifted due to the motion of the atom. The frequency shift is given by

$$\Delta_D = -\frac{v}{c}\omega \quad (2.12)$$

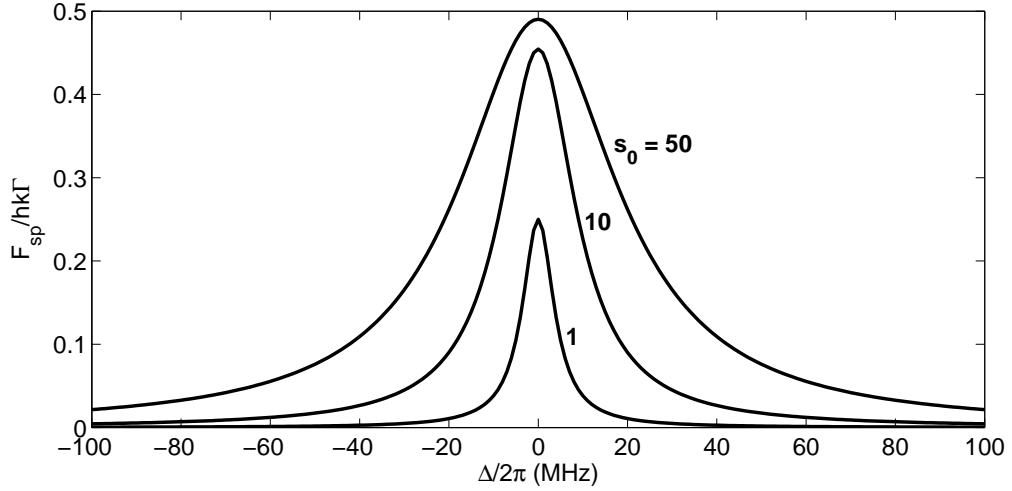


Figure 2.1. Spontaneous force vs. Detuning for $s_0 = 1, 10,$ and 50 . As laser intensity is increased the transition saturates, limiting the spontaneous force. However, the force is still increased for atoms away from resonance.

where $v = \vec{v} \cdot \hat{k}$, the atomic velocity in the direction of laser propagation, and $\omega = 2\pi\nu$ where ν is the frequency of the laser in the lab frame. Equation (2.11) can be reformulated in terms of a Doppler shift distribution, which would give the Doppler broadened linewidth of a transition.

$$f(\Delta_D) = \sqrt{\frac{m}{2\pi k_B T}} e^{-m(\Delta_D c)^2 / 2k_B T \omega^2}. \quad (2.13)$$

This distribution is plotted for both ${}^7\text{Li}$ and ${}^{85}\text{Rb}$ in figure 2.2. Thus the spontaneous force on moving atoms is actually truly a function of $\Delta_L + \Delta_D$, the sum of the laser detuning in the lab frame and the Doppler shift. Because of this, only a small fraction of atoms in a thermal sample interact with a resonant laser beam. However, this is actually the key to laser cooling and trapping. If $\vec{v} \cdot \hat{k} > 0$ then $\Delta_D < 0$, meaning these atoms will only interact with laser frequencies above, or blue detuned from resonance. In this case, since $\vec{v} \cdot \vec{F}_{sp} > 0$ and these atoms will be accelerated. If $\vec{v} \cdot \hat{k} < 0$, the opposite is true. These atoms will only interact with laser frequencies

below, or red detuned from resonance and will be slowed. Thus atoms traveling into a red detuned beam will be slowed.

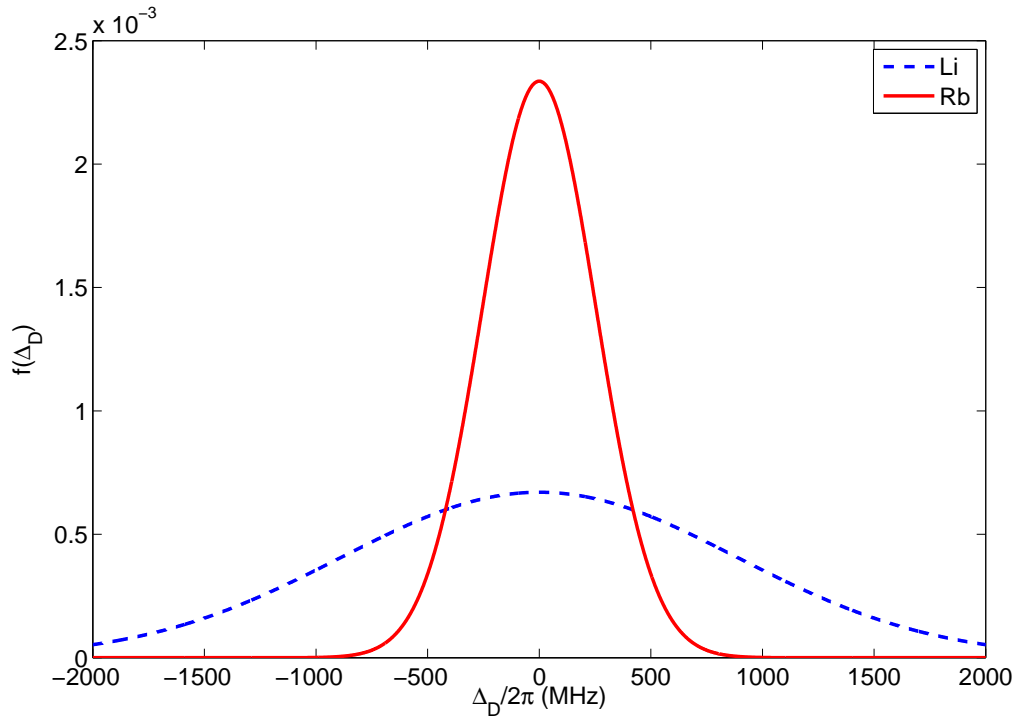


Figure 2.2. Population vs. Doppler shift based on the Maxwell-Boltzmann distribution at 300 K for Li and Rb. The spread in population is much larger for Li because of its smaller mass.

An effect of slowing the atoms down will be to reduce the magnitude of their Doppler shift, Δ_D , taking the atom out of resonance with the red detuned trapping light. In order to continuously cool and trap an atomic gas, the spontaneous force must be made to be spatially dependent as well. In order to introduce a spatial dependence, we must first go beyond a simple two-level system and introduce effects due to atomic interactions.

2.3 Effects of Atomic Structure on Cooling and Trapping

The extra complexity of true atomic quantum states inevitably does play an important role in how atoms are cooled and trapped. If this were not the case, laser cooling and trapping techniques would be universal for all atomic species provided an appropriate frequency laser is available. Laser cooling and trapping of alkali metals usually occurs on the D₂ line — the transition from the $n^2S_{1/2}$ state to the $n^2P_{3/2}$ state, where n is the ground state principal quantum number of the valence electron of the given species. (The D₁ line is the transition from $n^2S_{1/2}$ to $n^2P_{1/2}$.) The $n^2S_{1/2}$ and $n^2P_{3/2}$ states are split into 2 and 4 hyperfine sublevels respectively, which are denoted by their corresponding total atomic angular momentum quantum number, F . Each hyperfine level has $2F + 1$ magnetic sublevels, labeled m_F , which are degenerate if no external electric or magnetic field is present. A ground state hyperfine level F and an excited hyperfine level $F' = F + 1$ act as the two levels of our system, but the m_F sublevels and other hyperfine states must be considered. A MOT creates a spatially dependent spontaneous force by taking advantage of the shift of the m_F sublevels in the presence of a B-field.

2.3.1 One Dimensional MOT

Creating a spatially dependent restoring force in a MOT from the velocity dependent spontaneous force requires control over an external magnetic field and the polarization of light driving the atomic transition. A spatially dependent magnetic field is created by positioning two magnetic field coils such that the trapping region falls in the center of both coils, halfway between them. Operating the coils in the anti-Helmholtz configuration such that currents flow in the opposite direction through the coils, they create a linearly varying magnetic field in the trapping region. Magnetic fields break the degeneracy of the m_F magnetic sublevels in atoms via the Zeeman effect. The shift for a weak field is given by

$$\Delta E = \mu_B g_F B_{ext} m_F \quad (2.14)$$

where μ_B is the Bohr magneton, g_F is the hyperfine Landé g-factor, and B_{ext} is the magnitude of the external magnetic field defining the quantization axis [90]. The Landé g-factor is a function of the J , I , and F quantum numbers resulting from expectation values of angular momenta. Assuming $\vec{B} = (\partial_z B)z\hat{z}$, taking \hat{z} to be the quantization axis, (2.14) becomes

$$\Delta E(z) = \mu_B g_F (\partial_z B) m_F z. \quad (2.15)$$

Now the spontaneous force depends on overall detuning of $\Delta_L + \Delta_D + \Delta(z)$ where $\Delta(z) = (\Delta E_{F'}(z) - \Delta E_F(z))/\hbar$ from the Zeeman shift. $\Delta E_{F'}(z) - \Delta E_F(z)$ will be the difference in energy shifts between the excited and ground state.

Combining the spontaneous force, Doppler shift, and Zeeman shift, the complete picture of a MOT in one dimension is given. For illustrative purposes, we consider an atom with an $F = 0$ ground state and $F' = 1$ excited state, and thus with three m_F magnetic sublevels. The extension to atoms with different F quantum numbers is straightforward. Photons are spin 1 particles, with σ^+ polarization carrying $+\hbar$ angular momentum and σ^- polarization carrying $-\hbar$. Since angular momentum must also be conserved on absorption of a photon, σ^+ causes $m_F + 1$ transition and σ^- polarization causes $m_F - 1$ transitions. With counterpropagating σ^+ and σ^- beams in a quadrupole field, the dependence of $\Delta(z)$ on m_F means that in one direction, atoms moving towards the σ^+ beam will be held on resonance by the B-field where $\Delta(z)$ compensates for the changing Δ_D as the atom is slowed, while in the opposite direction atoms moving towards the σ^- beam will be held on resonance. This creates a continuous restoring force along the \hat{z} axis, which is often approximated linearly, $F_{sp,z} \approx -kz$. This 1D case is pictured in figure 2.3. Having three sets of counterpropagating beams for each dimension creates a 3D trap, with atoms trapped at the center.

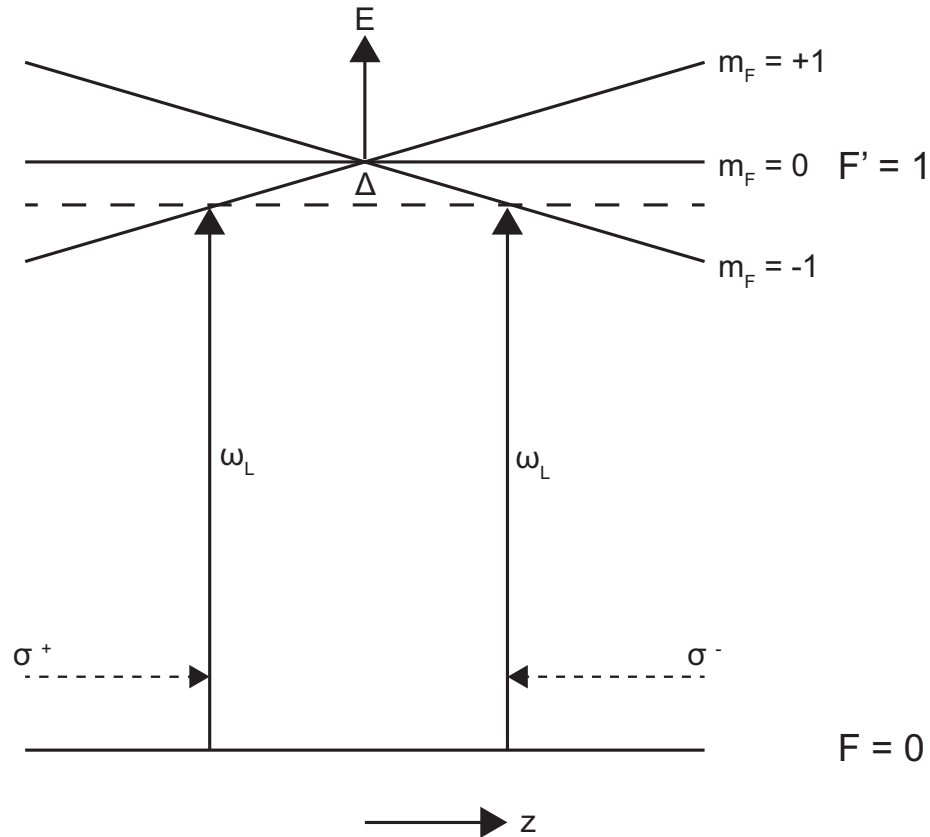


Figure 2.3. Model for 1D MOT. Magnetic sublevels are split by a spatially inhomogeneous magnetic field. σ^+ polarized light will only be resonant with $m_F = +1$ atoms to left of the origin. σ^- polarized light will only be resonant with $m_F = -1$ atoms to the right of the origin. In both cases the light pushes atoms to the center, creating a restoring force.

2.3.2 Effect of ${}^7\text{Li}$ and ${}^{85}\text{Rb}$ Hyperfine Structure on MOT Operation

So far, we have focused only on the general case of a two-level atom — a system which does not actually exist. The atomic structures of ${}^7\text{Li}$ and ${}^{85}\text{Rb}$ are given in figure 2.4. The atom can be treated as a two-level system by operating on a cycling transition. In ${}^{85}\text{Rb}$ this is the $F = 3$ to $F' = 4$ transition. Selection rules require the $F' = 4$ state excited atom to decay back down to the $F = 3$ state as $F = 0, \pm 1$ transitions are dipole allowed. However, there is a small but non-negligible probability which increases with laser intensity, that an atom is excited to the $F' = 3$ state (see

equation (2.1)), and end up in the $F = 2$ ground state. When this happens, that atom will become stuck there if no other laser field is present because of the large ground state hyperfine splitting. To account for this, a weaker repump laser is introduced on the $F = 2$ to $F' = 3$ transition to pump the atoms back into the cycling transition after they fall out. While the atom is no longer a true two-level system at this point, it is still a good approximation because the trapping light is of much greater intensity than the repump light.

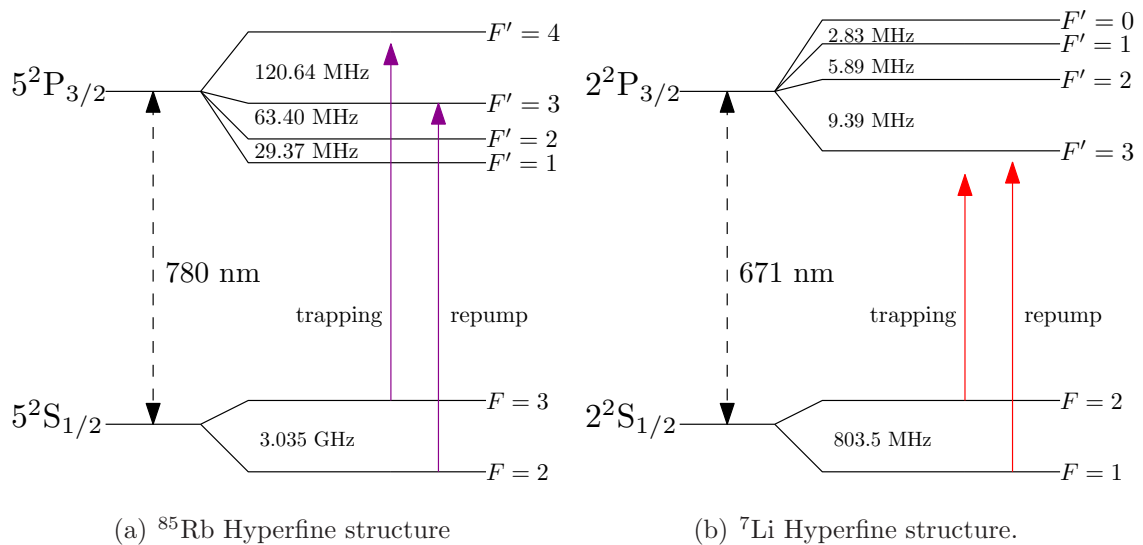


Figure 2.4. The energy levels of (a) ^{85}Rb [90] and (b) ^7Li [91]. Lasers driving the trapping and repump transitions in each species are also shown.

All of the alkali metals have a single valence electron and thus a similar atomic structure and can be trapped on a cycling transition with a repump beam. For most alkali metals, the power of the repump beam need not be large. However, for Li, the small spacing between the excited F' hyperfine states makes the two-level picture insufficient. The separation between hyperfine states is on the same order as the natural linewidth ($\Gamma/2\pi = 5.89$ MHz [89]). Because of this, trapping light resonant with the $F = 2$ transition will populate the $F' = 1, 2, 3$ excited states, meaning significant population will decay into the $F = 1$ hyperfine ground state. Unlike

rubidium, this occurs every few transitions, rather than after thousands. Because atoms will cycle into the lower hyperfine level much faster, a more intense repump laser field is needed. For lithium, the repump field is usually about half the intensity of the trapping laser field [92]. The role of the repump light is no longer simply to pump the atoms back to a cycling transition, because no such transition exists. It is, perhaps, more accurate to think of the two laser fields as co-trapping beams in lithium. Whereas the polarization and geometry of the repump light for rubidium is largely unimportant, the repump light for lithium must have the same polarization and 3D geometry as the trapping light.

Because the repump beam has an intensity on the order of the trapping beam, equation (2.1) is no longer valid as Li in a MOT no longer approximates a two-level system. A new ρ_e could be derived based on a three level system coupled by two laser fields for a closer approximation, and the development from that point forward will be identical. This is an important point as monitoring the fluorescence is the most straightforward way to determine the population of trapped atoms and the fluorescence depends on the decay rate which comes from ρ_e . Most groups use an ansatz that treats the trapping and repump as two separate two level systems and estimate the percentage of population in each, or by treating as a single two level system with both trapping and repump power on the trapping transition, since both are exciting to close to degenerate states. These methods should calculate populations to within a factor of 2.

2.4 Temperature Limits

Temperature and atom density are the two most important MOT characteristics. It is important to know how the MOT temperature compares to theoretical benchmarks. The transition linewidth and Doppler shift define the coldest temperatures possible for a true two-level system cooled via the spontaneous force in a MOT. If the transition has a natural linewidth of Γ , atoms will absorb light Doppler shifted

within this linewidth. If this is the case, the average energy of atoms will be $\Gamma/2$, giving a temperature of

$$k_B T_D = \frac{\hbar\Gamma}{2}, \quad (2.16)$$

known as the Doppler limit.

Since atoms are not two-level systems, they can be cooled beyond this limit through scattering of light by spontaneous emission through a process known as polarization gradient cooling. Any cooling that relies on spontaneous emission has a lower temperature limit associated with the recoil momentum of scattering a photon. The atom must have momentum of at least $\hbar k$ and thus energy of $\hbar^2 k^2/2m$. Thus the recoil limit is given by

$$k_B T_r = \frac{\hbar^2 k^2}{2m}. \quad (2.17)$$

Table 2.1
Temperature limits for ${}^7\text{Li}$ and ${}^{85}\text{Rb}$.

	Doppler Limit	Recoil Limit
${}^7\text{Li}$	22.5 μK	3.02 μK
${}^{85}\text{Rb}$	23.3 μK	0.18 μK

Table 2.1 gives these characteristic temperatures for both ${}^7\text{Li}$ and ${}^{85}\text{Rb}$. Lower temperatures can be achieved by methods that do not involve spontaneous emission, such as evaporative cooling. Our MOT temperature is one or two orders of magnitude above these limits, but still in what is considered the ultracold regime. For ${}^{85}\text{Rb}$ the estimated temperature is $\approx 200 \mu\text{K}$, while an upper limit of 1.1 mK for ${}^7\text{Li}$ has been established through photoassociation measurements [13, 55]. The usual method of measuring temperature is by checking fluorescence or cloud expansion after releasing atoms from the MOT [92]. The capability of doing the measurement exists in our system, but we have not relied on this method to measure temperature.

2.5 Capture Velocity and Loading Rates

For each photon that an atom absorbs, the velocity of the atom will change by the recoil velocity $v_{rc} = \hbar k/m$. The magnetic field gradient is designed to compensate for the changing Doppler shift as the atom is slowed. The atomic velocity, and thus Doppler shift, can be made into a function of position (similar to the Zeeman shift) if one assumes a velocity of zero at the edge of the trapping region - which should approximately be the case for trapped atoms. In that case, applying basic kinematics, we have

$$v(z) = \sqrt{2v_{rc}\gamma_p(z - d/2)}, \quad (2.18)$$

for a trap with beams diameter d . Closely associated with this is the capture velocity. Assuming the atoms will interact with a MOT beams from $-d/2$ to $d/2$, the maximum velocity at which an atom can be captured is

$$v_c = \sqrt{2v_{rc}\gamma_p d}. \quad (2.19)$$

All atoms travelling faster than this will pass through the MOT without scattering enough photons to be trapped.

The number of atoms trapped for either species can be modeled with a simple rate equation,

$$\frac{dN}{dt} = R - \frac{N}{\tau}, \quad (2.20)$$

where N is the number of atoms, τ is the trap lifetime and R is the loading rate. We examine τ in more detail later, but R can be computed by using the Maxwell-Boltzmann distribution to compute the flux of atoms crossing the trapping surface with a velocity less than v_c . This yields a trapping rate of

$$R \approx \frac{nd^2v_c^4}{u^3} \quad (2.21)$$

where n is the density of atoms, d is the beam diameter which define the trapping surface, and $u = \sqrt{2k_B T/m}$ [93]. The loading rate has a d^4 dependence, as v_c^4 also contributes d^2 term. Thus, the trapping beam diameter strongly influences the

number of trapped atoms. In general, it is advantageous to have large MOT trapping beams to trap many atoms and for ease of alignment. However, it must be noted that expanding beams reduces $s_0 = I/I_{sat}$ and the scattering rate, γ_p . If the beam intensity is close to the saturation intensity, the decrease in the trapping force may cancel the effect of increased beam size.

In our system, measuring the trap lifetime, τ , for Li is quite easy. As discussed in the next section, Li is loading by a slowed atomic beam. Turning off the beam shutter cuts off the flux of Li into the trapping region causing R to be zero, at which point the exponential decay of MOT fluorescence can be observed. This is covered in more detail in Sourav Dutta's thesis [83]. The observed trap lifetime for Li was the basis for studying collisions between Li and Rb as the presence of a second species introduces losses due to interspecies collisions [94].

2.6 Zeeman Slower

Certain properties of Li present some extra obstacles to cooling and trapping. First, being one of the lightest elements, the Boltzmann velocity distribution of Li has a much larger spread than heavier elements. (See figure 2.2.) Because of this, a much smaller fraction of thermal Li will be within the capture velocity given by equation (2.5). This effect is exacerbated by the fact that Li must be heated to around 400°C to have a high enough background vapor pressure. As Li starts to thermalize and approach room temperature (where more of the thermal population is within the capture velocity), it increases the probability that it will simply adsorb to the surfaces of the vacuum chamber, meaning it can no longer be trapped. Where Rb can be trapped simply by using dispensers that introduce a background flux Rb vapor through the trapping region, special methods are usually employed to introduce Li to the trapping region to ensure a large flux of trappable atoms.

The usual method is to use a Zeeman slower, which consists of a thermal atomic beam that is slowed by the spontaneous force from a resonant laser while traveling

through a spatially varying magnetic field. It relies on the same principles that allow a MOT to cool and trap atoms. The atoms are already transversely cool because of the collimating methods used to create the beam. A single red detuned laser beam is used to cool them longitudinally, slowing them as they travel opposite the direction of beam propagation. In a MOT, the spatially varying B-field that keeps the atoms resonant with the laser is generated by anti-Helmholtz coils. In a Zeeman slower, the varying field is simply created by tapering the number of turns in a magnet coil along the path of the atomic beam so that the magnitude of the B-field decreases. The design of the tapered coils is important as the Zeeman shift needs to decrease at the same rate as the Doppler shift decreases. The velocity and thus frequency shift of the atom can be calculated from equation (2.18). The goal of a Zeeman slower is not to achieve zero velocity atoms, which would stop them from reaching the MOT entirely, but to have nearly all the atoms in the atom beam have a slow enough velocity that they will all be captured once entering the MOT. The use of Zeeman slowers is not simply limited to Li, but it is also used as a way to trap heavier atoms while using large detunings at lower intensities for colder MOTs and to reduce untrapped background gas. Zeeman slowers are thus useful for experiments that require quantum degeneracy.

Experimentally, Zeeman slowers can be quite long (Ours is ≈ 30 cm.) and the B-fields they create can often stray into the MOT region causing the trap to be distorted. Because of this, field canceling coils are often required. The length also causes atoms with too high a transverse velocity to be lost before getting to the MOT region meaning that many Zeeman slowers are accompanied by a 2D MOT used for extra transverse cooling beyond the collimation achieved by the aperture(s) that create the beam. Our Zeeman slower was designed by Sourav Dutta and does not incorporate a 2D transverse cooling stage. The atom numbers we measure would not be possible without the Zeeman slower, but we have found that small Li MOTs can be generated just by a slowing beam without the slower's magnet coils turned on.

2.7 Dark SPOT

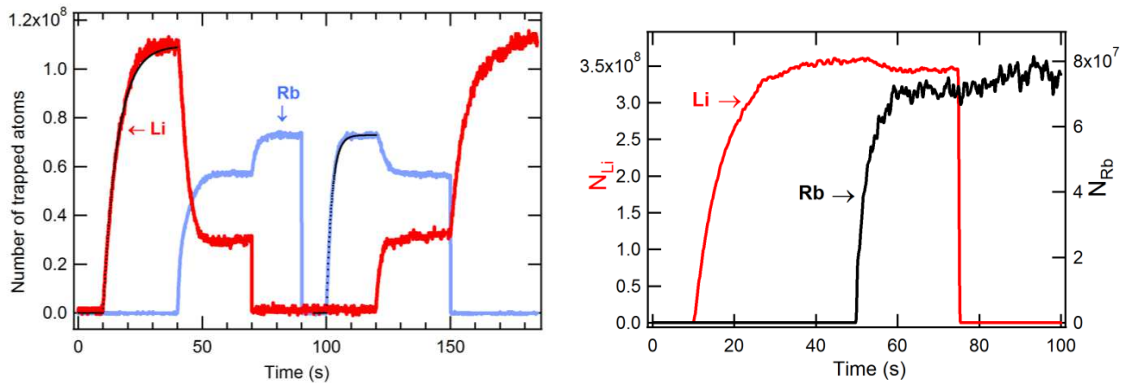
To increase the number of trapped atoms in a MOT, one can increase the beam diameter, increase the laser intensity, use a Zeeman slower, etc., but in large part, these changes increase the volume of the MOT without increasing the density. This is because as trapped atoms fluoresce, the photons emitted can be absorbed by another trapped atom and the momentum absorbed will push the second atom away from the first. Thus, the spontaneous emission from trapped atoms in a MOT creates a repulsive force between atoms. When the spontaneous force from trapping lasers balance the repulsive force from spontaneous emission, the trap operates in an equilibrium regime where the density is limited by the outward radiation pressure, meaning additional trapped atoms will increase the volume but not the density of atoms in the trap [49].

In trying to create a BEC, Ketterle developed a dark spontaneous force optical trap (dark SPOT or dark MOT) – essentially a MOT with a hole in the middle of the repump beam, so that at the center of the MOT, atoms will not be repumped onto the cycling transition, but will remain in the dark state until they start to move outside the trapping region. Another method was to induce a dark state temporally by cycling the repump beam on and off. Both have the effect of suppressing fluorescence in the center of the trap, which removes the outward force due to radiation pressure and increased atom density by up to an order of magnitude [45].

Dark MOTs require that the repump can be separated from the trapping light so that a hole can be placed in the repump beam. They also require that the repump be present in at least two dimensions of trapping so that a repump “shell” can be formed around the dark region of the MOT. Because of this, one cannot employ a dark MOT in Li because of the requirement that the repump have the same polarization and be propagating with the trapping frequency in all dimensions to act more as a co-trapping beam. Dark MOTs can be employed for all other alkali metals. However, as the excited hyperfine splitting increases, the atoms stay on the cycling transition and

keep fluorescing longer before ending up in the dark state, mitigating the intended effect of the dark region. To drive atoms into the dark state faster and improve dark MOT densities by minimizing fluorescence, a depump beam being is sometimes used to actively drive the atom into the dark state. In ^{85}Rb , the depump would be resonant with the $F = 3 \rightarrow F' = 2$ transition.

Because molecular production via photoassociation is proportional to $\rho_{\text{Li}}\rho_{\text{Rb}}$, it is advantageous to have the MOTs be as dense as possible. A dark MOT is essential for LiRb, because collisions between Li and excited Rb^* are the main loss mechanism when both species are present. To maintain high atom numbers in both MOTs, a dark MOT is required for Rb. Figure 2.5 shows how the MOT atom numbers are mutually affected in a dark MOT versus a bright MOT from a previous study on interspecies collisions done by Sourav Dutta.



(a) Normal MOT operation

(b) Dark MOT operation

Figure 2.5. Comparison of dark MOT vs. normal MOT operation from a collisional study conducted by Sourav Dutta. Adapted from his thesis [83].

3. Experimental Setup

The experimental apparatus for our cold molecule experiments can roughly be divided into two main systems — the laser system and the vacuum system. The laser system can be subdivided into the atomic cooling and trapping lasers, the PA laser, and the ionization laser. The components of the vacuum system consists of a lithium oven, atomic beam/Zeeman slower, an atom trapping region, and a time-of-flight mass spectrometer. In this chapter we discuss the functional details of these systems and some of the electronics and software that control them.

3.1 Cooling and Trapping Lasers

In our system, all of the lasers that cool and trap atomic rubidium and lithium are external cavity diode lasers (ECDLs). We use a mixture of commercial and home built diode lasers for this purpose. Free running diode lasers are too broadband for atomic physics, are difficult to tune, and tend to be multimode without feedback. Using some kind of optical feedback in an external cavity can narrow the linewidth of a diode laser and by mounting the feedback element on a piezoelectric transducer (PZT) the external cavity length, and thus the wavelength, can be electronically controlled. One could use mirrors, microscope slides, gratings, etalons, etc. [73–80]. Most ECDL lasers today use gratings in their external cavity to reduce linewidth to less than 1 MHz. The usual cavity configurations for gratings are Littrow or Littman-Metcalf. The details of these geometries can be found in the thesis of Arthur Mills [87], but the details of variants are widely available. The design used in our home built lasers was developed by Sourav Dutta [75]. The compact design makes the cavity very easy to stabilize using inexpensive thermoelectric coolers (TECs) and when the grating is

positioned properly, they can be tuned over 100 GHz when the piezo and current are scanned together.

As discussed in the previous chapter, trapping each atomic species requires two frequencies — one for the main cycling transition and a second for the repump. Being a dual species MOT, we must generate both frequencies for ${}^7\text{Li}$ and ${}^{85}\text{Rb}$. Because we also employ a Zeeman slower to trap lithium, appropriate laser frequencies must be generated for it also. In total, six stable laser frequencies are required. Figure 3.1 gives the overview of the atomic cooling and trapping laser setup for our dual species MOT.

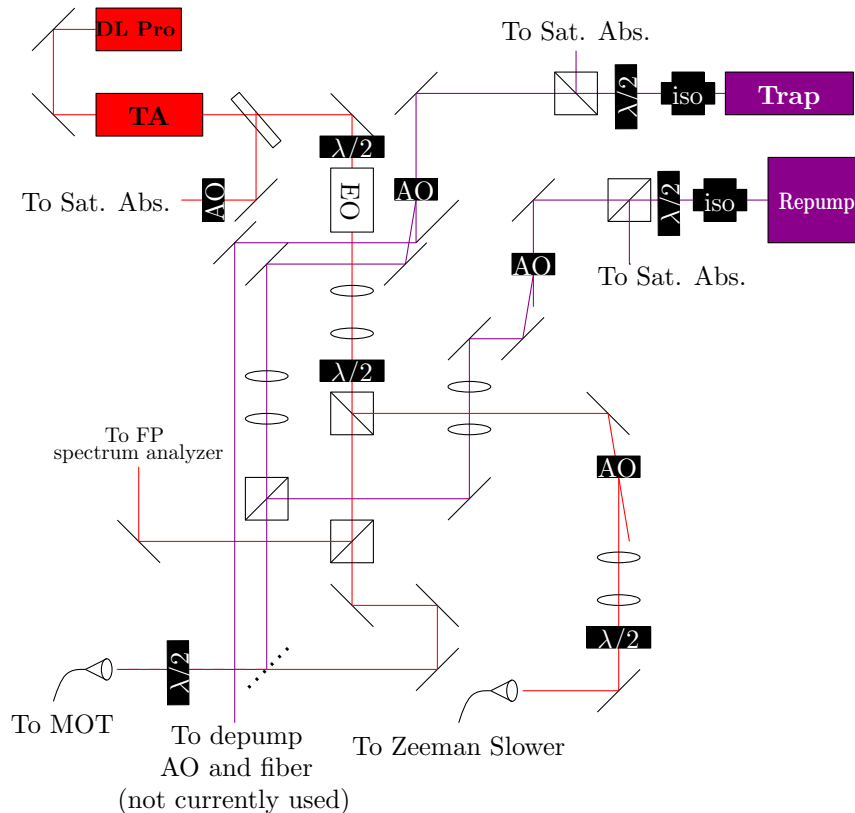


Figure 3.1. Diagram of the atomic cool and trapping laser system. Stabilized lasers, EOMs, and AOMs, generate frequencies for the Rb MOT, Li MOT, and Li Zeeman slower. Lenses are required to mode match beams to PM fiber input. Waveplates and PBSs are required for clean polarization into PM fiber.

For rubidium, we generate trapping and repump frequencies using two separate lasers. The trapping laser is a 1 W, 780 nm, Littrow ECDL Tiger laser from Sacher Lasertechnik. This laser requires strong optical isolation, as even small amounts of unwanted optical feedback can make the laser unstable. The repump laser is a home built laser with about 50 mW of output power at 780 nm. The trapping and repump beams have orthogonal polarization so that they may be combined on a polarizing beam splitter (PBS).

Because the ground state hyperfine splitting for ${}^7\text{Li}$ is so small, we generate trapping and repump beams for both the MOT and Zeeman slower using acousto-optic modulators (AOMs) and electro-optic modulators (EOMs) to frequency shift a single source with easily obtainable RF electronics. AOMs generate a standing RF acoustic wave in a crystal through which the laser passes. The beam coming out of the AOM will be diffracted when driven at an RF frequency. The processes can be viewed as a photon scattering off a phonon, shifting its momentum and energy. An EOM relies on a crystal that has an electric field dependent index of refraction. When a DC field is applied, an EOM acts like a field dependent waveplate, retarding the phase of light polarized in the same orientation as the field by an amount dependent on the strength of the field. When an RF signal is applied, the phase is modulated at the RF frequency, which adds sidebands to the main carrier frequency at integer multiples of the driving frequency. The amount of power in each sideband depends on the RF power applied and can be calculated by expanding the modulated optical field in terms of Bessel functions,

$$Ae^{i\omega t + i\beta \sin(\Omega t)} = Ae^{i\omega t} \left(J_0(\beta) + \sum_{k=1}^{\infty} J_k(\beta) e^{ik\Omega t} + \sum_{k=1}^{\infty} (-1)^k J_k(\beta) e^{-ik\Omega t} \right), \quad (3.1)$$

where β is the modulation depth and Ω is the modulation frequency [95]. The amplitude can be modulated by placing a polarizer after the EOM and rotating the input polarization so that it is a 45° angle to the RF electric field, causing the polarization to change at the RF frequency.

In our experiment, generating the frequencies needed to trap ${}^7\text{Li}$ starts with a commercial 35 mW 670 nm DL Pro ECDL in Littrow configuration from Toptica Photonics. Only 28 mW are usable after an internal optical isolator and in general only 18–20 mW are obtained because alignment of the feedback grating in the DL Pro is quite difficult given the design of the laser. The DL Pro is amplified by a 500 mW BoosTA tapered amplifier (TA) from Toptica Photonics. An optical isolator in the BoosTA reduces the output by about 20%, and in general 360–380 mW was the maximum power output measured. The DL Pro output is highly elliptical and we periscope the beam so that the polarization and ellipticity is rotated 90° to match the desired input of the TA. Improper matching of the input beam’s shape and divergence can cause a reduction of up to 100 mW. In previous configurations, a lens system was used and the output power strongly depended on the placement of the collimating lens. The DL Pro/BoosTA combination is more difficult to set up than a single high power ECDL like the Tiger laser, but single mode laser diodes (LD) at 670 nm are uncommon and are unavailable at high powers. At low powers they can be purchased from companies like Toptica, but are usually quite expensive when compared to 780 nm diodes available for under \$100. (Toptica only sells AR coated diodes at 670 nm.) Inexpensive low power 10 mW LDs at 670 nm are available from Roithner Lasertechnik.

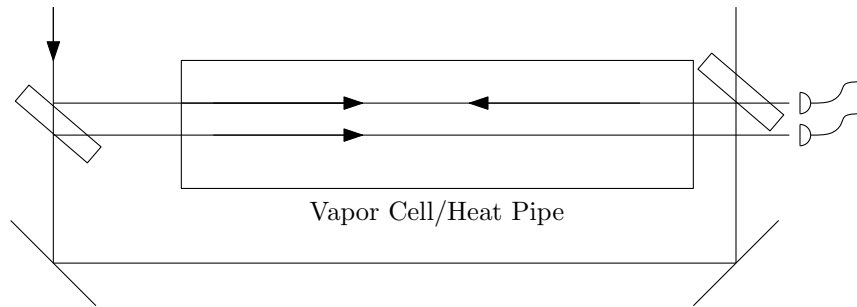
Because we use a Zeeman slower to load the Li MOT, only 80 mW of light is needed (50 mW for the MOT beams and 30 mW for the Zeeman slower), so the TA is normally run well below the maximum operating current in the hopes of extending its lifetime. The output of the TA goes through an EOM to produce sidebands, with the first upper sideband acting as the Li repump. Roughly 1/3 of the power is picked off and sent through an AOM which shifts the light down in frequency by 80 MHz for the Zeeman slower. The 670 nm Li and 780 nm Rb MOT beams are combined on a dichroic mirror and coupled into a polarization maintaining (PM) fiber that carries the light to the MOT region. The fiber allows the lasers to be located on a different table from the dual species MOT apparatus and spatially filters the beams

so that the MOT beams have clean Gaussian profiles. The Zeeman slower beam is carried via a separate PM fiber. PM fibers are required because MOT and Zeeman slower performance depend on having a stable, well defined polarization. Using non-PM fiber and cleaning up the polarization afterwards is not an option, because the fiber “scrambles” the polarization and any small perturbation changes the output polarization. This would cause light passing through any polarizing optic to fluctuate in power. Stable powers in each of the beams is required for high quality MOT operation.

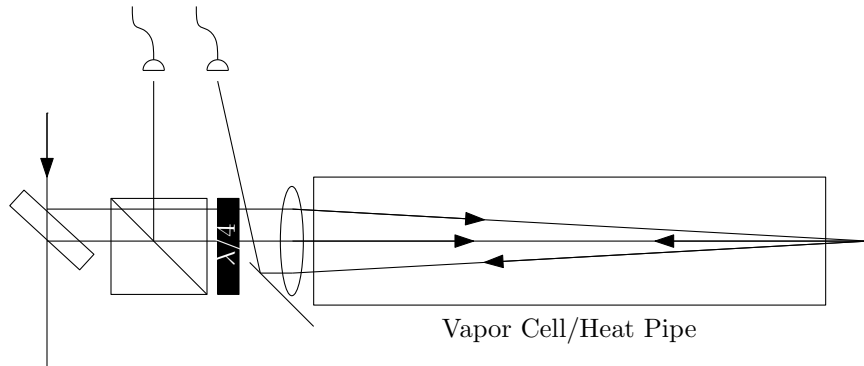
3.1.1 Frequency Stabilized Diode Lasers

We frequency stabilize all of the diode lasers in a similar fashion. We modulate the injection current for each laser at several kHz, which frequency modulates the laser output. A portion of the beam is sent through a saturated absorption setup and the resulting spectra are demodulated using lock-in amplifier circuits. Details of such schemes can be found in Arthur Mills’ thesis [87]. The balanced photodetector and modulation/lock-in amplifier circuits used were developed by Dionysios Antypas [96]. Because a MOT requires that the trapping beams be red detuned, the laser cannot simply be locked to the trapping transition. Instead, the laser is locked to a different transition and shifted to the appropriate frequency using an AOM. Two saturated absorption configurations used are shown in figure 3.2.

Saturated absorption involves a pump and probe beam counterpropagating in a vapor cell (or heat pipe if a sample needs to be heated to achieve high enough optical density). Without the pump, the measured probe transmission is reduced as it goes through a Doppler broadened resonance. To see the natural linewidth, the pump changes the transmission of the probe when atoms are interacting with both beams at the same time. Because the Doppler shift will be different for the pump and probe, most of the atoms within a distribution of velocities only interact with one laser at a time. Atoms with zero velocity along the axis of counterpropagation will have the



(a) Saturated absorption with windows.



(b) Saturated absorption a PBS.

Figure 3.2. Two saturated absorption schemes. In (a) the retroreflected pump and probe beams are produced by a semi-reflective window. In (b) the pump and probe is the same retroreflected beam, but the polarization is rotated so it can be separated by a PBS. Note that scheme (b) only requires a second beam if balanced photodiodes are used to subtract out the Doppler broadened background.

pump and probe driving the same transition. In this case, the pump is depleting the population the probe interacts with, resulting in a “hole” of increased transmission. This allows the natural linewidth of hyperfine transitions to be seen without the effects of Doppler broadening. The transmission of the probe is also affected by the presence of the pump when their frequency is halfway between two resonances within the same Doppler velocity envelope. In this case, the Doppler shift is of the same magnitude but opposite direction for the two beams, so the pump and probe excite two different transitions at the same time. This is called a crossover resonance and the

lineshape depends on whether the pump depletes the ground state population seen by the probe (increased transmission) or transfers population into a state resonant with the probe (decreased transmission). A second probe may be used to subtract out the Doppler broadened background by using balanced photodiodes, leaving only the saturated absorption lines. Figure 3.3 shows an example of the saturated absorption lines against the Doppler broadened velocity distribution from equation 2.13. In practice it is difficult to subtract out the Doppler broadened background completely, but it is generally unnecessary to have perfect subtraction.

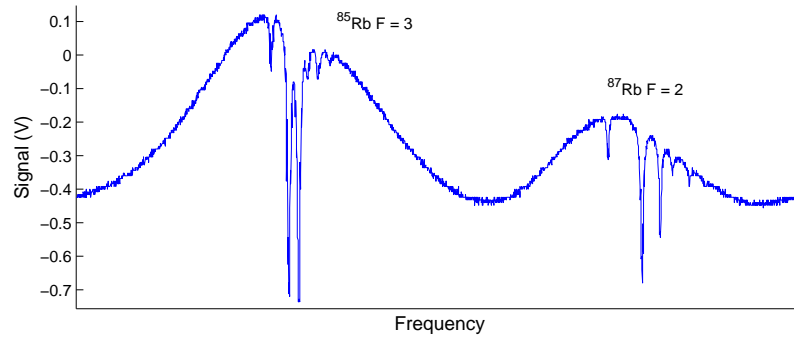


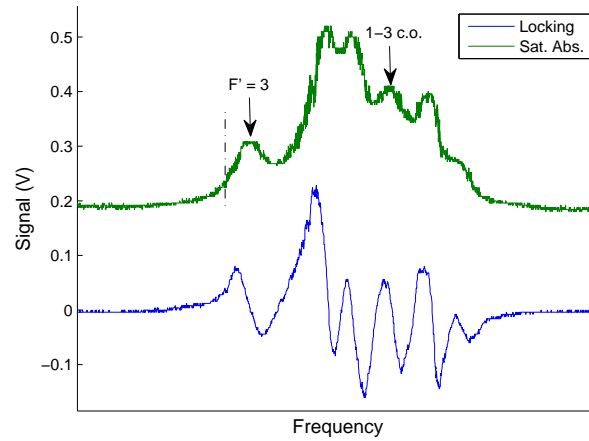
Figure 3.3. The saturated absorption spectra for ^{85}Rb ($F = 3$) and ^{87}Rb ($F = 2$). The hyperfine levels and crossover resonances are visible against the Doppler broadened background.

For ^{85}Rb , the $5\text{P}_{3/2}$ state hyperfine splittings are on the order of 100 MHz and the $5\text{S}_{1/2}$ hyperfine splitting is about 3 GHz. The Doppler broadened linewidth of a ^{85}Rb transition is about 500 MHz (at room temperature) and the natural linewidth is about 6 MHz. Thus saturated absorption shows the hyperfine structure of the $5\text{P}_{3/2}$ state. The ground state can be resolved without saturated absorption because the hyperfine splitting is greater than the Doppler broadened linewidth. This also implies that there are no ground state crossover resonances because there are almost no atoms travelling fast enough to experience a 1.5 GHz Doppler shift. For ^7Li , the $2\text{P}_{3/2}$ state hyperfine splittings are < 10 MHz and the $5\text{S}_{1/2}$ hyperfine splitting is 803.5 MHz. Lithium requires heating to nearly 400°C for the vapor pressure to be

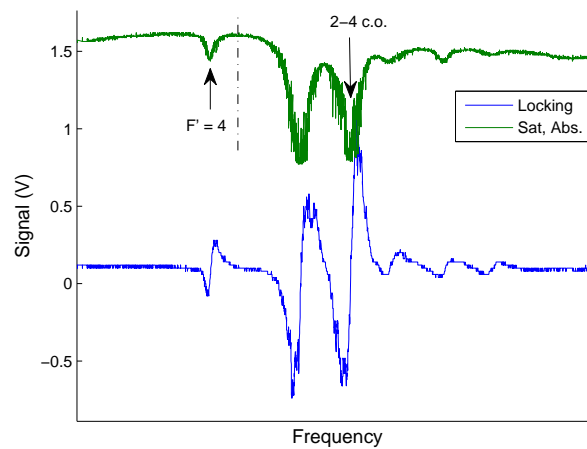
high enough to do spectroscopy. At this temperature the Doppler broadened linewidth of a transition is 2–3 GHz. Thus excited states in Li appear as a single line because the natural linewidth is on the order of the hyperfine splitting and there is a ground state crossover resonance because the ground state splitting is unresolved in a Doppler broadened measurement. This crossover resonance manifests as a decrease in probe transmission because the pump is driving atoms from the non-probe resonant ground state into the probe resonant ground state. Figures 3.4 and 3.6 show the saturated absorption spectra for Rb and Li.

We lock the trapping laser to the ^{85}Rb $F = 3 \rightarrow F' = 2, 3$ crossover resonance. An 80 MHz AOM shifts the frequency up so that it is between -3Γ and -4Γ detuned from the $F = 3 \rightarrow F = 4$ transition, where Γ is the natural linewidth of the transition (equation 2.2). The detuning of the Rb repump laser, in general, has negligible effect on the Rb MOT, so it could in theory simply be locked to the $F = 2 \rightarrow F' = 3$ transition. However, to accommodate any future experiments where the repump beam would require switching or tuning we use an AOM to control its frequency. For a bright MOT, we lock the repump to the $F = 2 \rightarrow F' = 1, 2$ crossover resonance and the AOM shifts frequency to be on resonance with the $F = 2 \rightarrow F' = 3$ transition. Figure 3.4 shows the saturated absorption signals and the locking signals generated from them that we use to stabilize the lasers.

For a dark MOT, it is possible to take the undiffracted portion of the trapping beam after the first AOM and use another AOM to shift it down in frequency from the $F = 3 \rightarrow F' = 2, 3$ crossover resonance down to be resonant with the $F = 3 \rightarrow F' = 2$ transition to create a depump beam. However, MOT fluorescence was sufficiently limited simply by making the repump less effective. For a dark MOT we lock the repump to the $F = 2 \rightarrow F' = 1, 3$ crossover instead of the $F = 2 \rightarrow F' = 1, 2$ crossover, thus causing the repump beam to be blue detuned by about 15 MHz from the $F = 2 \rightarrow F' = 3$, and limit the trapping laser power to 100 mW. This was easier to implement and gave roughly the same PA rates as a true dark MOT with a depump beam.



(a) Repump locking signal.



(b) Trap locking signal.

Figure 3.4. Locking signals for ^{85}Rb MOT repump and trapping lasers. The peaks to which the lasers are locked are the 1-3 and 2-4 crossover resonances respectively for dark MOT operation. When a bright MOT is desired, the repump is locked to the 1-2 crossover resonance (immediately to the right of the 1-3 resonance pictured). The approximate frequency of the AOM shifted laser that actually goes to the MOT region is noted with a dashed line and the transition on which the laser acts is marked. (For a bright MOT, the repump is resonant with the $F' = 3$ transition marked.)

Because the saturated absorption is done in a vapor cell with natural abundances, ^{87}Rb lines are also observed. The ^{85}Rb $F = 2, 3$ lines are at 780.238 and 780.244 nm respectively, while the ^{87}Rb $F = 1, 2$ lines are at 780.246 and 780.233 nm. Being familiar with each of set of hyperfine resonances is useful as it reduces the need to use a wavelength meter to find resonances if a laser is stable and tunable. The ^{87}Rb $F = 2$ resonance is seen in figure 3.3 and is distinguished by the large hyperfine splitting. The ^{87}Rb $F = 1$ resonance is shown in figure 3.5 for reference. Also, because the Rb dispenser in the vacuum system is also natural abundance, we could switch to a ^{87}Rb MOT should the interest arise.

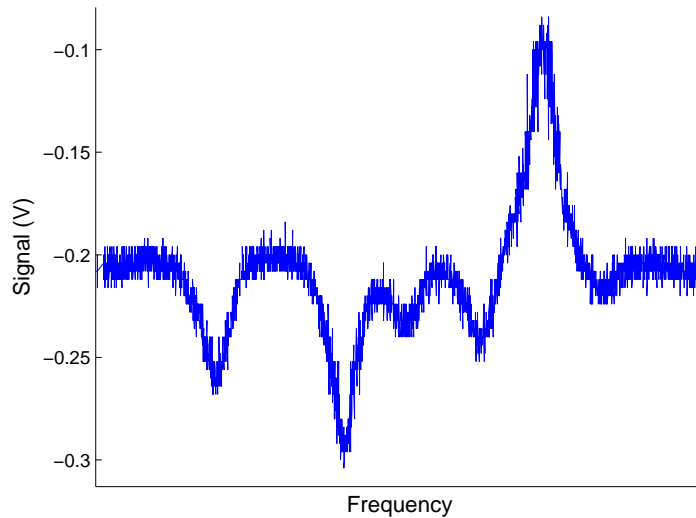
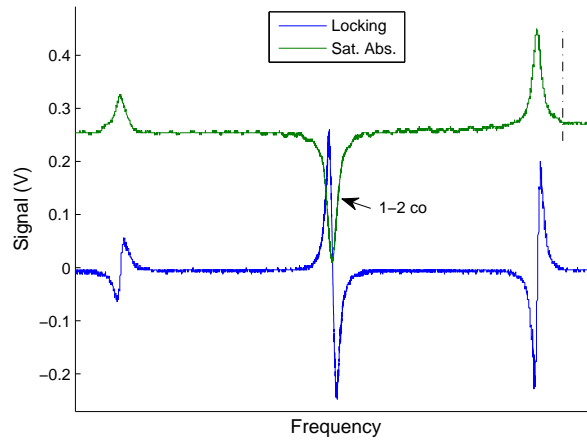
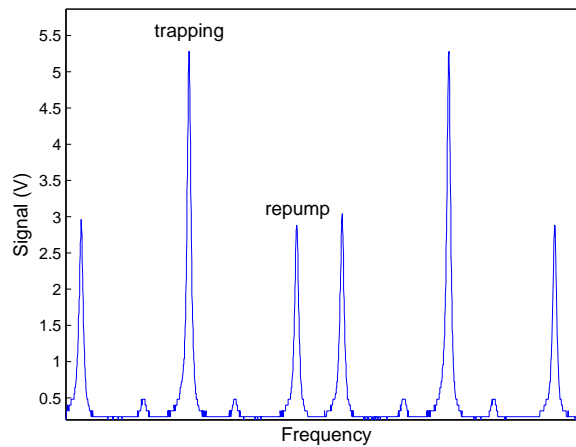


Figure 3.5. ^{87}Rb $F = 1$ transitions. Frequency decreases along the x-axis making the leftmost peak the $F = 1 \rightarrow F' = 2$ transition.

Locking the DL Pro to an appropriate frequency for cooling and trapping Li has extra considerations. First, while at room temperature, Rb has a high enough vapor pressure to generate a signal, but Li must be heated to around 400°C in a heat pipe for saturated absorption. Next, we have to rely on the ground state hyperfine structure to lock the laser as the excited states are roughly degenerate in a saturated absorption scan. The ground state hyperfine splitting is 803.5 MHz, and AOMs above

200 MHz are quite expensive. Frequency shifting light to the crossover resonance halfway between $F = 1$ and $F = 2$ transitions in ${}^7\text{Li}$ is possible by double passing light through a 200 MHz AOM. For power considerations, we do not shift the output of the TA, but rather frequency shift the beams used for saturated absorption beam up in frequency. This fixes the output of the TA to the red of the $F = 2$ line when the saturated absorption beam is locked to the crossover resonance. The orientation of the ground state crossover is reversed because instead of the pump depleting the population seen by the probe, the pump is cycling population back into the hyperfine state with which the probe interacts. (See figure 3.6.) The frequency of the AOM is set so the trapping beam will be -4Γ to -5Γ detuned from the $F = 2$ resonance in ${}^7\text{Li}$. The repump frequency is generated by an EOM, which we will discuss in more detail later. (Several experimental setups were tried to generate the trapping and repump frequencies in a single beam.) The Zeeman slower also requires trapping and repump frequencies, but at a larger detuning because it is slowing atoms originating from a 400°C oven. The Zeeman frequencies are generated by picking off some light after the EOM and shifting it down in frequency 80 MHz using an AOM. Figure 3.6 shows the ${}^7\text{Li}$ locking signal with position of the trapping beam frequency and the output of the spectrum analyzer that monitors the repump sideband.

The other stable Li isotope is ${}^6\text{Li}$. Should interest in fermionic LiRb arise, it would likely require an isotopically enriched or pure sample to be placed in the Li oven because ${}^6\text{Li}$ is only 8% abundant [88]. The $2S_{1/2}$ hyperfine splitting of ${}^6\text{Li}$ is only 228 MHz, so a single pass 200 MHz AOM could be used to lock to a ${}^6\text{Li}$ transition, or one could lock to a $2P_{1/2}$ transition as the ${}^7\text{Li}$ D_1 line is about the same frequency as the ${}^6\text{Li}$ D_2 line (670.96 nm) [91]. An EOM (or some form of frequency modulation) is still the easiest way to generate a repump frequency despite the low frequency separation because while an AOM could produce the repump frequency, it would still have to be combined with the trapping frequency on a non-polarizing beam splitter, reducing the power available.

(a) ${}^7\text{Li}$ locking scheme.

(b) Repump generated by EOM.

Figure 3.6. Frequencies for the Li MOT. We pick off light from the TA and downshift it by double passing it through an AOM. The downshifted light is locked to the 1-2 crossover in the Li saturated absorption signal so that the light from the TA is red detuned from the $F = 2$ transition, indicated by the dashed line. The EOM generates a sideband red detuned from the $F = 1$ transition 803.5 away. The EOM frequency is usually 825 MHz. Best MOT operation occurs when sidebands have about half as much power as the carrier, as monitored by a 2 GHz Fabry-Perot spectrum analyzer.

Electronics for AOM and EOM control

Because the frequencies of many lasers are controlled via AOMs and an EOM, we created an electronic board to provide RF controls. Shown in figure 3.7, the board consists of 8 RF outputs. 6 of the 8 channels consist of a voltage controlled oscillator (VCO), followed by an RF switch, followed by a voltage variable attenuator (VVA). The VCO and VVA control the frequency shift and diffraction efficiency respectively for each AOM. (Or the sideband frequency and modulation depth in the case of an EOM.) The RF switches allow for the beams to be turned on and off quickly should experimental timing be important to the experiment. The remaining 2 channels are simply VCOs to control AOMs that do not need temporal or diffraction efficiency control. The board was designed so that the RF traces would act as $50\ \Omega$ transmission lines (usually called microstrips on printed circuit boards) by controlling their width. There are several programs available for calculating proper microstrip dimensions based on the type of design being used.



Figure 3.7. The board used to control the AOMs in our setup (right) can be thought of as a series of channels (left) with a VCO, RF Switch, VVA on the board, with a high power amplifier driving an AOM after the board. The devices can be controlled by outputs coming from a data acquisition system programmed by a computer.

All the RF components come from Minicircuits. The RF switches used are SWMA-2-50DR+. The VCOs used to control the frequencies are ROS-100+ and ROS-300+ for the 80 and 200 MHz AOMs respectively. The VVA used is the RVA-800+. One channel can be configured for an 800 MHz VCO (ROS-850-719+) to control the EOM. This channel requires a different supply voltage and a VVA that works at higher frequencies (RVA-2000+). The VCO and VVA inputs are generated by a National Instruments PXI-6723 Analog Output card which is controlled in software by programs written in G for LabView. The outputs go through differential amplifiers configured for a gain of 10 to reduce noise, isolate the ground plane of the board, and because the VCO input range is 0–15 V, while the analog output range is from -10–+10 V. The output of the PXI-6723 was found to be susceptible to sources of electrical noise around the lab. Capacitors were used to filter out AC noise and transients, and reduce the linewidth of the output. The analog outputs have the capability to be dynamically changed, as long as the frequency of the control signal is less than 10 kHz. The RF switches are controlled by a PXIe-6341 data acquisition card. It can be used to control the timing down to 1 μ s. The digital inputs are isolated from the board by using an Analog Devices ADuM 1400 Quad-Channel Digital Isolator. Tantalum capacitors were added to the voltage regulators that power the chips. Prior to this change, there were issues with the RF switches failing. Any future redesign of this board should incorporate these capacitors and a strong low pass filter on the VCO input, which were not originally included.

The outputs from the RF control board are amplified by Minicircuits ZHL-32A or ZHL-1A amplifiers depending on whether it is an 80 or 200 MHz signal. The cost of board fabrication and components is about \$300, and the cost of each amplifier is \$230. Most commercially sold AOM drivers cost about \$700 per AOM. While the board is capable of controlling the EOM as well via an amplified 800 MHz VCO, this resulted in substantially lower MOT density compared to a commercial oscillator or frequency synthesizer. The cause of this density reduction is unknown, but may have to do with noise on the VCO signal. Possibly, a more stable voltage source to control

the VCO would fix this issue and remove the need for a frequency synthesizer. The board was designed with assistance from former REU student Roger Ding.

3.1.2 Generating Repump Frequencies for Lithium

As noted earlier the Li repump light must have the same polarization as, be of comparable intensity to, and be present from same directions as the trapping beam. The easiest way to ensure this is to use an EOM to add repump sidebands to the main trapping frequency. However, at one point the EOM used for this purpose was damaged and no longer usable and a replacement would have cost over \$5000. So alternative methods of producing repump frequencies were investigated. In the end, another EOM, slightly modified, proved sufficient. The fact that it severely deforms the beam profile was irrelevant as the PM fiber spatially filters the beam, allowing for stable MOT operation — provided coupling efficiency into the fiber is high enough.

The original and current EOM were made at JILA. The EOM crystal is part of an RF transmission line, with a copper case acting as a ground plane and a conducting strip on top. In the original EOM, the RF signal was sent to a high power $50\ \Omega$ terminator after the crystal. The original crystal was smaller, so the required electric field could be generated at lower RF powers. The replacement EOM is not terminated at $50\ \Omega$, rather the RF signal is reflected back to create a standing wave. The replacement EOM is larger, requiring a stronger RF signal to produce the same modulation depth. As long as the crystal sits at an antinode of the standing wave, the electric field is effectively doubled, reducing the required RF power. This technique requires an RF isolator between the amplifier and the EOM crystal to prevent 10 W or more of RF power being reflected back into the amplifier.

Commercial EOMs generally place the crystal in an RF resonator. It allows for the desired modulation depth at a fraction of the RF power, but limits the use of the EOM to a specific frequency range. Companies that sell suitable EOMs include Newport (Model # 4421-02) and Qubig (Model # EO-Li7-3K). The disadvantage of

resonator EOMs is that a different model would be needed for ${}^6\text{Li}$. It is possible that current modulation may be more effective at the lower frequency of 228 MHz, where it is not a realistic option at 803 MHz. This is, however, unlikely.

An attempt was made by our group to build our own EOMs as a batch of the crystals can be grown and coated for a fraction of the cost of a commercial EOM. Initially, to make them easy to assemble, a piece of copper was machined to sit on top of the crystal to act as the top of a the transmission line while the crystal would sit on a copper base that would act as the ground plane and all the parts could be screwed into place. However, the thickness of the copper on top of the crystal meant that it did not behave as a $50\ \Omega$ transmission line due to the skin effect and a significant amount of power was reflected. Using a copper tape instead of a machined piece of copper on top of the crystal improved transmission somewhat, but the modulation depth was still well below what was expected. Also, soldering a connection from the pin of an SMA connector to the copper tape would often result in damaging or optically degrading the face of the crystal. While this route was ultimately abandoned, perhaps gluing the SMA pin to the top of the metalized surface of the crystal using a conducting adhesive or finding another method of making the crystal behave as a transmission line could have fixed the issue.

Current Modulation

Sidebands can be added to a carrier frequency without an EOM by modulating the injection current of the diode laser. This would modulate the amplitude and frequency of the laser, leading to sidebands similar in characteristic to equation 3.1 but with asymmetry in the positive and negative order peaks that arise due to the additional amplitude modulation. With home built diode lasers this can be accomplished with a bias T. Commercial laser current supplies often have a modulation input that handle modulation in the kHz range. For RF frequencies in the MHz and GHz range, one would need to add a bias T and alter the connections of the commercial laser to

include a bias T — the DL Pro has a modulation input that can be configured as a bias T on the laser head itself for high frequency modulation. When employing current modulation, it is important to ensure that $I_{DC} + I_m < I_{max}$ where I_{DC} is DC current supplied, I_m is the amplitude of the RF current, and I_{max} is the maximum current rating of the diode. Because the bias T is placed as close to the laser as possible (i.e. after the current controller), there are no controls in place to ensure the laser’s current rating is not being exceeded by the output of the T. The DL Pro’s modulation input was not 50Ω so it was difficult to pinpoint I_m as a good deal of the RF signal was likely reflected, not making it to the diode.

Another important note is that like any laser cavity, ECDLs operate at frequencies that are integer multiples of the free spectral range (FSR) of the cavity, $\nu_{FSR} = c/2l$, where l is the length of the cavity. If the current is modulated at a frequency not equal to ν_{FSR} then the sidebands will be suppressed as they are not resonant with the laser cavity. A cavity length of about 18.5 cm would be required to match ν_{FSR} to the ${}^7\text{Li } 2S_{1/2}$ hyperfine splitting. Such a long cavity is not feasible in an ECDL as it would be too difficult to stabilize. Gratings in ECDL’s are generally placed a few cm from the diode. Some groups use current modulation to produce ${}^{85}\text{Rb}$ or ${}^{87}\text{Rb}$ MOTs with a single beam, but the cavity lengths would only be 5 and 2.5 cm respectively, which is more reasonable. If the Li MOT did not require the repump to have a comparable intensity to the trapping frequency, the suppression of sidebands in the cavity would be less of an issue. In ${}^{85}\text{Rb}$, the modulation depth needed would be minimal because the repump frequency would not require much power — matching the cavity length to the hyperfine splitting would not likely be necessary. Attempts to modulate the current of the DL Pro at 800 MHz resulted in first order sidebands with only a few percent of the total power, not sufficient for our purposes.

660 nm diodes

While inexpensive 670 nm diode may not be available at powers needed to seed the TA, 660 nm diodes, with powers up to 150 mW are available for well under \$100. Indeed, some groups working with Li use these diodes for their MOT lasers. However, there are drawbacks. First they must be temperature tuned (heated) to raise their operating frequency a full 10 nm. This usually requires an operating temperature of 50–65°C. Even if they can be heated to this temperature, operating at the edge of temperature specifications will shorten the life of the diode and also the life of the TEC controlling the temperature. Secondly, heating the diode reduces the maximum output power substantially. We tested three 660 nm LDs to see if/how they would perform at 670 nm: the Opnext (Hitachi) HL6545MG, the QPhotonics QLD-660-80S, and the Mitsubishi ML101J27-01. The QLD-660-80S had to be heated beyond its specification of 50°C and died after a few days of use. The HL6545MG and ML101J27-01 had maximum temperature specifications of 75°C and could be heated to operate at 670 nm. The HL6545MG had the better temperature tuning characteristic and only needed to be heated to 55°C while the ML101J27-01 needed to be at 65°C to run at 670 nm. While the HL6545MG has a rated output of 130 mW at room temperature, it drops to around 45 mW at 55°C. One can build ECDL's from these diodes for pump and repump light, but separate lasers are preferably combined on a polarizing beam splitter (PBS) so that the resulting power is the sum of the inputs. Because Li pump and repump beams must have the same polarization, they must be combined on a non-polarizing beam splitter, which would limit to the maximum power of a trapping/repump combination to essentially the power of a single diode laser.

Dual Frequency Injection of a Tapered Amplifier and Laser Diode

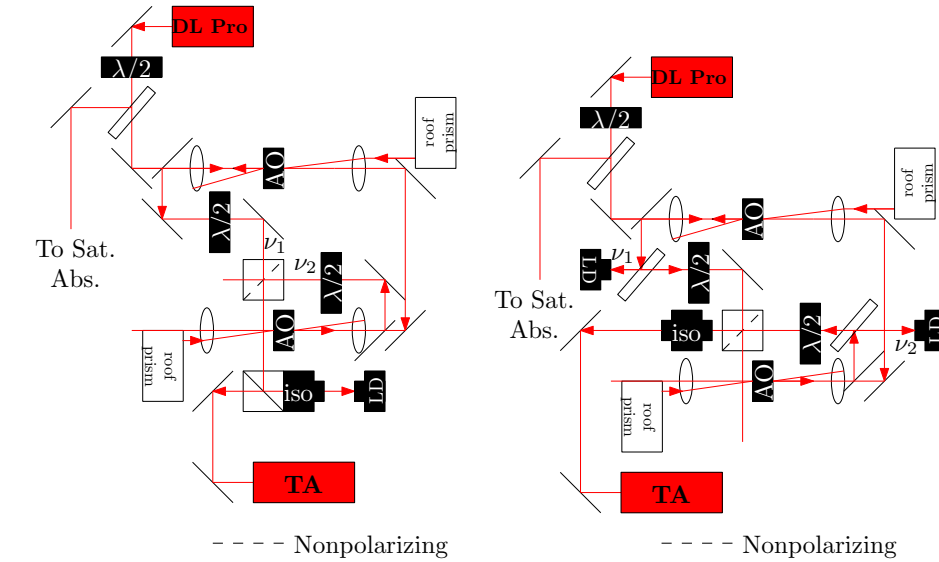
When it appeared that an EOM would not be viable for producing repump sidebands, we investigated using 660 nm diodes to produce the trapping and repump

frequencies. A TA can be seeded by multiple frequencies and will amplify both, sometimes many nanometers apart if the TA has a wide bandwidth, as was demonstrated by Goldwin *et al.*, who used a single TA in a dual species K/Rb trap [97]. If the frequencies are separated by less than 2 GHz, sidebands begin to appear likely due to beating between the injected frequencies [98,99]. The TA will output frequencies at the injected frequencies ν_1 and ν_2 ($\nu_2 > \nu_1$) and at sideband frequencies at $\nu_1 - n\delta$ and $\nu_2 + n\delta$ where $\delta = \nu_2 - \nu_1$ and n is an integer. We observed this when the TA was used to amplify both trap and repump frequencies at the same time. Instead of building a second ECDL to generate the second frequency, which would require a second optical isolator and a second saturated absorption setup, injection locking techniques were explored.

Details of various injection locking techniques can be found in Arthur Mills thesis [87], but we simply injected about 0.2–0.4 mW of power into free running diodes, as we had spare housings, current controllers, and temperature controllers. When aligned properly, the free running diode will take on the properties of the injected light. The alignment procedure is very similar to the process of aligning the feedback in an ECDL. When the 660 nm heated to operate at close to 670 nm, they could be injected with light from the DL Pro and take on its single mode narrow linewidth properties. The main issue when injection locking is that the slave LD will remain locked to master while being run at a current slightly above threshold. At higher current, the internal modes of the slave laser can become dominant, but tuning the current can periodically bring internal mode of the slave laser back to one compatible with the master laser. For the LDs we used, this happened about every 10 mA. The capture region where the slave diode would follow the master was about 1 mA. The capture region would depend on the temperature of the slave and the alignment and power of the injected beam. If any of these were to drift over time, so would the capture region — an issue that eventually led us to going back to an EOM to generate sidebands.

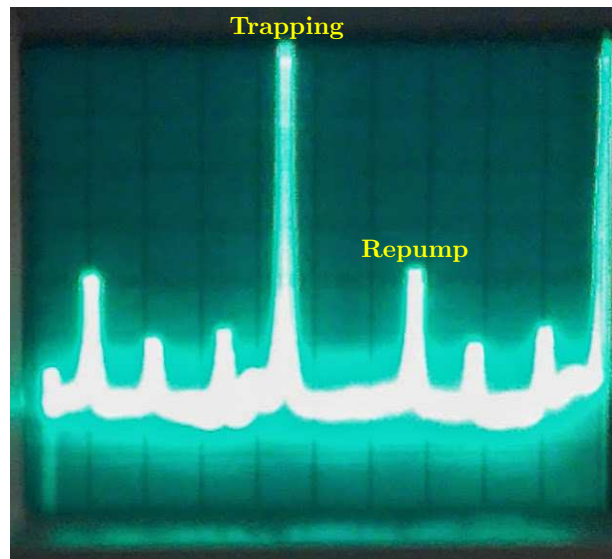
In our first scheme, we tried to injection lock a single diode with two frequencies and amplify its output with the TA. Dual frequency amplification using a single LD has been previously demonstrated by Booth *et al.* [99]. The scheme is shown in figure 3.8(a). We locked the DL Pro to the ${}^7\text{Li}$ D₂ line's crossover resonance and double passed it through two 200 MHz AOMs to shift the light to the desired trapping and repump frequencies, which were combined and injected into a single LD. The four wave mixing (FWM) effect seen by Booth *et al.* was observed as the LD produced extra frequencies at $\nu_1 - n\delta$ and $\nu_2 + n\delta$ similar to when a TA amplifies multiple frequencies. The amount of power in the extra frequencies depends on the energy difference and decreases as $\nu_2 - \nu_1$ increases. We controlled the power in each frequency by varying the amount of injected power from the input beams. In the end, the scheme would not work for us because there was a discontinuity where ν_2 or ν_1 became the dominant frequency amplified as the injected powers were changed. It proved impossible to stably injection lock a single LD with two frequencies such that the relative powers of the amplified frequencies were comparable. It is possible that the ability to tune the relative power in the two frequencies depends on the diode chosen. The QLD-660-80S diode seemed to behave more stably in terms of relative power in ν_1 and ν_2 , but it was unusable at 670 nm because it could not be heated to high enough temperatures without damaging the diode. The HL6545MG and the ML101J27-01 both exhibited the discontinuous tuning of relative power, making them unsuitable for producing both frequencies in a single diode. Note that in order to incorporate an optical isolator for the injected LD, the polarizing element was removed and replaced with a PBS that served as a input/rejection port.

Since a second spare diode housing and controllers were available we tried a more conventional approach where the two frequencies generated by AOMs were used to inject two different free running diodes (figure 3.8(b)). Frequencies were generated the same way but instead we injection locked two separate LDs which allowed better control of the relative trapping and repump power. The two outputs were combined and amplified in the TA. This method was used to generate a Li MOT successfully



(a) Injection locking a LD with 2 frequencies.

(b) Injection locking two LDs.



(c) 2 GHz spectrum analyzer monitoring the TA.

Figure 3.8. Two schemes for generating trapping and repump frequencies for the Li MOT. Both a LD and a TA will amplify multiple frequencies, but the output will have extra sidebands due to FWM effects. These extra sidebands are diminished when $\nu_2 - \nu_1$ is large. (c) shows a snapshot of a phosphor oscilloscope monitoring showing the signal from a spectrum analyzer monitoring the output the TA in (b). A similar result is seen for (a) but with less control over the relative power in the trapping and repump.

for several months, but there was an issue where the injection lock would break after random intervals of time. It is nearly impossible to do cold molecule spectroscopy if a MOT cannot reliably be maintained for extended periods of time. It was later found that the diffraction efficiency of one of the 200 MHz AOMs being used, which was already observed to be lower than it should, was actually fluctuating over extended periods of time. This may have been causing the slave laser current required to maintain an injection lock to drift, and without a way to compensate, the lock would simply break. It is not known definitively if replacing this AOM would have fixed the problem, as it was not discovered until after we returned to using an EOM to generate a repump sideband and a spare 200 MHz AOM was unavailable, but injection locking is a widely used technique to amplify laser frequencies.

3.1.3 MOT Setup

The details of cooling and trapping atoms in a MOT was discussed in Chapter 2. Once all the beams have been combined, they are sent through a PM fiber to the vacuum system to create the MOT. The details of the optics in our MOT setup is shown in figure 3.9. After the PM fiber, the beams are expanded to a 1" diameter. Rather than splitting the light into six beams, we split into three and retroreflect the three x-y-z beams to provide the needed light from six directions (two for each dimension of cooling and trapping). $\lambda/2$ waveplates and PBSs are used to ensure equal power is in each of three beams. The Rb repump beam has orthogonal polarization allowing it to be separated. Once separated a fill-in repump beam is split off and recombined on the original beam splitter while other x-y repump beams are expanded to 1" and have a dark spot mask placed in the middle of the beam. When a dark Rb MOT is desired, the fill-in is blocked so that the atoms in the middle of the MOT will fall into the dark hyperfine state and remain there, reducing MOT fluorescence and keeping most Rb atoms in the ground $5S_{1/2}$ state.

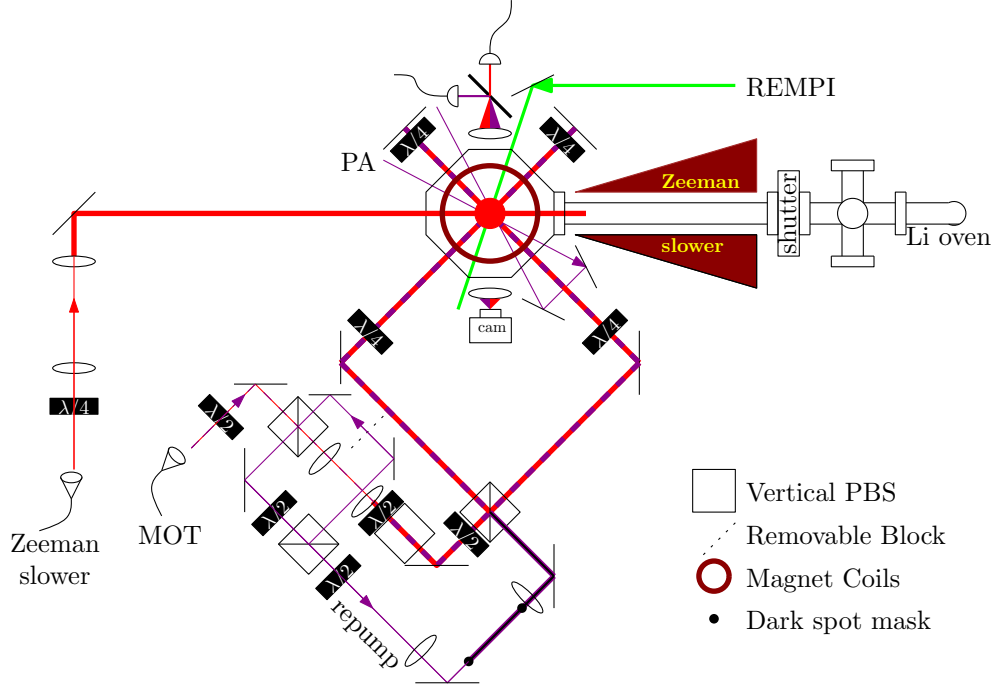


Figure 3.9. Schematic of lasers, optics, and magnetic coils (Zeeman and MOT) for MOT.

Different experiments required running the dual species in different conditions. For example to study the collisions between Li and Rb, the Rb was operated as a normal MOT (or “bright” MOT to contrast with a dark MOT where the fluorescence is suppressed). Measuring the atom number and densities also requires a bright MOT, because the atom number calculation is based on MOT fluorescence. A lens can collect MOT fluorescence onto a photodiode, and the atom number can be calculated by

$$N = \frac{\Omega}{4\pi} \gamma_p \quad (3.2)$$

where Ω is the solid angle the lens subtends ($\frac{\Omega}{4\pi} \approx \frac{(d/2)^2}{4l^2}$, where d is the diameter of the lens and l is its distance from the MOT), and γ_p is the scattering rate from equation 2.6. Parameters for other measurements taken using the dual species MOT can be found in the theses of Adeel Altaf and Sourav Dutta [55, 83]. For the experiments described in this thesis, the MOT was optimized to maximize the number of ions detected. This means a dark Rb MOT was used to suppress collisional losses.

The Li MOT was optimized for maximum atom number. The MOT coil current that optimized molecule production as measured by ion counting was 3.75 A, although little difference was seen between 3.5–4 A. The detuning and power of each MOT beam that optimizes ion counts is shown in table 3.1. Previous measurements estimate we trap 5×10^7 Li atoms at a density of $5 \times 10^9 \text{ cm}^{-3}$ and 1×10^8 Rb atoms at a density of $4 \times 10^9 \text{ cm}^{-3}$. The temperature of the Li MOT has an upper limit of 1.1 mK and the Rb MOT is a few hundred μK [13, 55].

Table 3.1

Frequency and power parameters for MOT lasers. These detuning (Δ) and power parameters optimize PA signal as measured by ion counts. Note that the Rb Repump detuning is for a bright MOT. Our method of creating a dark MOT is to lock to a different transition so that the repump is blue detuned and to block the repump beam from the middle of the MOT. The measured power of the Li beams consists of the combined power of the carrier and sidebands created by the EOM.

Beam	$F \rightarrow F'$	Δ (MHz)	RF (MHz)	Power (mw)
Rb Trap	$3 \rightarrow 4$	-19	73	100
Rb Repump	$2 \rightarrow 3$	-2	76	25
Li Trap	$2 \rightarrow 3$	-24	213	50
Li Repump	$1 \rightarrow 2$	-13	825	
Zeeman	$1, 2 \rightarrow 2, 3$	-104	80	30

3.2 Photoassociation Laser System

The PA laser field is generated by a Coherent 899-21 titanium:sapphire (Ti:S) ring laser, pumped by a 532 nm 8W Sprout-G laser from Lighthouse Photonics. The mid range optics were used in the Ti:S laser cavity which give a tuning range of roughly 800–900 nm, but still gives sufficient power down to about 775 nm. At 780 nm, a 5 W pump can give about 350 mW of power, with more available at longer wavelength.

3.2.1 Frequency Comb Assisted Spectroscopy

Work on developing frequency combs resulted in Nobel Prizes for Hall and Hänsch in 2005. A review of frequency comb details and uses can be found in a review article by Margolis [100]. A frequency comb is created when two frequency components of a femtosecond pulsed laser an octave apart are locked to produce a stable beat frequency so that in the frequency domain, there is a stable “comb” of frequencies

$$f_n = nf_{rep} + f_0 \quad (3.3)$$

where f_{rep} is the repetition rate of the pulsed laser and f_0 is the offset beat frequency. The Menlo comb’s main output is in the infrared 1000–1700 nm range, but an amplified signal from a second harmonic generator can result in visible and near infra red output from 450–1000 nm range. The second harmonic generation has the effect of doubling the observed frequency offset so that $f_n = nf_{rep} + 2f_0$. The Menlo system is usually set at $f_{rep} = 250$ MHz and $f_0 = 20$ MHz.

When the Ti:S is combined with the comb output on a PDA-10A (bandwidth 150 MHz) photodiode from Thorlabs, we are able to monitor a beat signal that satisfies

$$f_{laser} = nf_{rep} \pm 2f_0 \pm f_{beat}. \quad (3.4)$$

A wavelength meter accurate to within 250 MHz can pinpoint the value of n and tuning the laser frequency can determine the signs of f_0 and f_{beat} . MHz level accuracy is not often required for molecular spectroscopy, so often just a wavelength meter is sufficient for measurements when the PA laser is scanned. The frequency comb beat signal is useful when the PA laser is to be kept at a fixed frequency. The cavity to which the Ti:S is locked is only passively controlled by heating it and the laser can drift over time. Monitoring the beat signal can ensure reproducibility of the PA frequency and periodic adjustments can keep it within 5–10 MHz of the desired frequency. A circuit based on RF electronics could be designed to keep the beat signal fixed at a given frequency, but the drift in PA frequency is slow over time and can be accounted for with periodic graduate student feedback. The beat signal between

the frequency comb and the Ti:S laser is usually between -50 and -30 dBm. (See figure 3.10(b).) Beat signals between teeth of the comb are much stronger and are clearly seen at 250 and 500 MHz despite being well beyond the bandwidth of the detector.

Potential uses of the frequency comb extend beyond simply measuring our PA laser. In the future it could possibly be used to phase lock lasers hundreds of nanometers apart, to drive molecules into the absolute ground state via stimulated Raman adiabatic passage (STIRAP), as was done in KRb [21]. In this case, the repetition rate and offset frequency would have to be tuned so that teeth of the comb existed at each of the desired STIRAP frequencies.

3.3 Ionization Laser

The ionization laser is a Quanta-Ray PDL-2 Pulsed Dye Laser pumped by a Quanta Ray PRO-Series Pulsed Nd:YAG Lab-190 10 Hz Laser. The second harmonic of the YAG is a 532 nm output, sufficient for pumping several dyes. We have generally relied on rhodamine 590 (R590) and rhodamine 610 (R610) dyes for molecular spectroscopy. R590 covers roughly from 16,400–17,200 cm^{-1} (roughly 580–610 nm) and R610 covers from 17,200–18,000 cm^{-1} (555–580 nm). These dyes generally have a much longer lifetime compared to other available dyes and are readily available, making them convenient to use as long as molecular states are accessible in those ranges. Numerous states are accessible for LiRb in this region, but since the light from a pulse is intended to ionize a molecule through a two photon process, we must make sure that a two photon transition has enough energy to ionize a molecule for the states we are populating.

The wavelength of the PDL is controlled by a Superior Electric Slo-Syn M061-FC02E stepping motor that rotates a grating. When disengaged, the stepper can simply be turned by hand to tune the laser. When engaged, it is controlled by a Superior Electric SD200 Step Motor Drive Module. The minimum step size in energy

depends on the dye being used (about 0.07 cm^{-1} for R590), but regardless of the dye used, it is comparable to the PDL output bandwidth ($> 0.1 \text{ cm}^{-1}$). While stepping through frequencies, the step must be synchronized to the 10 Hz output of the YAG. This will be covered in more detail when discussing the timing of the ion detection system.

3.4 Vacuum System and Ion Detection

The vacuum system was largely designed by Sourav Dutta. Details about the main components (lithium oven, atomic beam/Zeeman slower, atom trapping region, and time-of-flight (TOF) mass spectrometer) can be found in his thesis [83]. A schematic is shown in figure 3.11 and we simply highlight the features in this section. A collimated atomic lithium beam is formed from a lithium oven where the vapor can only escape through packed hypodermic needles. This technique was also employed in the thesis of Dionysios Antypas [96]. The Li atom beam passes through the Zeeman slower into the MOT region. The slower ensures the majority of Li atoms slowed enough to be captured by the MOT upon entering the main chamber. The materials that were available at the time of the slower's construction causes do not allow for very efficient cooling. The inner part of the coil that is in contact with the vacuum system gets quite hot when the coils are on for an extended period of time, even with water cooling the exterior of the coils. Care needs to be taken to ensure that this does not adversely affect the vacuum quality or that repeated thermal expansion and contraction causes a vacuum leak. The window that gives optical access to the Zeeman beam becomes coated by Li over time. If it is only partially coated, it can be heated to remove some of the Li coating. A UV source shining on the window can also help remove the Li coating, but this should only be done while the ion detection equipment is off as the UV light can ionize vapor inside the vacuum. If the window becomes too coated, it will require replacement which involves the time consuming process of breaking vacuum.

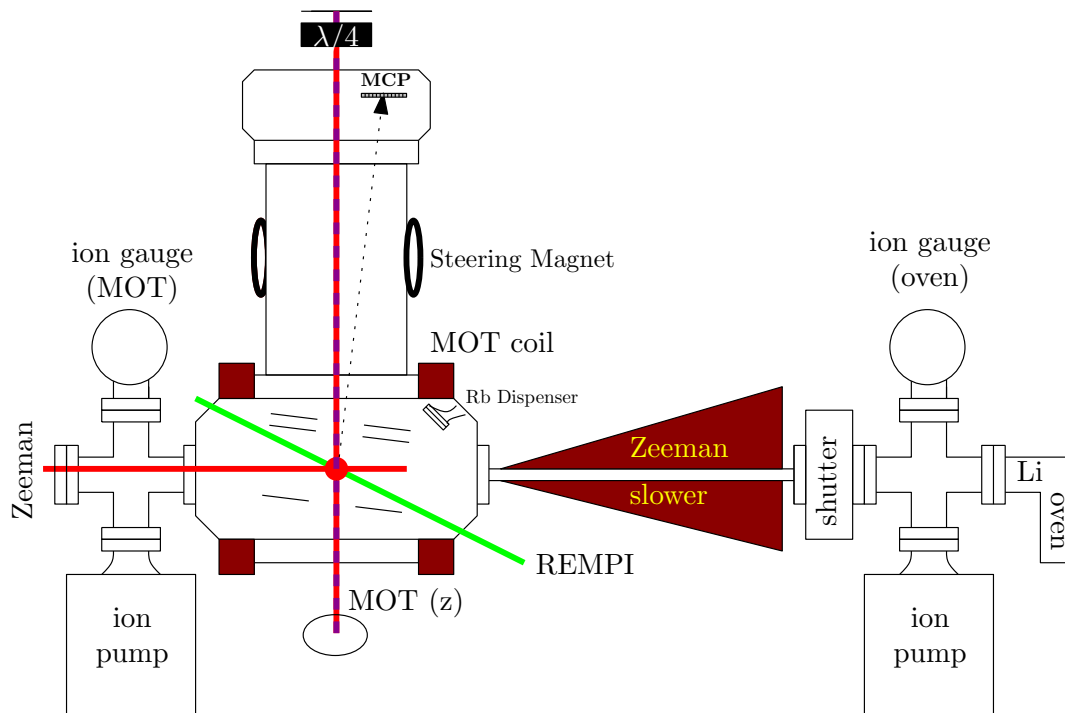


Figure 3.11. Schematic of vacuum system setup for Dual Species MOT and TOF mass spectrometer.

The trapping region is in the middle of Extended Spherical Octagon vacuum chamber from Kimball Physics (Part #MCF800-ExtOct-G2C8A16). It has optical access for the MOT beams, the PA beam, the ionization beam, with access left over for MOT imaging, fluorescence detection, and future dipole trap beams. Above and below the chamber are coils to produce the MOT's octopole magnetic field. Within the chamber are field plates mounted for the TOF mass spectrometer. The lower and middle plates are set at 400 and 340 V respectively to sweep the positive ions upward. The top plate is grounded to create an acceleration region. Above the MOT chamber is the TOF chamber. At the top of the TOF region is a Chevron type matched pair of micro-channel plates (MCPs) manufactured by Tectra Physikalische Instrumente to amplify the ion signal. The resistance between plates should be 330 M Ω when they are functioning properly. The plates are mounted at an angle so that the MCPs

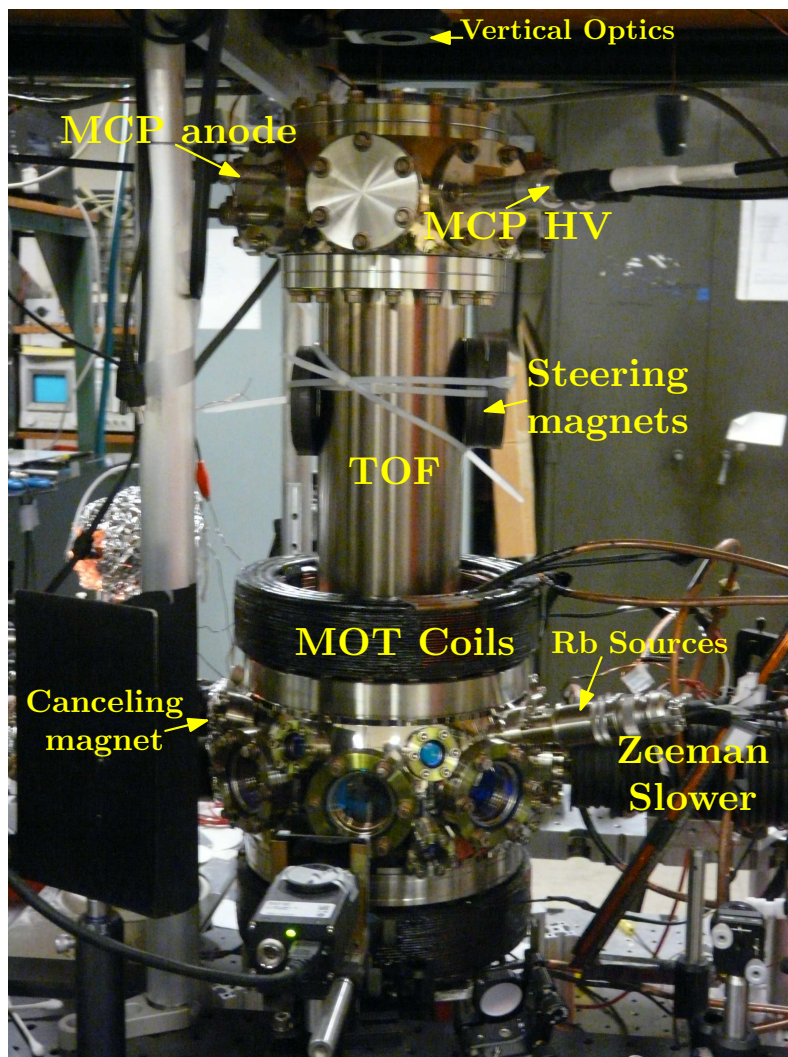


Figure 3.12. Photo showing important components of the vacuum system.

can be mounted to the side, allowing access for the vertical MOT beams. Photos are shown in figure 3.12 and 3.13.

The mass spectrometer is required because each pulse from the dye laser is capable of creating Li^+ , Rb^+ , Rb_2^+ and LiRb^+ ions with each shot. Thus an ion detected by the MCPs is only meaningful if it arrives at time t_{LiRb} where t_{LiRb} is the measured time from the generation of the YAG pulse to a LiRb^+ ion signal being detected by the MCPs determined based on its time of flight. Arrival times for other atomic ions (t_{Li} and t_{Rb}) can be measured unambiguously by ionizing the atoms with a dye laser

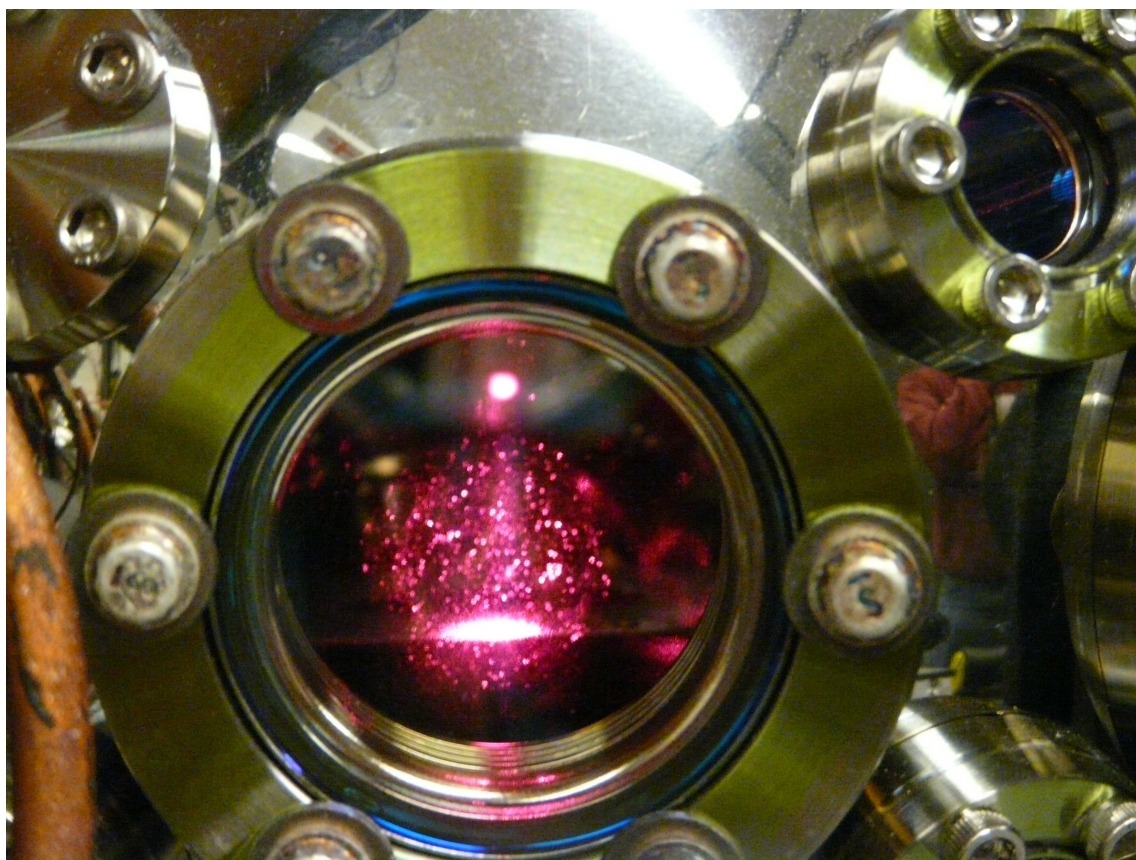


Figure 3.13. Photo of Li atom cloud hovering over the bottom electric field plate.

pulse without the other species present and without a PA beam present. It has been shown in previous experiments that the light required to trap Rb in a MOT will also photoassociate some Rb₂ molecules [101, 102]. This is a small loss mechanism for Rb MOTs, but it does result in the presence of an ion signal at $t_{\text{Rb}_2} = \sqrt{2}t_{\text{Rb}}$.

Because ⁷Li is very light compared to ⁸⁵Rb there was some concern about the ability to differentiate between the Rb⁺ signal and LiRb⁺ signal, as was the case in the detection of LiCs [26]. The mass ratio of ⁷Li⁸⁵Rb to ⁸⁵Rb is 1.08 meaning that LiRb should arrive at $\sqrt{1.08}t_{\text{Rb}} = 1.04t_{\text{Rb}}$. The spread in arrival times for a given species, δt determines if the Rb and LiRb can be distinguished. If the peaks overlap, *ie.* if $t_{\text{Rb}} + \delta t_{\text{Rb}}/2 > t_{\text{LiRb}} - \delta t_{\text{LiRb}}/2$, then there can be ambiguity as to which species of ion is arriving at a given time, but this is not the case for our system. Analysis of ion arrival times and spread in arrival times is covered in more detail in Chapter 2 of Adeel Altaf's thesis [55]. For the field plate voltages noted earlier, $t_{\text{Rb}} = 20.1 \mu\text{s}$ and $t_{\text{LiRb}} = 20.9 \mu\text{s}$. The spread in both is less than 150 ns, meaning the two signals are quite well resolved. Figure 3.14 shows the resolved Rb⁺ and LiRb⁺ arrival on an oscilloscope.

The number of ions that produce signal above our noise threshold depends on the gain the MCP provides for each ion that strikes it, which depends on their operating potential difference. They can be run at a potential as high as 2 kV. Ions start to be detected as low as 1.5 kV. The signal increases nonlinearly from 1.5–2 kV. We typically use the MCPs at 1.8 kV (lower MCP -1.9 kV; upper at -0.1 kV) because the counting statistics show minimal improvement when increased further. Running the MCPs at lower voltages reduces the chances they will somehow be damaged and increases the lifetime. The MCPs must be turned on in a controlled manner to avoid damage from current runaway. The potential must be stepped up incrementally with several minutes of waiting in between steps. The procedure can be found in their manual. As this procedure can take several hours, it has been automated using a LabView program to send a signal from the PXI-6723 to the Bertan Series 230 high voltage power supply which can be controlled externally. The high voltage supply

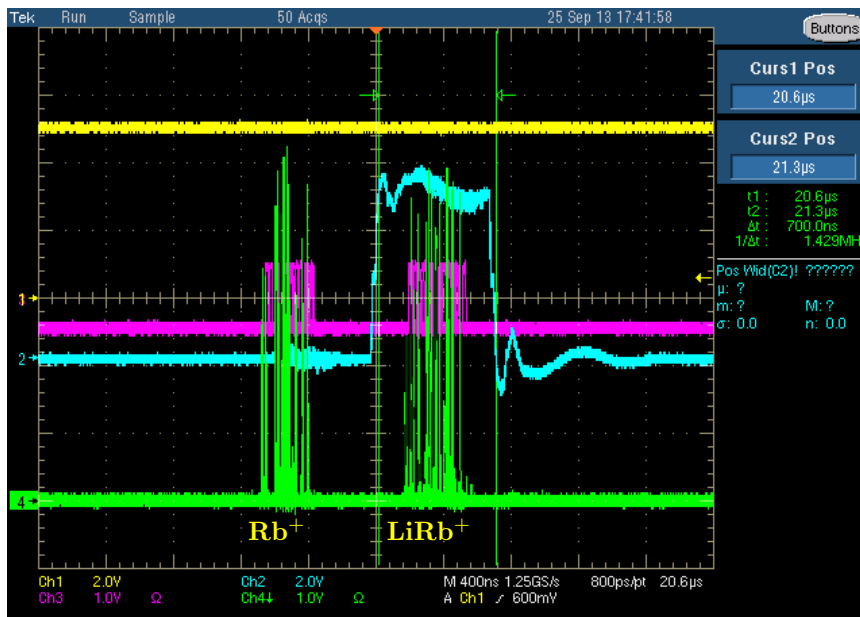


Figure 3.14. Image of oscilloscope monitoring the arrival of ions to the MCPs. The Li^+ and LiRb^+ signals are clearly resolved. The yellow trace is the Q-Switch monitor for the YAG that determines $t = 0$. The green trace is the MCP signal after amplification. The purple trace is the discriminator output. The cyan trace is the gate signal which sets the time interval during which ions are counted. It has been set to count LiRb^+ .

generates an output which is 1000 times the input control voltage, so that a 2 V signal corresponds to a ± 2 kV output depending on whether the supply is configured for positive or negative output.

The program also safely ramps the MCPs down when the system is not in use. The ramp cycle start or restart can be delayed so that it starts hours or days later after ready for its next use, rather than requiring a 2–3 hour wait each time it they need to be turned on. The turn on can be bypassed in the event the MCP control program crashes. The National Instruments cards retain the value of their last output unless the PXI chassis or computer is shut off, so should the program crash while the MCPs are in use, the program's previous setting (which can be read off the Bertan supply) can be directly output bypassing the long start up procedure. Bypassing

the turn on procedure when the MCPs are at 0 V is dangerous and can irreparably damage the MCPs. Should the computer crash the output of all analog and digital outputs resets to 0. If this happen while the MCPs are being externally controlled, the abrupt drop to 0 V, while not ideal, should not damage the MCPs. They can simply be ramped back up safely from 0 V.

3.5 Ion Counting Electronics

The pulse amplitude that the MCP generates can differ by over an order of magnitude from pulse to pulse. These large fluctuations can be averaged out when many ions are being produced in each pulse, but since we produce only a small number of LiRb per pulse (< 2 except for the strongest transitions), it can be misleading to simply average the signal over each detection window as one detection could yield more signal than the next 10 combined. We choose rather to count the number of pulses generated by the MCPs within a given arrival window to determine the number of ions detected.

First, we amplify the MCP signal so that each pulse associated with an ion arrival is easily distinguished above the background noise. We tried building a high speed transimpedance amplifier circuit appropriate for amplifying the MCP signal following the design from reference [103]. Our goal was to be able to amplify the signal from an arriving ion so that the width of the amplified peak was on the order of 10 ns. We tried a number of different op-amp models, with passive components used to reduce ringing that often comes with fast op amps, but we were unable to design a circuit that met our requirements for speed and stability using off the shelf op-amps.

In the end, we used amplifiers from a nuclear instrumentation module (NIM) rack. The NIM amplifiers (Ortec model #420-C) are fast and have a fixed gain of 20. We pass the signal through two amplifiers for a gain of 400. To turn peaks of varying strength into a countable pulse train, we send the amplified signal to a discriminator, also on the NIM rack (LeCroy model #821). Any time the amplified

MCP signal exceeds a threshold, the discriminator produces a NIM logic pulse of a controllable width and fixed amplitude. To count the number of ion pulses produced we use the counter/timer that is part of the NI PXIe-6341 card. There are four TTL counter/timers that have a timebase of 100 MHz on the card. NIM logic levels are different from the 0/5 V of TTL, so the NIM signal must be converted to TTL somehow before being read by the DAQ card. The LOW/HIGH levels in NIM logic has a 0.8 V separation, which is identical to the difference in emitter-coupled logic (ECL). There are chips that can translate ECL logic to TTL logic. We use a Motorola MC10H125PG ECL to TTL translator to convert the output of the discriminator to TTL pulses. To ensure that logic levels from the NIM discriminator match those of ECL, either the DC level of the discriminator output can be adjusted or the MC10H125PG can be configured for differential inputs so that the DC value does not matter. The inputs to the MC10H125PG and oscilloscope must be terminated at 50 Ω to maintain fast pulse counting and ensure that there are no signal reflections that could interfere with pulse counting. The scope can be set to 50 Ω internally, but a resistor across the MC10H125PG inputs is required. A flow chart of the electronics is shown in figure 3.15.

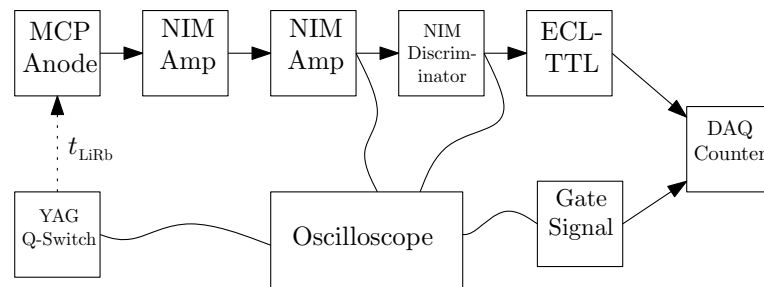


Figure 3.15. Flow chart showing the signal connections for counting ions.

3.5.1 Experimental Timing

To ensure that the pulse counting electronics are in sync with the YAG, a user configurable timing sequence was designed in LabView and output via the PXIe-6341. The YAG lamp and Q-switch can be externally controlled via TTL inputs. Since the YAG can be unstable and possibly be damaged if the oscillator energy is turned up without a 10 Hz signal that discharges the lamp, it is necessary that a LabView program be run in the background that sends a continuous 10 Hz signal that keeps the lamp firing when being controlled externally. The YAG fires on a rising TTL edge. The width of the pulse, t_{lamp} can be of arbitrary length as long as $t_{lamp} < 100$ ms. We use a clock signal generated from a counter/timer on the PXIe-6341 to generate this continuous pulse train. To optimize the YAG output power, the Q-switch must be triggered at an optimal delay time after the lamp discharges. By making the pulse width of the lamp control signal equal to the Q-switch delay time, a TTL pulse set to be triggered on the falling edge of the lamp signal can be used to control the Q-switch. A counter/timer is used for the lamp output so that the Q-switch delay can be controlled to a precision of 10 ns (100 MHz timebase). The optimal delay time was found to be 220 μ s, but that should be periodically rechecked, especially if any adjustment is made to the YAG.

The Q-switch TTL signal is output on a digital output of the PXIe-6341. The digital output has a timebase of 1 MHz, but the length of the Q-switch pulse is arbitrary (we choose 5 ms). By using a digital output instead of a counter, we can output a digital wave that can synchronously control other aspects of the experimental timing that depend on the generation of the ionization pulse determined by the Q-switch. This digital wave can be used to turn any AOM or EOM with an RF switch control on or off, or to switch MOT coils, field plates, etc. on and off if necessary. We briefly discuss how to generate the appropriate digital output.

If we would like to control these signals to within 10 μ s, then an array of length $100 \text{ ms}/10 \mu\text{s} = 10,000$ must be created where an array element is set to output every

10 μs as a digital wave. Since the digital channel is an 8 bit output, the timing of up to 8 experimental devices can be controlled on this channel and synced to the laser pulse. The easiest way to create the array is to create 8 separate arrays for each channel and sum them at the end. HIGH and LOW for each channel is represented by 2^n for HIGH and 0 for LOW, where n is the number of the channel (0–7) that is being controlled. For example, the first 6 bits all control RF switches on the AOM board. For our experiment, all trapping lasers are simply left on continuously, so an array of 10,000 63s (equivalent to adding the first six arrays, $1+2+4+8+16+32$) can be made to indicate all these are to be left on all the time. The seventh bit controls Q-switch. An array of 500 64s (2^6) and 9,500 0s would correspond to a pulse width of 5 ms where the Q-switch fires at the very beginning of the signal. The construction of an array element is shown as follows:

$$1 + 2 + 4 + 8 + 16 + 32 + 64 + 0 = 127 = 01111111_2$$

corresponds to the first seven timing bits being on and the eighth being off — this is what is output while the Q-switch is high. After the Q-switch changes to low, the array elements being output change to

$$1 + 2 + 4 + 8 + 16 + 32 + 0 + 0 = 63 = 00111111_2.$$

The eighth bit can be used for various purposes, such as controlling a shutter for the PA beam. An array of 128s (2^7) and 0s can be added to the array to control when the shutter signal is high (128) and low (0). If additional synchronized timing of instruments is needed in the future, it is not actually necessary to use a digital output to control a device that is always on. An RF switch could be hard wired to a +5 V supply supply available on the PXIe-6341 connector block, so that the digital output can be appropriated for other purposes by changing the output array appropriately. Only one of the PXIe-6341's digital output channels can be used to output a digital wave in this manner. The two other digital channels do not have hardware timing capabilities. The 8 bit digital signal is repeated N times, where N

is a user defined number indicating the number of ion pulses a measurement should be integrated over.

The other important aspect of experimental timing has to do with the time of flight. Because Li, Rb, and Rb₂ ion counts need to be excluded, the counter is gated so that it only counts pulses within a user determined window to be configured to coincide with the arrival of LiRb ions to the MCPs. The amplified MCP and discriminator signals are split so they can be monitored on an oscilloscope. This monitoring is required to ensure our LiRb window is correct and that the discriminator is appropriately set at a level that counts all the LiRb⁺ arrivals without superfluous counts due to other ions. Because this gate needs to be accurate to 100 ns or less, a clock signal generated by the 100 MHz counter/timer is required. To accomplish this, the output line that carries the Q-switch control signal is wired to another terminal on the DAQ that can be used as a trigger. On the rising edge of this trigger from the Q-switch output, a gate signal is generated by using one of the counter/timers as an output. This signal delayed by an amount t_{gate} . The signal has a frequency of 10 Hz (as do all the other signals generated) to match the 10 Hz repetition rate of the YAG. The signal is high for a user specified δt_{gate} during which the arrival of LiRb ions is expected. For the field plate voltages listed earlier, we use $t_{gate} = 20.6 \mu\text{s}$ and $\delta t_{gate} = 700 \text{ ns}$ so that the arrival to LiRb ($t_{\text{LiRb}} = 20.9 \mu\text{s}$, $\delta t_{\text{LiRb}} < 150 \text{ ns}$) is well within the arrival window. Figure 3.16 shows an example timing sequence.

3.5.2 Laser Scanning Control and Calibration

Once the program registers that the timing sequence has been repeated N times, it stops counting and saves the number of counts over N shots. At this point the timing sequence is complete and the ionization laser or PA laser can be stepped depending on the kind of scan being done. The PA laser can be controlled externally by a control signal from -5–+5 V that corresponds to a scan range set on the Ti:Sapphire control box. Usually this is set at 20 GHz. So that a 1 V change in the external signal

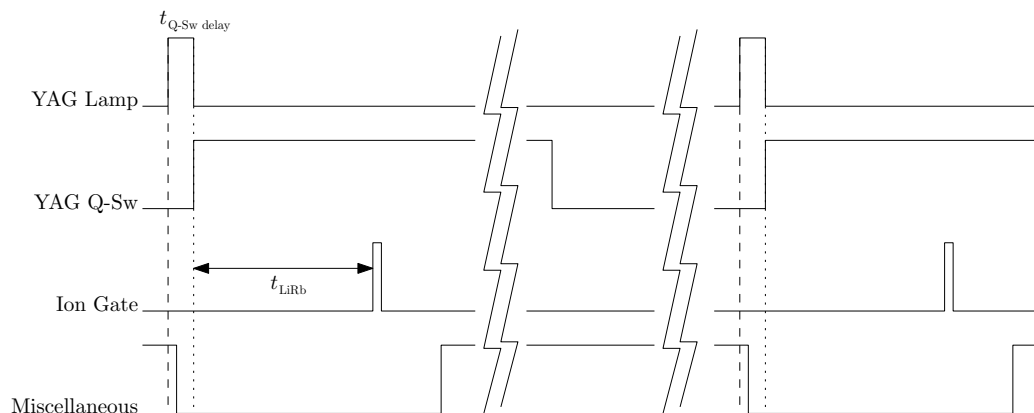


Figure 3.16. The experimental timing signals. The sequence begins with the YAG Lamp (dotted line), a 10 Hz signal that is continuously generated. Its pulse width is set so that the YAG Q-Switch triggers on its falling edge. The falling edge of the Lamp/rising edge of the Q-Switch is what we use as $t = 0$ for TOF (dotted line). The Ion Gate is a 10 Hz signal that triggers off the Q-Switch rising edge, but delayed so that it coincides with the arrival of LiRb^+ at the MCPs. The Q-Switch signal is controlled by 1 bit of an 8 bit digital wave. The other 7 bits can be configured to control other miscellaneous aspects of experimental timing. An example that could correspond to turning off field plates, magnet coils, MOT beams, etc., while ionization is occurring is shown. We have used it to control a PA beam shutter.

corresponds to an approximately 2 GHz change in laser frequency. An analog output from the PXI-6723 or some other function generator can be used to control the PA laser frequency. The analog output card is the easiest way synchronize PA scan steps with the experimental timing. The control program can change the PA frequency after an ion counting sequence, whereas more complicated methods of synchronizing the PA scan would be required if a different external control for the Ti:Sapphire was used. The control signal for the analog output card goes through a large low pass filter to reduce the laser noise as much as possible and also to ensure that any sudden large changes in the control voltage do not cause the Ti:Sapphire to come unlocked from the reference cavity. Scans generally consist of small steps ($< .05 \text{ V}$) between data points that are unlikely to cause the laser to come unlocked. A program was written

so that large changes in control voltages are applied via a ramp so that large changes can be done seamlessly to when tuning the Ti:Sapphire to a desired frequency.

Scanning the ionizing PDL is accomplished by sending pulses to the step motor driver. The controller was put together by Rekishu Yamazaki based on the SD200's manual and requires a power supply for the TTL logic and a second for the motor. Two TTL signals are sent to the controller. One controls the direction the motor turns and the second controls when the motor steps. The direction control can be left high or low for the duration of a scan depending on whether one wants to scan up or down in laser frequency. The motor steps once when a rising edge is sent to the controller's PULSE input. To scan the PDL, once ion counting is finished for one data point, the dye laser is stepped a number of times determined by the user. Because of the broad linewidth of the PDL and the power broadening that occurs for most resonances, 5 steps were generally taken between data points ($\approx 0.35 \text{ cm}^{-1}$). When it is possible that interesting structure could be made apparent with a finer scan, the number of steps should be reduced to 2 or 1, where the frequency change between steps is now comparable to the linewidth of the laser. Whether the PDL or Ti:Sapphire laser is being scanned, the control program waits to start sending the ion counting sequence again until after the laser frequency has been changed, thus ensuring that each data point in a scan has been integrated over an identical number of shots. It also makes the timing of the stepping motor pulses somewhat arbitrary. In our case, we use a software timed (less accurate than hardware timing) pulse that is high for 5 ms and low for 5 ms. The software timing allows us to use one of the DAQ card's non-hardware timed digital outputs that can only be sent a single value at a time.

Calibrating the scans is done by recording the initial and final frequencies and assuming a linear scan. The PDL stays remarkably linear over a long range and the Ti:Sapphire stays reasonably linear over a scan of 10 GHz or so. When the Ti:Sapphire is continuously scanned via a ramp signal, the scan does not quite stay linear when the ramp changes direction. For stepped scans (the kind used for ionization spectroscopy)

monitoring a wavemeter or beat signal between the laser and the frequency comb could be used to give an the laser frequency at each step, but such a measurement is not so easy to integrate and the assumption of linearity often suffices.

3.5.3 Accuracy of Ion Counting

We briefly mention the limitations in our electronics in counting individual ions as they are detected by the MCPs. There are three possible reasons why an ion that reaches the MCPs may be missed by our counting electronics. The first reason is simply that signal generated is simply not strong enough to trigger a pulse from the discriminator. To avoid this the discriminator threshold should be as close to noise level as possible. Weak signal can also easily be checked by increasing the potential difference in the MCPs to increase the gain and to see if that affects the number of ions detected.

The next two reasons that an ion may be missed both have to do with the rate at which ions are arriving. The arrival time of individual LiRb ions has roughly a Gaussian spread around t_{LiRb} . Even though, in general, we are counting fewer than two arriving ions per pulse on average, there tends to be bunching that makes it more likely to observe multiple ions or no ions for a given pulse, rather than the same number detected for each pulse. Testing demonstrates the ability to correctly count up to three LiRb ions within the arrival window, but a tendency to undercount for higher numbers, which can often happen for stronger transitions. When the time between arriving ions becomes too small, two ions that arrive nearly simultaneously create only a single count from the discriminator. Because of the limitations of the DAQ counter, we must keep the discriminator pulse width greater than 10 ns. Usually we set the width to between 15 and 20 ns. Thus, should two ions arrive within 20 ns of each other, the discriminator only generates a single pulse. Also, because the counter has a 100 MHz timebase, it can sample the discriminator output every 10 ns, which is why the pulse width must be longer than that to ensure a rising edge is

detected. Based on Nyquist theorem, the highest frequency signal the counter could theoretically detect would be 50 MHz. Using a function generator to output a TTL pulse train, it was observed that the actual limit was about half that. Undercounting of pulses started to occur when the pulse train had a frequency between 20 and 30 MHz. The speed of the DAQ counter has been the most significant cause of undercounting.

More detailed analysis of the counting statistics could be used to compensate for the undercounting and give more accurate measurements of observed peak intensities in our spectra, but a comparison between the automated electronic counting and a manual count of discriminator pulses from recorded oscilloscope traces given in table 3.2 shows that the undercounting does not significantly alter the data so that adding a correction gives little additional qualitative information.

Table 3.2

A comparison of the number of ions detected over 50 laser pulses for LiRb resonances of different strengths. DAQ refers to the number of counts recorded by the data acquisition card's counter. Software is the number of pulses counted when the discriminator output was recorded by an oscilloscope and analyzed in MATLAB to determine how many rising edges there were. The two columns represent the number of ion counts recorded by each method for the same measurement.

PDL Energy (cm^{-1})	Software	DAQ
17826	138	105
17790	77	61
17811	57	49
17716	41	30
17783	9	9

3.6 Conclusion and Future Upgrades

The experimental apparatus for creation and detection of ultracold LiRb molecules is quite robust and has some features that, while not yet used, can benefit future experiments. We have used the timing capabilities to control a shutter for the PA beam a means of determining whether the ground state LiRb molecules are in a triplet state or singlet state [34,55]. The capability exists to have timing control well beyond our current uses. We are able detect LiRb production via both fluorescence trap loss measurements and TOF ion detection. The LiRb signal is temporally well resolved. The anode that detects the current generated by the MCPs is the metal coated bottom of a phosphor screen. In the future the phosphor screen could be used to spatially resolve the detected ions, hopefully allowing us to directly image the rotational wavefunction of the molecules.

Improvements to the apparatus would likely focus on improving the efficiency of ion detection. Currently permanent magnets are being used to adjust the trajectory of the ions so that they are incident on the MCPs. The optimal magnetic field likely depends on the electric field created by the field plates. Increasing the field plate voltages did increase the ion signal, but currently we are constrained by the high voltage supplies being used. Replacing the permanent magnets used to steer the ions with magnet coils should allow for continuous control of the ion trajectory.

Finally, when a suitable pathway is found to absolute ground state LiRb, experiments will likely require that the molecules remain trapped for long times. The easiest way to trap the molecules would be to use a dipole trap created by a high power far off resonance beam. Experiments investigating the dipole-dipole interactions may require an optical lattice, where a counterpropagating beam creates a standing wave within the dipole trap. Theoretical work has been done to determine appropriate conditions where one atom of each species could present at each site within a lattice, essentially preforming the molecules in a state ready for PA to create a molecule at each lattice site [14]. Polar molecules can also be trapped within a specially designed

electrostatic field [104]. While the cost of such a trap would be cheaper, it would likely add to the experimental complexity within an already crowded vacuum system.

4. Previous Theoretical and Experimental Results in LiRb

In this chapter we discuss previous theoretical and experimental results in LiRb that will inform our new experimental data. LiRb has lagged behind studies of other bialkali molecules, there have been theoretical predictions for LiRb molecular potential energy curves (PECs) [105, 106] and long range interactions based on the C_6 coefficient for various potentials [20, 107, 108]. Also of importance is theoretical work done on LiRb^+ because of our reliance on ionization spectroscopy. PECs that are derived from experimental results are much more accurate than these *ab initio* calculations. Spectra taken in heat pipes, where very hot LiRb can be formed through three body collisions, have mapped out a few potentials [39, 40].

Our more recent results from cold molecule spectroscopy include discovering and measuring the binding energy of weakly bound levels in excited LiRb^* by finding photoassociation (PA) resonances. The excited levels can be detected either by trap loss (a drop in MOT fluorescence due to population decrease via molecular formation) or, in regions where the fluorescence contrast is too weak to determine trap loss, ion detection can be used by tuning the ionizing pulsed dye laser (PDL) to a frequency where the molecule can undergo resonantly enhanced multiphoton ionization (REMPI). Our group has detected numerous LiRb resonances via both methods [12, 13, 55, 83]. When the frequency of a PA laser is fixed on a resonance. The PDL can be scanned to find REMPI resonances. The energies where REMPI resonances occur depend on the excited molecular states enhancing the ionization and the initial ground states populated. By looking for progressions in the REMPI spectra, assignments can be made for the initial state and the intermediate state that enhances the ionization process.

4.1 Correspondence between Hund’s case (a) or (b) and Hund’s case (c)

Quantum descriptions of diatomic molecules are covered in detail in Appendix A. Here we simply note that when discussing molecular potentials, it is important to know how strongly the electronic orbital angular momentum and spin couple to the internuclear axis, which largely depends on the internuclear separation. At large internuclear spacing, LiRb falls under Hund’s coupling case (c), where Ω , the projection of total electronic angular momentum on the internuclear axis, is a good quantum number. Closer internuclear spacings fall under Hund’s coupling case (a), or in the case of triplet Σ states, Hund’s case (b). In Hund’s case (a) Λ and Σ , the projections of orbital angular momentum and spin respectively, are also good quantum numbers. In Hund’s case (b), Σ is not a good quantum number. Thus in Hund’s case (a) or (b), the PEC is described by Λ and the multiplicity of the state based on the spin, $2S + 1$. The selection rules for the Hund’s cases are covered in the appendix. PECs attempt to describe atomic interactions at all internuclear separations, thus there must be a correspondence between Hund’s case (a) or (b) potentials and Hund’s case (c) potentials. Correlation between Hund’s case (a) or (b) and (c) is covered by in reference [31]. The Hund’s case (a) or (b) to Hund’s case (c) correlation for LiRb for the first 6 PECs can be found in table 4.1.

There are a couple of notational issues to note when discussing vibrational levels close to a potential’s dissociation energy. First, the vibrational quantum number v starts at $v = 0$ for the lowest vibrational level in a PEC. Levels close to the bottom of a PEC almost always belong to Hund’s case (a) or (b). As v increases, it is common to describe high v levels in terms of a PEC labeled Hund’s case (a) or (b) notation, *e.g.* $v' = 34$ of the $B^1\Pi$ state. However, spin and the orbital angular momentum are not good quantum numbers for these high v states because their large internuclear separation causes them to fall under Hund’s case (c). $v' = 34$ of the $B^1\Pi$ state actually better described as belonging to the $4(1)$ potential, which can be thought of as an admixture of singlet and triplet states. Notationally, $B^1\Pi$ and $4(1)$ are describing

Table 4.1
Correspondence between labelling of PECs in Hund's case (a) or (b) potentials to Hund's case (c) potentials.

Hund's case (a) or (b)	Hund's case (c)
Li(2S)+Rb(5S)	
$X^1\Sigma^+$	1(0 ⁺)
$a^3\Sigma^+$	1(0 ⁻)
	1(1)
Li(2S)+Rb(5P)	
$A^1\Sigma^+$	2(0 ⁺)
$c^3\Sigma^+$	2(0 ⁻)
	2(1)
$b^3\Pi$	3(0 ⁺)
	3(0 ⁻)
	3(1)
	1(2)
$B^1\Pi$	4(1)

the same PEC, but in regions where a molecule has different good quantum numbers and therefore different selection rules. The other issue is how to label levels close to the asymptote observed via PA when the number of vibrational levels in a PEC is unknown. The notation used in this thesis is to label these states starting with $v = 1$ for the least bound vibrational level and using the appropriate Hund's case (c) notation to describe the potential. For example $v = 3$ of the 4(1) potential is the third least bound state. Using Hund's case (c) notation indicates that we are dealing with weakly bound molecules and labelling v in terms of increasing binding energy is consistent with the description weakly bound states presented by LeRoy and Bernstein [109]. This notation for weakly bound states is not universal, and would

likely be dropped if there was no possible ambiguity in the number of vibrational levels.

Our group has previously measured the binding energy of many levels of the Hund's case (c) potentials listed in table 4.1. In the Hund's case (c) regime, the molecular properties are largely determined by the C_6 van der Waals dispersion coefficient. Heteronuclear atomic interactions at long range takes the form:

$$V(R) = -\frac{C_6}{R^6} - \frac{C_8}{R^8} - \frac{C_{10}}{R^{10}} - \dots \quad (4.1)$$

Knowledge of the C_6 coefficient is enough information to accurately calculate energies of vibrational levels close to the dissociation limit using the LeRoy-Bernstein formula:

$$D - E_v = A_6(v - v_D)^3 \quad (4.2)$$

where D is the dissociation energy, E_v is the energy of vibrational level v , v_D ($0 < v_D < 1$) is the vibrational quantum number at dissociation, and

$$A_6 = \frac{16\sqrt{2}\pi^3\hbar^3}{B(2/3, 1, 2)^3\mu^{3/2}C_6^{1/2}}$$

with μ being reduced mass of LiRb and B being the Beta function [109]. The C_6 coefficients of some potentials are very similar but other information can be used to assign lines to a particular potential (such as hyperfine structure). All of the potentials asymptotic to the Rb D₁ line (2(0⁺), 2(0⁻), and 2(1)) have similar C_6 coefficients Potentials asymptotic to the Rb D₂ line fall into two groups with similar C_6 values: the first group is made up of 3(0⁺), 3(0⁻) and 3(1), and 1(2) and 4(1) form the other group [20, 107, 108]. Figure 4.1 shows the long range interactions for states just below either the D₁ or D₂ line.

4.2 LiRb PECs: Theoretically and Experimentally Determined

Figure 4.2 shows PECs for LiRb. Some of the curves are based on *ab initio* calculations done by Korek [106]. In the figure, these are shown with dashed lines. The PECs calculated by Korek are adiabatic calculations that incorporate spin-orbit

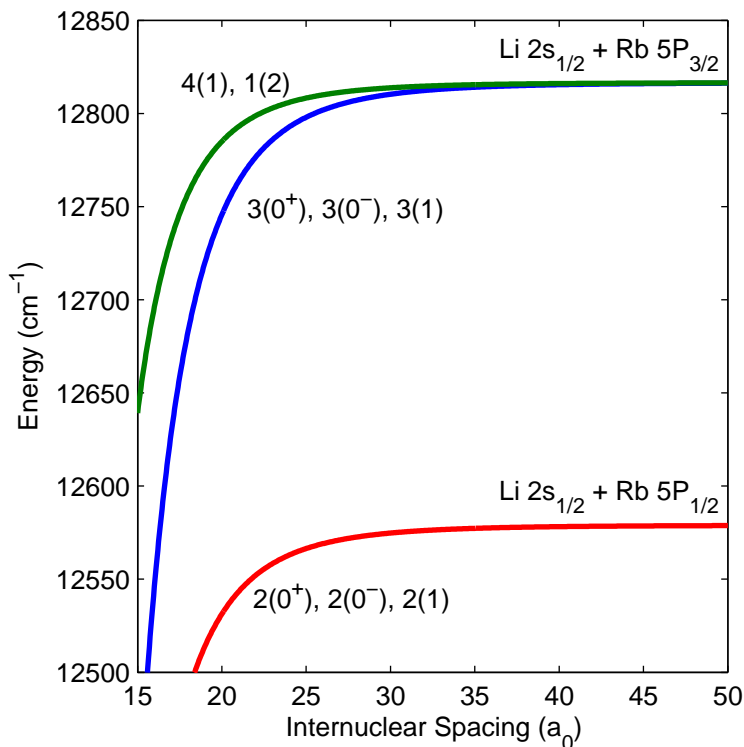


Figure 4.1. Calculations of long range interaction for LiRb molecules [107]. At long range the molecules are fall under Hund's case (c), thus the potentials are labeled using the good quantum number Ω , the total electronic angular momentum projection.

interaction. Potentials that have the same total electronic angular momentum projection, Ω , have avoided crossing in adiabatic calculations as crossings are not allowed in the Born-Oppenheimer approximation [5]. However, the correct way to calculate vibrational states from a PEC is to use a diabatic potential if the nuclear motion is fast enough that it cannot be decoupled from electronic motion [55, 110, 111]. For example, the $b^3\Pi$ crosses the $A^1\Sigma^+$ at around $8a_0$. For the $b^3\Pi_{0^+}$ potential, the adiabatic calculation would represent an avoided crossing between the $(2)\Omega = 0^+$ and $(3)\Omega = 0^+$ potentials, where (2) and (3) refer to second and third most deeply bound $\Omega = 0^+$ potentials following the notation used by Korek. To create the diabatic curve, $(2)\Omega = 0^+$ before the avoided crossing would be joined with $(3)\Omega = 0^+$ after

the avoided crossing to create the diabatic $b^3\Pi_{0^+}$ potential. Likewise the $(3)\Omega = 0^+$ would be joined with the $(2)\Omega = 0^+$ to create the diabatic $A^1\Sigma^+$. If the avoided crossing in the adiabatic calculation is large (which would deform the diabatic calculation), data points can be removed so that software used to calculate molecular constants, such as LEVEL, can fill in a smoother interpolation.

Some PECs are well known over a large region because transitions have been measured and assigned in heat pipe experiments [38–40]. These PECs can be calculated to fit experimental results. PECs obtained from experimental observations are represented in figure 4.2 with solid lines. Table 4.2 shows which potentials have had vibrational levels observed experimentally in heat pipe experiments. While transitions to the $C^1\Sigma^+$ have not been reported, perturbations on $B^1\Pi$ levels from at least eight $C^1\Sigma^+$ levels have been used to roughly calculate a PEC for $C^1\Sigma^+$ [40]. This is not an exhaustive list of all molecular states observed. Our REMPI spectroscopy has identified the $v = 7$ –13 states of the $a^3\Sigma^+$ potential [55], but these results have not been incorporated into any new calculations of that potential. Information on the long range interaction has been gathered through PA, but joining the C_6 information obtained, to more deeply bound levels has not yet occurred and may require observations of additional vibrational levels to accurately join the two regions.

Table 4.2
Vibrational Levels previously observed in heat pipe experiments.

PEC	Observed Vibrational Levels	Ref
$X^1\Sigma^+$	0–45	[39]
$a^3\Sigma^+$	5,6	[39]
$B^1\Pi$	0–22	[38, 40]
$D^1\Pi$	0–10,13,15	[39]

Because $S = 1/2$ for both Li and Rb, LiRb comes in either triplet $S = 1$ or singlet $S = 0$ states. For triplet state, the spin-orbit interaction results in a splitting

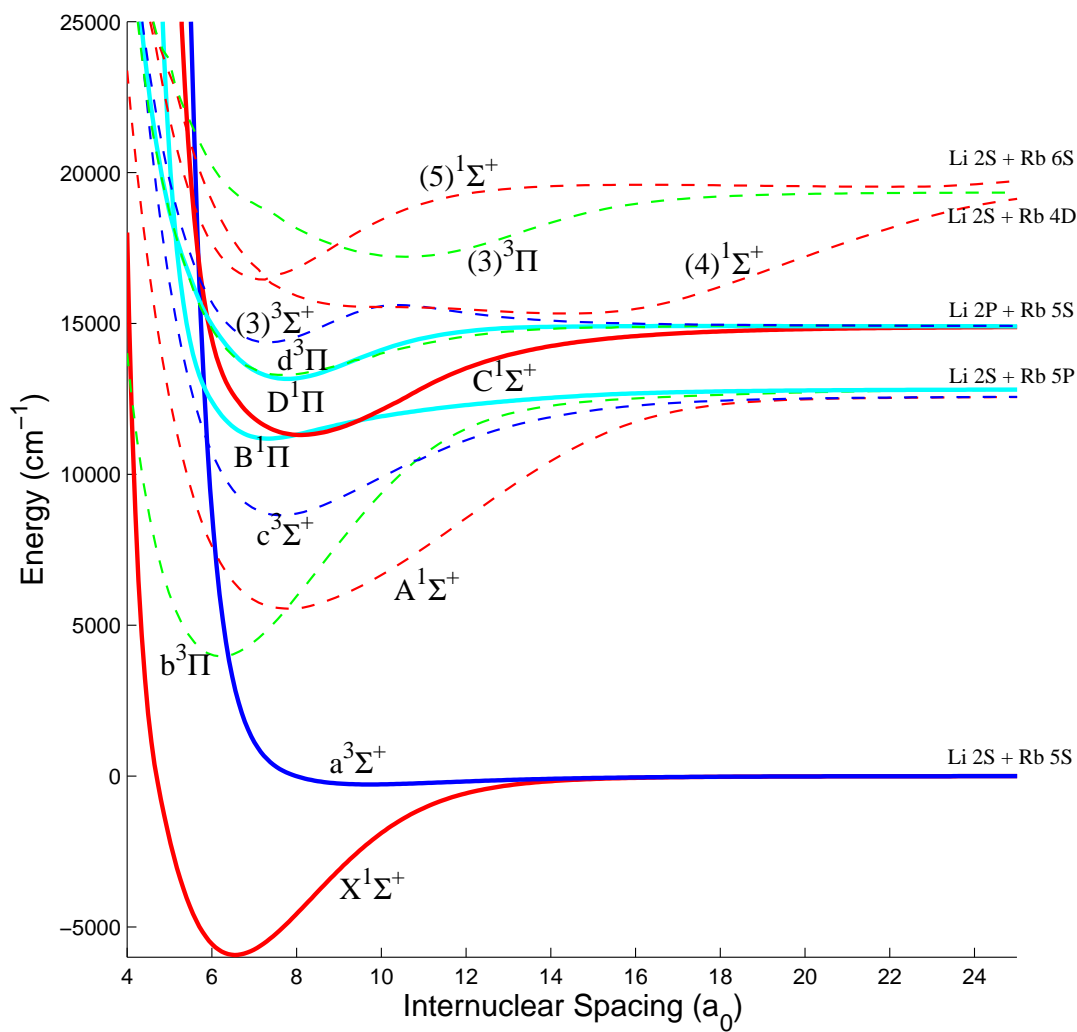


Figure 4.2. Diabatic potential energy curves for LiRb. All curves asymptotic to the lowest three atomic energy states (ignoring fine structure) are shown. Solid curves are calculations based on experimental observations from Ivanova *et al.* [39, 40]. The dashed curves are based on adiabatic calculations from Korek [106], which have had avoided crossing removed to make them diabatic curves. The top three curves are asymptotic to either the Li 2S + Rb 4D or Li 2S + Rb 6S states. Many other PECs are asymptotic to Li 2S + Rb 4D, but are not pictured.

analogous to the spin-orbit contribution to the fine structure in atomic systems. Thus, in Hund's case (a), the electronic energy for states of different spin projections, Σ , would be given, to first order, by

$$T_e = T_0 + A\Lambda\Sigma \quad (4.3)$$

where T_0 is the electronic energy where spin is ignored and A is a constant for different $\Lambda + \Sigma$ multiplet terms [112]. Because of this triplet potentials where $\Lambda \neq 0$ (such as Π and Δ potentials) have a spin-orbit splitting that gives rise to multiplet potentials. It should be noted $\Lambda + \Sigma$ is distinguished from $\Omega = |\Lambda + \Sigma|$ because in molecules with larger spins, it is possible for $\Lambda + \Sigma$ to be negative which would have a different splitting from a positive $\Lambda + \Sigma$ of the same magnitude. $b^3\Pi$ should split into $b^3\Pi_2$, $b^3\Pi_1$, $b^3\Pi_{0-}$, and $b^3\Pi_{0+}$. For $\Omega = 0$ states there is an additional small splitting for states of different parity upon reflection in any plane containing the internuclear axis. The spin-orbit interaction results in a multiplet peak structure of observed vibrational levels for Hund's case (b) to Hund's case (a) transitions or vice versa. This has been observed in the $(3)^3\Pi$ potential [55]. At long range, each branch of the splitting will correspond to a different Hund's case (c) potential, but during this change over, Λ and Σ are no longer a good quantum numbers and separation into different potentials can no longer be treated as spin-orbit correction. In fact, the different spin-orbit branches at close range need not correspond to potentials with similar C_6 coefficients at long range. For example, the $1(2)$ has a very different C_6 from the other Hund's case (c) potentials that correlate to the $b^3\Pi$ potential. Instead it has a C_6 similar to the $4(1)$ which correlates to the $B^1\Pi$.

4.3 Previous Photoassociation Results

In PA, it is assumed that the energy of the ultracold colliding atoms is approximately at the dissociation limit of ground state molecules. In LiRb this corresponds to the the $2S_{1/2}$ and $5S_{1/2}$ states in Li and Rb respectively. As the PA laser is tuned to the red of an atomic resonance, it can be tuned through a molecular rovibrational

level. Since atomic resonances correspond to the dissociation limit of excited electronic potentials, the difference in frequency between the atomic resonance and the detected PA resonance, Δ_{PA} , gives a very accurate measurement of the binding energy of the excited LiRb^* molecule. Observations of these levels, either through trap loss [12, 13, 83] or [55] ionization spectroscopy can be fitted to the LeRoy-Bernstein formula (equation (4.2)) to give a C_6 coefficient and v_D , giving an accurate picture of the long range interactions of the atoms.

Our previous work has detected for several of the potentials shown in figure 4.1. Table 4.3 is a summary of the potentials that we have mapped out in previous PA experiments, along with the most bound vibrational level detected and its binding energy, the measured C_6 coefficient of the potential.

Table 4.3

A summary of previous PA spectroscopy results. Molecules formed in the $3(0^+)$ have only been detected via trap loss. Despite being having the strongest observed PA rate in trap loss, no ions are detected, likely indicating the molecule dissociates before decaying to an electronic ground state. The C_6 coefficient is reported in atomic units.

Potential	Lowest v	Δ_{PA} (GHz)	C_6 (ion) [55]	C_6 (trap loss) [12, 13]
2(0^+)	5	-208.08	10120 (450)	11335(+600, 300)
2(0^-)	11	-1862.02	12410 (180)	13470 (+540, 270)
2(1)	10	-1345.77	13130 (330)	13730 (+535, 270)
3(0^+)	5	-106.75	-	20160 (950)
4(1)	5	-217.81	8750 (500)	9235 (490)
1(2)	6	-373.06	10070 (590)	10190 (420)

4.4 Previous REMPI Results from PA to the 2(0^-) Potential

While using PA to measure the binding energy of excited states can be done using either trap loss or ion detection, the levels of the ground state potential the

molecule decays to after PA can only be detected by scanning the REMPI laser. These spectra are in terms of ion production versus REMPI frequency while the PA laser is fixed on a resonance. Peaks occur when the REMPI laser is resonant with an excited state that enhances the ionization of the molecule. We can then detect LiRb^+ with our mass spectrometer. Thus, these spectra contain information about both the vibrational levels populated as molecules created by PA decay down to the ground state as well as the vibrational levels of the intermediate potential used to enhance ionization. Interpreting REMPI spectra can be similarly difficult to interpreting heat pipe spectra because the vibrational spacings from the two participating potentials have to be disentangled to make assignments. REMPI spectra do have the advantage of originating from cold molecules, so that only low J states contribute to observed transitions. Heat pipe spectra can involve rotational quantum numbers as high as $J > 100$ meaning the rotational structure of different vibrational states starts to overlap.

Previous work relied on forming molecules via PA to the $v = 5, 9, 11$ of the $2(0^-)$ potential. The complete spectra and assignments can be found in Adeel Altaf's thesis [55]. A section of the data from REMPI spectra taken while the PA laser is resonant with the $v'' = 5$ level is shown in figure 4.3. The notation v'' and v' are used to distinguish between ground state (v'') and excited state (v') vibrational levels in a molecular transition. Piecing these spectra together has identified the $v'' = 7-13$ levels of the $a^3\Sigma^+$ state and the $v' = 0-10$ lines of the $(3)^3\Pi$ state. After PA, the molecule can decay from the $2(0^-)$ potential to either the $1(0^-)$ or the $1(1)$ potential. Either long range potential corresponds to the $a^3\Sigma^+$ at close range. The intermediate states that enhance the REMPI process are vibrational levels of the $(3)^3\Pi$ state. Because this is a Hund's case (b) to Hund's case (a) transition, there are no selection rules governing Σ and Ω quantum numbers. Because of this figure 4.3 clearly shows triplet peaks due to splitting from the spin-orbit splitting of $(3)^3\Pi$ states.

Of note is that no lines of significance were seen below 17300 cm^{-1} because the $a^3\Sigma^+$ states are being ionized through the very bottom of the $(3)^3\Pi$ state. Below

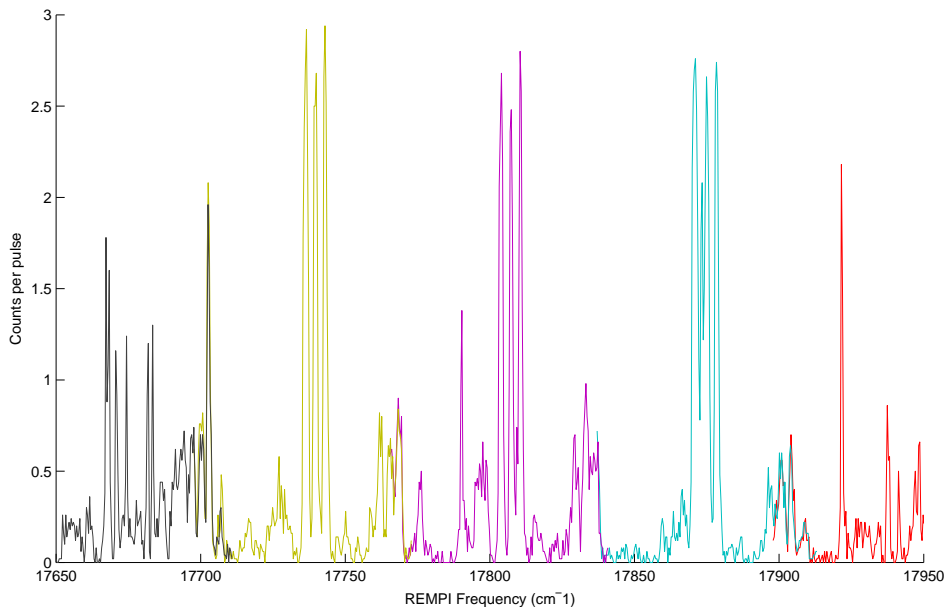


Figure 4.3. A section of REMPI spectra when the PA laser is kept fixed on the $v'' = 5$ level of the $2(0^-)$ potential. The colors represent different individual scans that have been pieced together. The $2(0^-)$ decays to the $1(0^+)$ or $1(1)$ potential, both of which correlate to the $a^3\Sigma^+$ potential at close range. Of note are the triplet peaks that occur due to the spin-orbit interaction in the $(3)^3\Pi$ potential. Details and assignments for these lines can be found in reference [55].

the $v' = 0$ there would be no other triplet potential through which to ionize until reaching states that are asymptotic to the $\text{Li } 2\text{P} + \text{Rb } 5\text{S}$ state at 14904 cm^{-1} , which would not have enough energy to ionize via a two photon process without a two color REMPI process.

Also of note is the somewhat regular spacing of the triplet peaks. When attempting to find a pattern in REMPI spectra, one tool that can be used is to take the autocorrelation function of the spectra. If there is a somewhat regular vibrational level spacing, ΔG_v this will result in a peak in the autocorrelation function at that energy separation. The bottom of most potentials can be approximated as harmonic oscillators close to the equilibrium internuclear spacing, R_{eq} . This is indeed the case

for the $(3)^3\Pi$. The autocorrelation functions of the REMPI spectra taken for PA to the $v' = 5$ and $v' = 11$ states are shown in figure 4.4. The autocorrelations both exhibit strong peaks at about 70 cm^{-1} , the approximate vibrational spacing near the bottom of the $(3)^3\Pi$ potential. Upon finding this pattern, one can look for a repeating pattern among peaks with smaller separation to identify the vibrational levels of the $a^3\Sigma^+$ which is a very shallow potential. Anharmonic corrections vary from potential to potential, making the regularity of ΔG_v , and the usefulness of autocorrelation functions hard to predict.

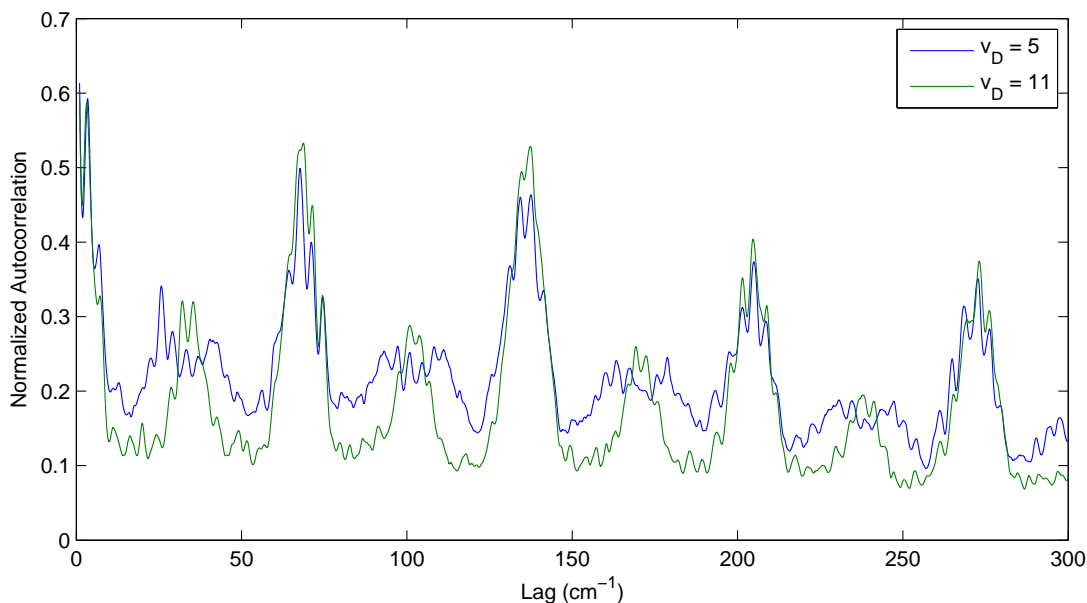


Figure 4.4. Autocorrelation functions for REMPI spectra. LiRb molecules are produced via PA to the $v'' = 5$ and $v'' = 11$ levels of the $2(0^-)$ potential and undergo resonantly enhanced ionization through the $3(3)^3\Pi$ state. The distinct peak at around 70 cm^{-1} is due to the vibrational level spacing of deeply bound molecules in the $(3)^3\Pi$ state.

4.5 Calculations of LiRb⁺ Potential

Production of LiRb⁺ via REMPI depends on the two photons having enough energy to reach a bound LiRb⁺ state. The asymptotic energy of Li 2S + Rb⁺ lies a minimum of 33,690.81 cm⁻¹ above the Li 2S + Rb 5S ground state asymptote [113]. LiRb⁺ has its own molecular potential and the depth of that potential determines the energy required to ionize LiRb. If the molecule is in a vibrational state v'' at energy $E_{v''}$, there are two conditions that must be satisfied for REMPI. The first is the resonance condition

$$\hbar\omega = E_{v'} - E_{v''} \quad (4.4)$$

where $\hbar\omega$ is the energy of the REMPI photon and $E_{v'}$ energy of a vibrational level in the excited state. The strength of the transition relies on the Franck-Condon factor (FCF) of the $v'' \rightarrow v'$ transition and not every transition will have a large enough FCF to be observed.

The second condition is one of having sufficient two photon energy for ionization:

$$2\hbar\omega \geq E_{v_+=0,min} - E_{v''}. \quad (4.5)$$

Here, $E_{v_+=0,min}$ is the minimum energy of the ion's lowest vibrational state, $v_+ = 0$. The dissociation energy of LiRb⁺ is a continuum above 33,690.81 cm⁻¹ because the kinetic energy of the ejected electron can carry away the excess energy. Thus positions of energy levels in the ion relative to the ground state molecule depend on the kinetic energy of the free electron. $E_{v_+=0,min}$ refers to energy of the ion's lowest vibration level in the limit that the free electron has zero energy. FCFs play a much smaller role for the ionization transition because the LiRb⁺ is a continuum state. For a two photon transition where $2\hbar\omega = E_{v_+} - E_{v''}$, several v_+ states can result in the same energy by adjusting the dissociation energy of the ion accordingly. If $2\hbar\omega$ is of sufficient energy, the molecule, in essence, "chooses" the best v_+ states to ionize through. When $2\hbar\omega$ is closer to the ionization threshold, FCFs have a larger influence. For example, if $v_+ = 0$ is the only accessible level of the ion because of insufficient energy to access higher states then whether or not ionization occurs should depend

on the FCF. However, extracting even qualitative information about FCFs involving ionized states from spectra would be quite difficult.

As there are no experimental observations for LiRb^+ binding energies, we must rely on theoretical calculations to inform our expectations of allowed REMPI transitions. Previous REMPI experiments in LiCs have demonstrated qualitative validity of some previous calculations [8]. Based on condition 4.5, their experiments demonstrated a lower bound for the potential depth of the $X^2\Sigma^+$ state of LiCs^+ was at least 3385 cm^{-1} . This is consistent with some calculations of D_e , the potential depth at R_e , the equilibrium internuclear spacing. Other theoretical calculations placed $D_e < 3000 \text{ cm}^{-1}$. Of the theoretical works that were not discounted by the LiCs measurement, two also have predictions for D_e of $\text{LiRb}^+ X^2\Sigma^+$ potential. The results of their calculations for D_e , R_e , and ω_e are shown in table 4.4.

Table 4.4

Calculated values for D_e the potential depth, R_e the equilibrium spacing, and ω_e , the first term in the anharmonic oscillator expansion. The two references also provide calculations for LiCs^+ that were consistent with experiment.

Ref	$D_e \text{ (cm}^{-1}\text{)}$	$R_e \text{ (}a_0\text{)}$	$\omega_e \text{ (cm}^{-1}\text{)}$
[114]	4202	7.6	140
[115]	4193.54	7.54	139.65

Given that the $v_+ = 0$ state lies roughly $\frac{1}{2}\omega_e$ above the bottom of the potential, a good approximate value for $E_{v_+=0,min}$ is $E_{v_+=0,min} = IE_{\text{Rb}} - D_e + \frac{1}{2}\omega_e$, where IE_{Rb} is the Rb ionization energy of $33,690.81 \text{ cm}^{-1}$. Thus a good estimate for the binding energy of the $v_+ = 0$ state is about 4130 cm^{-1} and $E_{v_+=0,min}$ lies roughly $29,560 \text{ cm}^{-1}$ above the ground state dissociation limit. These constraints will be used to determine which transitions are possible for the range of REMPI frequencies scanned.

5. REMPI Spectra of the $X^1\Sigma^+$ State

In this chapter we examine the resonantly enhanced multiphoton ionization (REMPI) spectra of molecules that are formed via PA to the 4(1) potential. Surprisingly, we find very deeply bound states populated, as many observed transitions can be assigned to known energies for $X^1\Sigma^+ \rightarrow B^1\Pi$ or $X^1\Sigma^+ \rightarrow D^1\Pi$ transitions. We present evidence that decay after PA is taking place at close internuclear spacings that should decay to these deeply bound levels, although the physical reason for why this is happening is unknown. We hope that this information helps find a route to the rovibronic ground state of LiRb in the future.

5.1 Experimental Conditions and Resulting Spectra

We recorded REMPI spectra for three different PA resonances, the $v' = 3, 4, 5$ levels of the 4(1) potential. The 4(1) potential correlates only to the $B^1\Pi$ potential at close range. Because the $B^1\Pi$ potential has been studied by heat pipe spectroscopy for $v' \leq 22$, the parameters of the potential are fairly well known. Based on these measurements, it is expected that the $B^1\Pi$ potential has vibrational levels up to $v' = 36$ (or possibly 37). Even though levels above $v' = 22$ haven't been observed, the previous work suggests that the $v' = 3, 4, 5$ vibrational levels of the 4(1) electronic potential correspond to the $v' = 34, 33, 32$ levels of the $B^1\Pi$. Unfortunately, a connection between the low v' and high v' levels of the $B^1\Pi$ cannot be made at this time because the binding energies of the electronic potentials involved in the measurements are not precisely known. The energy of $v' \leq 22$ levels has been measured with respect to the $v'' = 0$ level of the $X^1\Sigma^+$ potential via heat pipe spectroscopy, while long range 4(1) levels have been measured relative to the dissociation energy of the 4(1)/ $B^1\Pi$ potential through PA. The binding energy of the $v = 0$ level, $D^* - E_{v'=0}$,

has an uncertainty of a few wavenumbers [40], so there is no true measurement of the separation between the 4(1) $v' = 5$ level and the B¹Π $v' = 22$ level to connect the two regions.

We measured the PA laser frequency using a wavelength meter, either a Bristol 621A Wavelength Meter or a HighFinesse WS/6-200 Wavelength Meter. Beating a portion of the PA beam against the output of a MenloSystems FC1500 frequency comb ensured the same absolute PA frequency was used for each REMPI scan to keep the PA laser stable and to ensure that a calibration drift or offset would not affect the PA rate. Table 5.1 shows the frequency of the PA laser for each of the resonances used. The beat signal, f_{beat} depends on the frequency comb parameters in equation (3.4). Because the sign f_0 depends on how the frequency comb is locked, the values of f_{beat} can differ by ± 80 MHz in practice. Thus frequency comb measurements rely on an accurate wavelength meter to determine which tooth of the frequency comb is producing the beat and the sign of f_0 . $f_{beat} = 125$ MHz is unsigned because that is when the PA frequency is exactly halfway between two teeth of the frequency comb, making the sign ambiguous. Otherwise, the sign of f_{beat} is positive if it increases as f_{laser} increases and negative if it decreases as f_{laser} increases.

Table 5.1

The absolute frequency measured via a wavelength meter, PA detuning, and the value of the beat signal used to ensure measurements were reproducible. Note that the absolute frequency can be calculated using equation (3.4) and the value measured by the wavelength meter may not exactly agree because of calibration offsets. The sign of f_{beat} is determined by observing the beat signal as the PA laser is tuned and differ by ± 80 MHz depending on the frequency comb offset.

4(1) level	Absolute ν (GHz)	Δ_{PA} (GHz)	f_{beat} (MHz)
$v' = 3, J = 2$	384191.49	-40.67	+10
$v' = 4, J = 1$	384126.66	-105.50	-80
$v' = 5, J = 1$	384014.37	-217.79	125

5.1.1 REMPI scans

Figures 5.1, 5.2, and 5.3 show the raw data for REMPI scans taken between 16400–18000 cm^{-1} for PA to the 4(1) $v' = 3, 4, 5$ levels, respectively. Figure 5.4 shows all of these scans, where the data for each scan has been normalized relative to the strongest peak, which removes the PA rate information and focuses on the relative intensities of the REMPI transitions. The PA beam has a collimated beam diameter of 0.85 mm. When on the strongest PA resonance, the 4(1) $v' = 3$, about 350 mW of power were used. When on the weaker $v' = 4, 5$ PA resonances, we increased the power to over 450 mW in an attempt to increase the PA rate and reduce the integration time required per data point. The number of shots over which the data was integrated is noted by each figure. The pulsed dye laser (PDL) typically had pulse energy of 2–4 mJ per shot and a beam diameter of 4 mm. Two different dyes were required to cover the overall scan range of 16400–17000 cm^{-1} . R610 covers roughly from 16400–17200 cm^{-1} and R590 covers from 17200–18000 cm^{-1} . Towards the edge of the dye ranges, where the gain is no longer quite as strong, the energy of the PDL pulses may drop below 1 mJ. As this starts to happen, amplified spontaneous emission (ASE) begins to accompany the laser pulse. ASE is responsible for the increase in background signal seen around 16400 cm^{-1} , 17200 cm^{-1} , and 18000 cm^{-1} .

To calibrate the REMPI scans, we measured the wavelength of the PDL using a Coherent Wavemaster wavelength meter (accuracy 0.2 cm^{-1}) at the beginning and end of each scan. The PDL tuning is very linear so we assigned intermediate data points simply by producing a linear fit. There are a couple of gaps in the scans which correspond to atomic Rb resonances. The $5P_{3/2} \rightarrow 7D_{5/2,3/2}$ occurs at 17463.57 cm^{-1} and the $5P_{3/2} \rightarrow 9S_{1/2}$ transition occurs at 17682.49 cm^{-1} [113]. Despite using a dark MOT in an effort to keep as many Rb atoms in the ground $5S_{1/2}$ state, there will always be some fraction of the population in the excited $5P_{3/2}$ state of the cycling transition. The aforementioned transitions are both electric dipole allowed transitions and will result in strong two photon ionization of the excited Rb atoms. Approaching

either of these energies on a REMPI scan results in a much stronger Rb^+ signal on the mass spectrometer. Eventually the Rb^+ signal expands temporally to the point that it overlaps with arriving LiRb^+ , meaning those data points should be ignored. If the signal gets strong enough, it starts to saturate the MCPs meaning that there is no detectable signal until after some recovery time, which will coincide with the arrival of LiRb^+ . For most scans, sections around these transitions are skipped. Data points that were taken near these transitions where it was determined that the signal was due to Rb^+ and not LiRb^+ were deleted so as to not interfere with the assignment of LiRb^+ lines. The $5\text{P}_{3/2} \rightarrow 7\text{D}_{5/2,3/2}$ was much stronger and a wider section of the scans were unusable around that line.

5.1.2 $v'' = 5$ Spectra and Choice of J

We took REMPI spectra over nearly the entire range of both the R590 and R610 dyes for PA to the $v' = 3$ and $v' = 4$ levels of the $4(1)$ state. Only a small section was taken for PA to the $v' = 5$ level. The reduction in PA rate required a longer integration time to achieve an acceptable number of counts for signal to noise. Also, after overlaying the spectra in figure 5.4 it became apparent that spectra were nearly identical. The $v = 3, 4, 5$ have nearly all the same lines with perhaps a few weaker lines that appear in only in one or two of the scans. Also, the rotational levels used differs between $v' = 3$ ($J = 2$) and $v'' = 4, 5$ ($J = 1$). There are actually some interesting differences which seem to depend on which J was used for PA. Initially, J was chosen simply because it seemed as if either $J = 1$ or $J = 2$ resulted in a stronger ion signal for different v' states. However, subsequent PA scans show this may not have been the case. It is possible that significant differences in ion counting signal for vibrational states with different J values could have been due to the fact that the frequency of the PA laser had simply not been optimized.

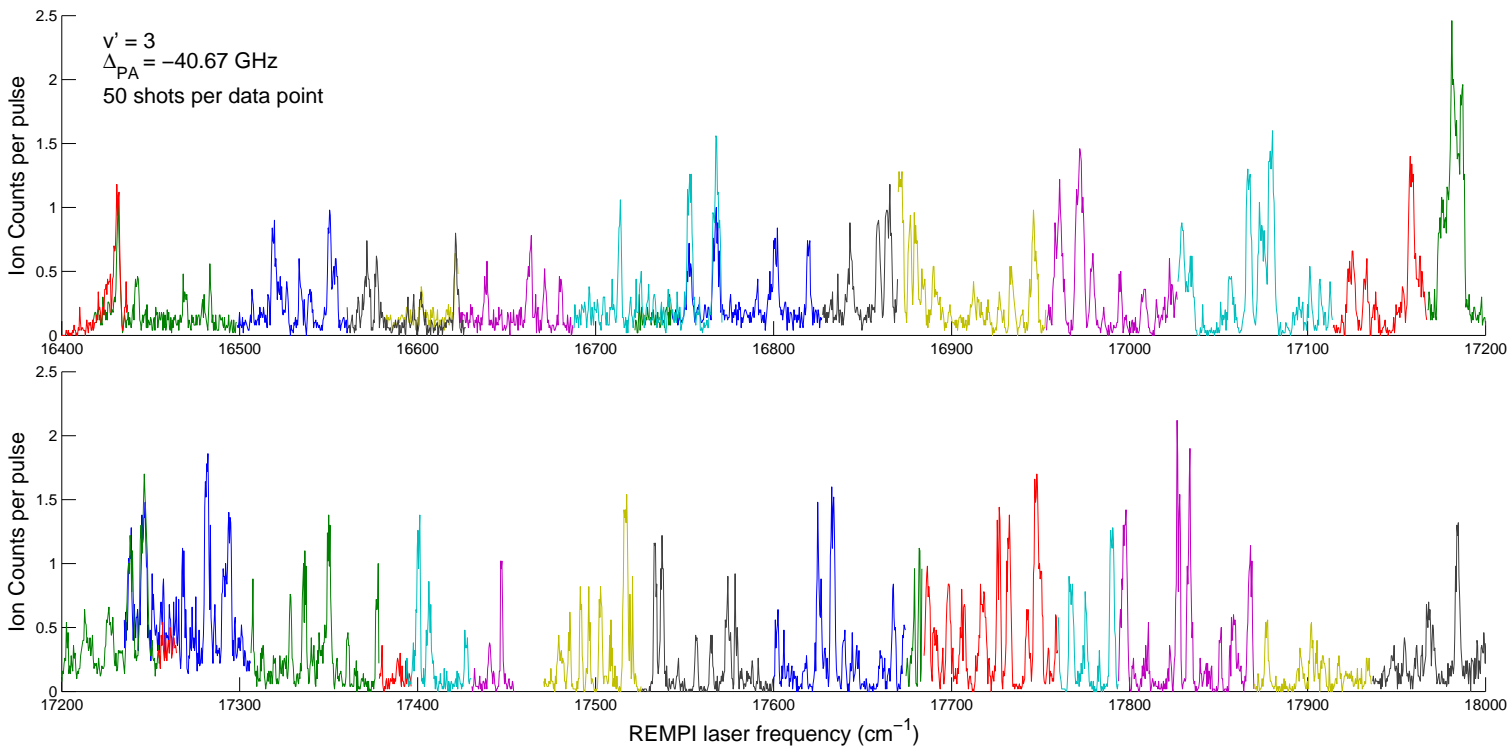


Figure 5.1. Raw REMPI scans taken while the PA laser is resonant with the $v' = 3$, $J = 2$ level of the $4(1)$ potential.

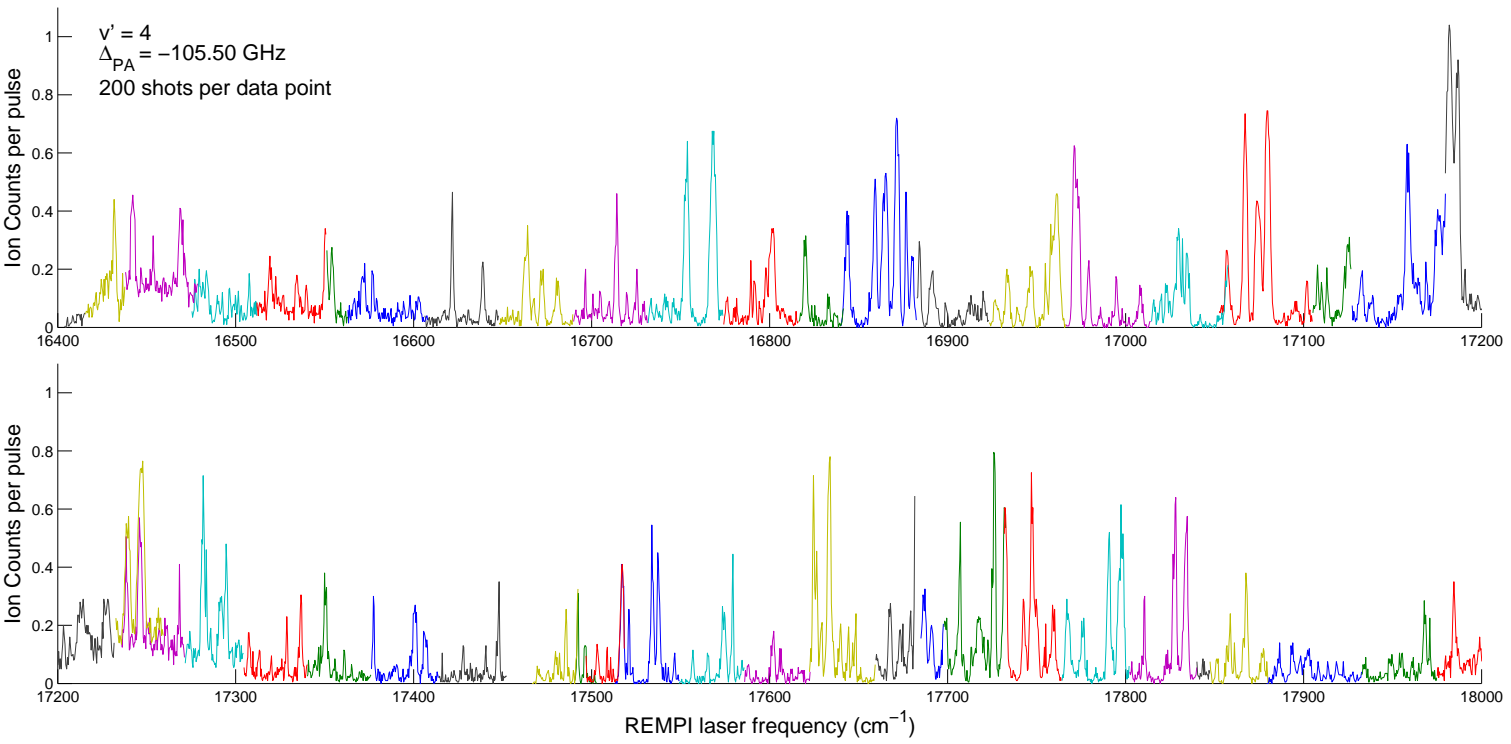


Figure 5.2. Raw REMPI scans taken while the PA laser is resonant with the $v' = 4$, $J = 1$ level of the $4(1)$ potential.

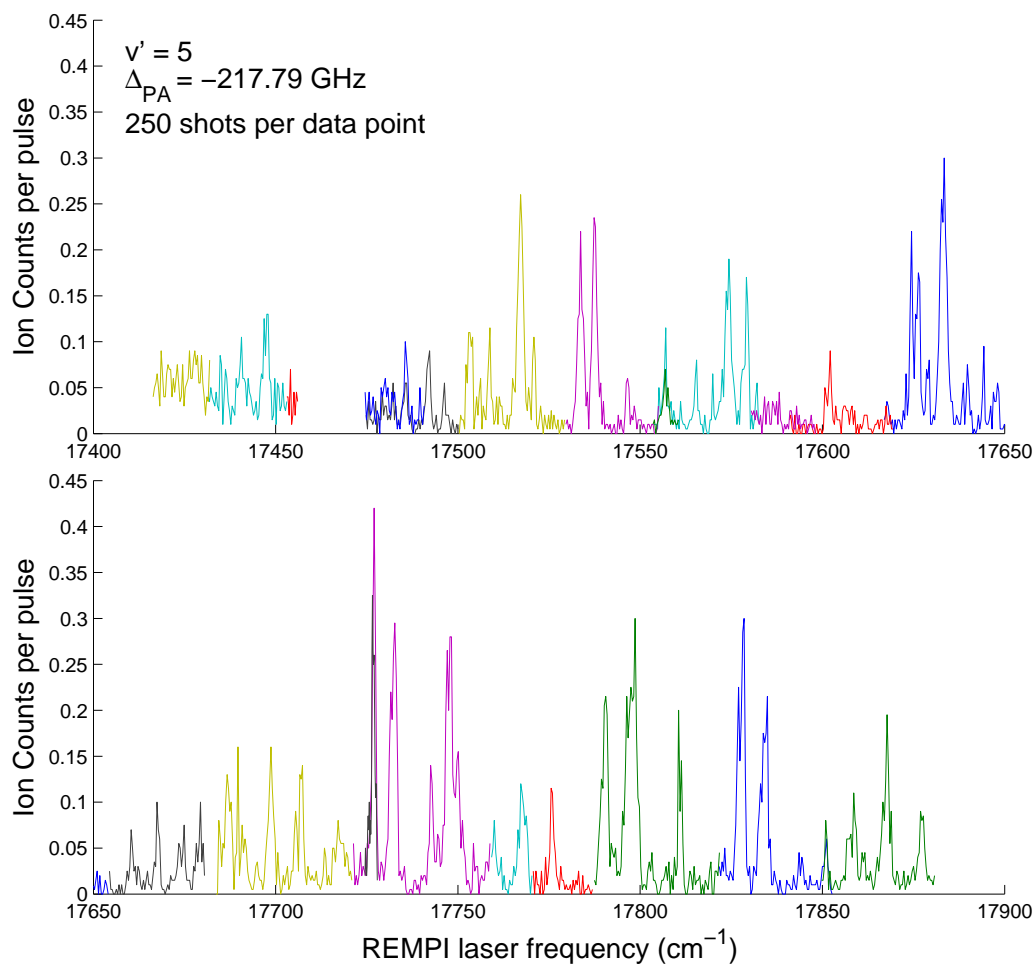


Figure 5.3. Raw REMPI scans taken while the PA laser is resonant with the $v' = 5, J = 1$ level of the $4(1)$ potential.

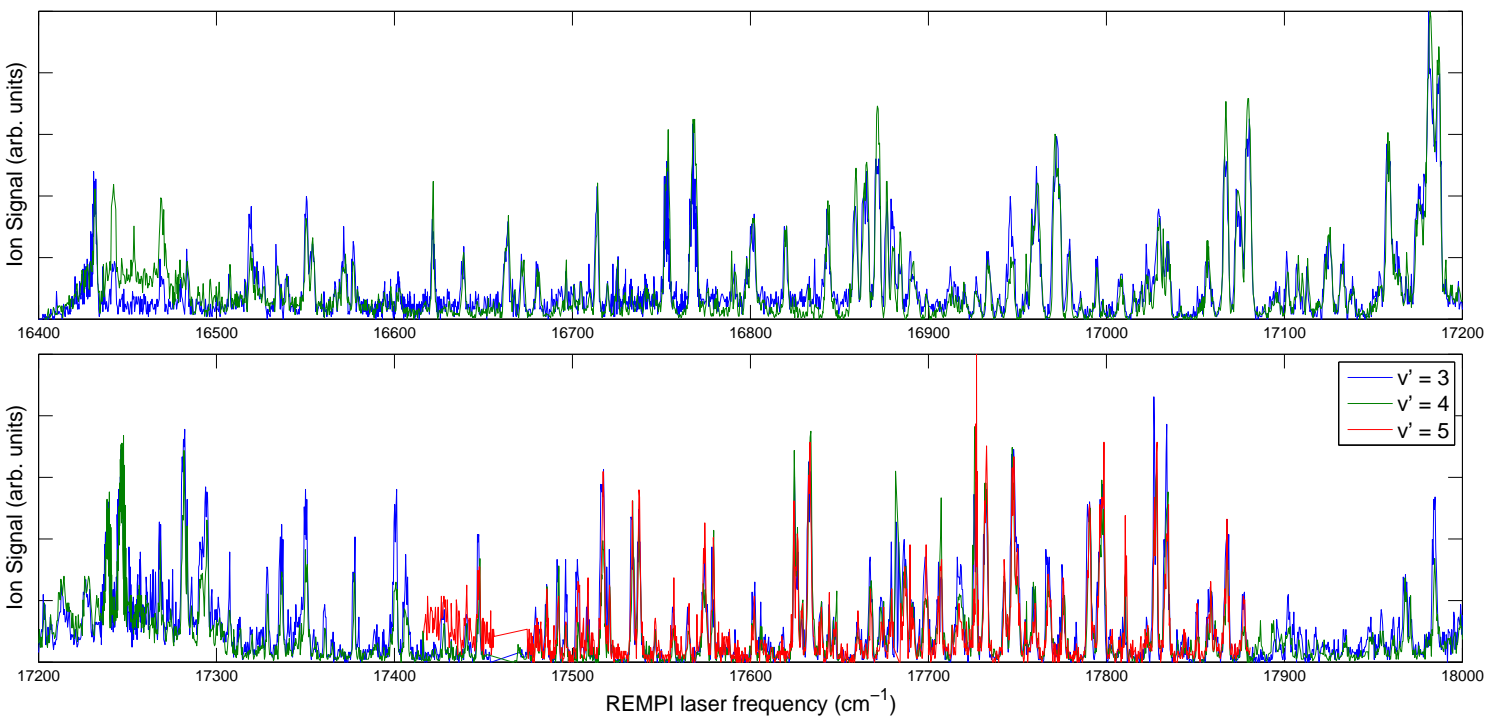


Figure 5.4. Normalized REMPI scans of the $v' = 3, 4, 5$ levels of the $4(1)$ potential.

5.1.3 Molecular Potentials Involved in REMPI

Because the $X^1\Sigma^+$ is so deeply bound ($D_e = 5927.9 \text{ cm}^{-1}$ [39]), several potentials can be involved in two photon ionization depending on the v'' states that are populated after PA. Figure 5.5 shows the various paths that can be taken. If high v'' are populated after PA, they should ionize through the $(4)^1\Sigma^+$ or $(5)^1\Sigma^+$ potentials. The $(4)^1\Sigma^+$ has a unique long range potential with a large classical turning point, even for deeply bound molecules, while the $(5)^1\Sigma^+$ is much shorter range. Considering that high v'' $X^1\Sigma^+$ molecules are going to be long range there is an expectation that the $(4)^1\Sigma^+$ participates more strongly in ionization because $|\psi_v|$ should be similarly large for both potentials at large R , where $|\psi_v|$ for $(5)^1\Sigma^+$ would be close to zero. If the molecule decays to moderately deep v'' , ionization through either the $D^1\Pi$ or $C^1\Sigma^+$ becomes possible. And for the most deeply bound states ionization could be enhanced by either the presence of $B^1\Pi$ or $C^1\Sigma^+$ states. The exact correspondence between v'' and the intermediate potential involved in ionization is discussed in more detail later.

5.2 $X^1\Sigma^+ \rightarrow D^1\Pi$ Transitions

To assign transitions to the lines seen in our spectra, we look for patterns and rely on previous theoretical and experimental work. One of the first attempts to find a pattern was to take the autocorrelation function of the recorded spectra, which is shown in figure 5.6. Unfortunately, the autocorrelation function yielded no strong peaks, as it did for spectra involving the $(3)^3\Pi$ potential. (See figure 4.4.) The lack of a clearly defined peak simply means that we are inducing transitions involving levels from anharmonic regions of the electronic potentials so that there is not a regular energy spacing. However, there is a weak correlation around 110 cm^{-1} .

As a clearly repeatable pattern is not seen, looking for transitions to the $D^1\Pi$ and $B^1\Pi$ potentials have the advantage that many of the vibrational level energies have already been measured in previous heat pipe experiments (see table 4.2). For levels

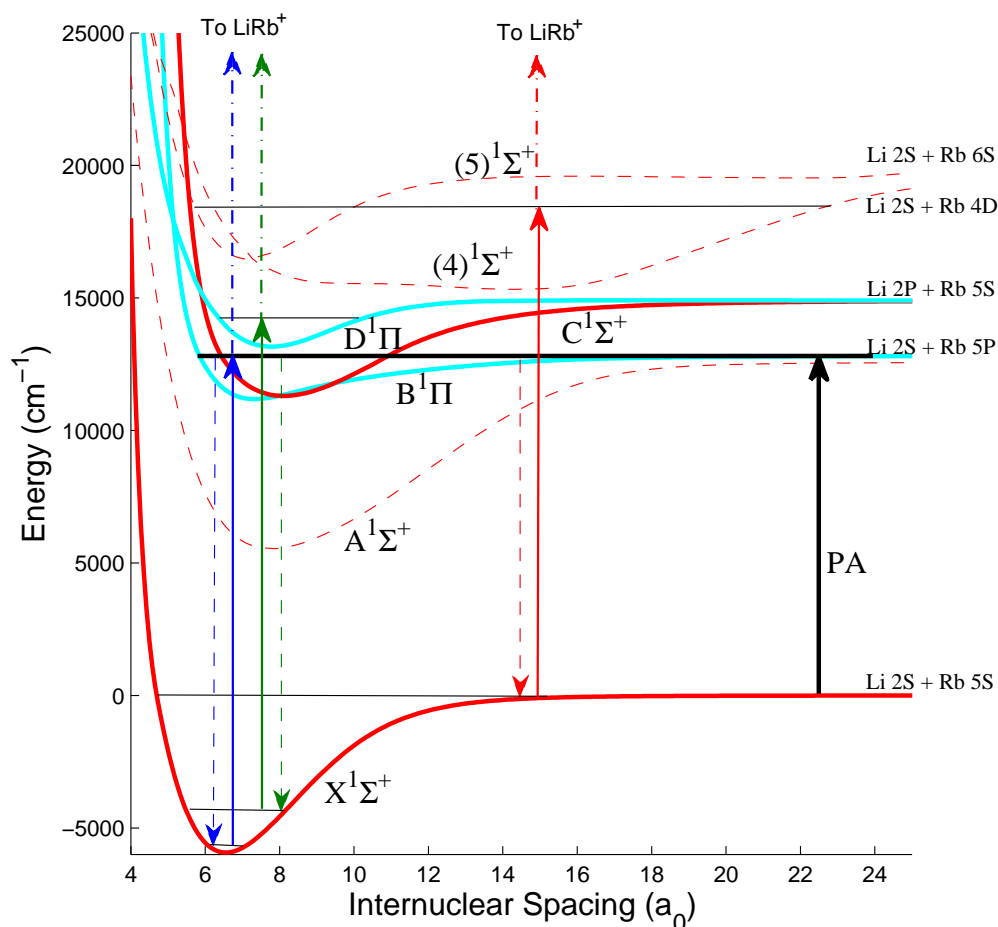


Figure 5.5. The possible pathways for REMPI from the $X^1\Sigma^+$ state depend on the decay path from PA. Only PECs through which $X^1\Sigma^+$ molecules could ionize are pictured. Weakly bound molecules would likely ionize through the $(4)^1\Sigma^+$ potential. The most deeply molecules can ionize through the $B^1\Pi$ or $C^1\Sigma^+$ potential. Moderately bound molecules can ionize through the $D^1\Pi$ or $C^1\Sigma^+$ potential.

that have not been observed, levels close to the highest observed level ($v' = 22$ for $B^1\Pi$ and $v' = 15$ for $D^1\Pi$) should still be accurately predicted by the calculations based on the experiment. The missing $v' = 11, 12, 14$ levels of the $D^1\Pi$ should also be quite accurately known considering they are in between known lines that have been fitted.

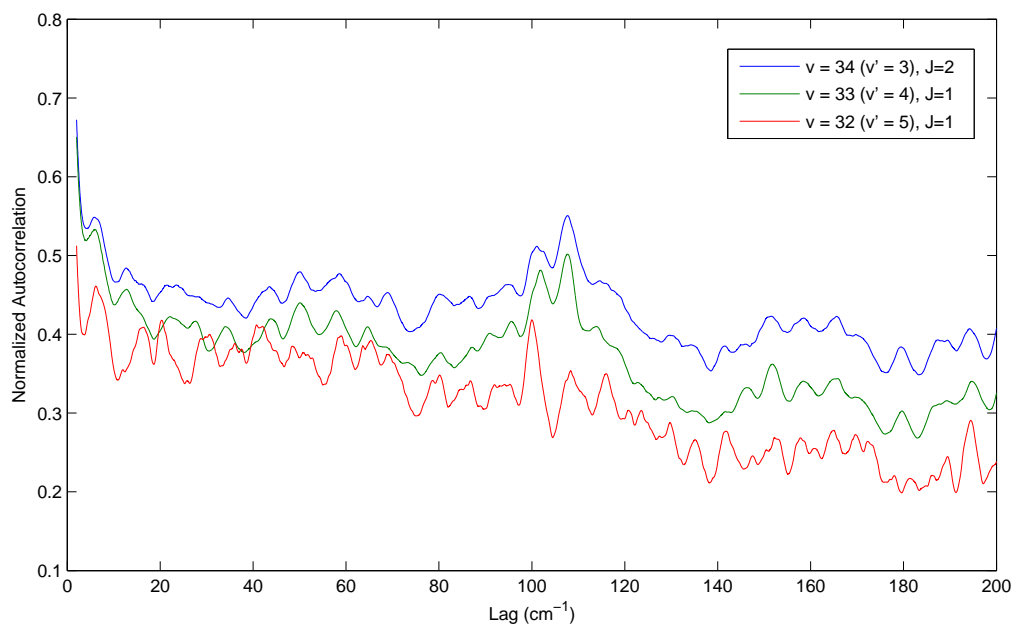


Figure 5.6. Auto correlation function for REMPI scans for molecules that have decayed to the $X^1\Sigma^+$ after PA to a vibrational level close to the dissociation limit of the 4(1) potential (correlates to the $B^1\Pi$ at close range).

There are 22 expected vibrational levels in the $D^1\Pi$ potential. In the $D^1\Pi$ potential, the $\Delta G_{v'}$ progression is cut off before it can approach zero because the C_6 coefficient of the $D^1\Pi$ is negative, meaning it is actually a repulsive potential at long range and the potential has a second extremum. This contributes to the low number of $D^1\Pi$ vibrational levels and about three quarters of the $D^1\Pi$ levels are quite well known. Based on the two photon ionization conditions from section 4.5, REMPI progressions involving the $D^1\Pi$ potential would have to originate from the $v'' = 7-26$ levels of the $X^1\Sigma^+$ state, provided the calculations in table 4.4 are accurate. Figure 5.7 shows the vibrational spacings for the $D^1\Pi$ potential calculated from the PEC Ivanova *et al.* using the LEVEL 8.0 software program [40, 116]. (LEVEL was used to calculate energy levels and FCFs for all the potentials mentioned in this chapter.) It

should be noted that observation of these transitions after decay from 4(1) potential, would be indicative of surprisingly deeply bound molecules.

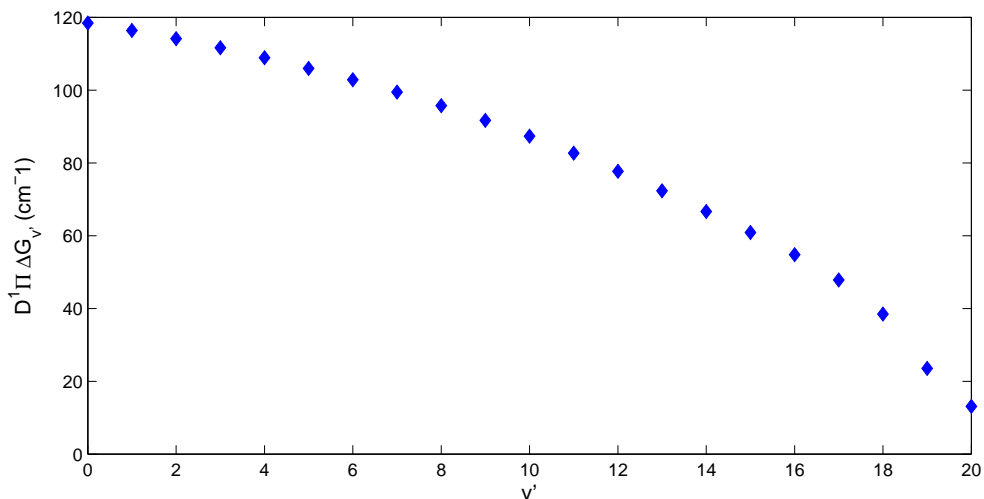


Figure 5.7. Vibrational energy spacing ($\Delta G_{v'}$) as a function of vibrational level (v') of the $D^1\Pi$ potential. Calculation of vibrational energy spacing is based on measurements from reference [40].

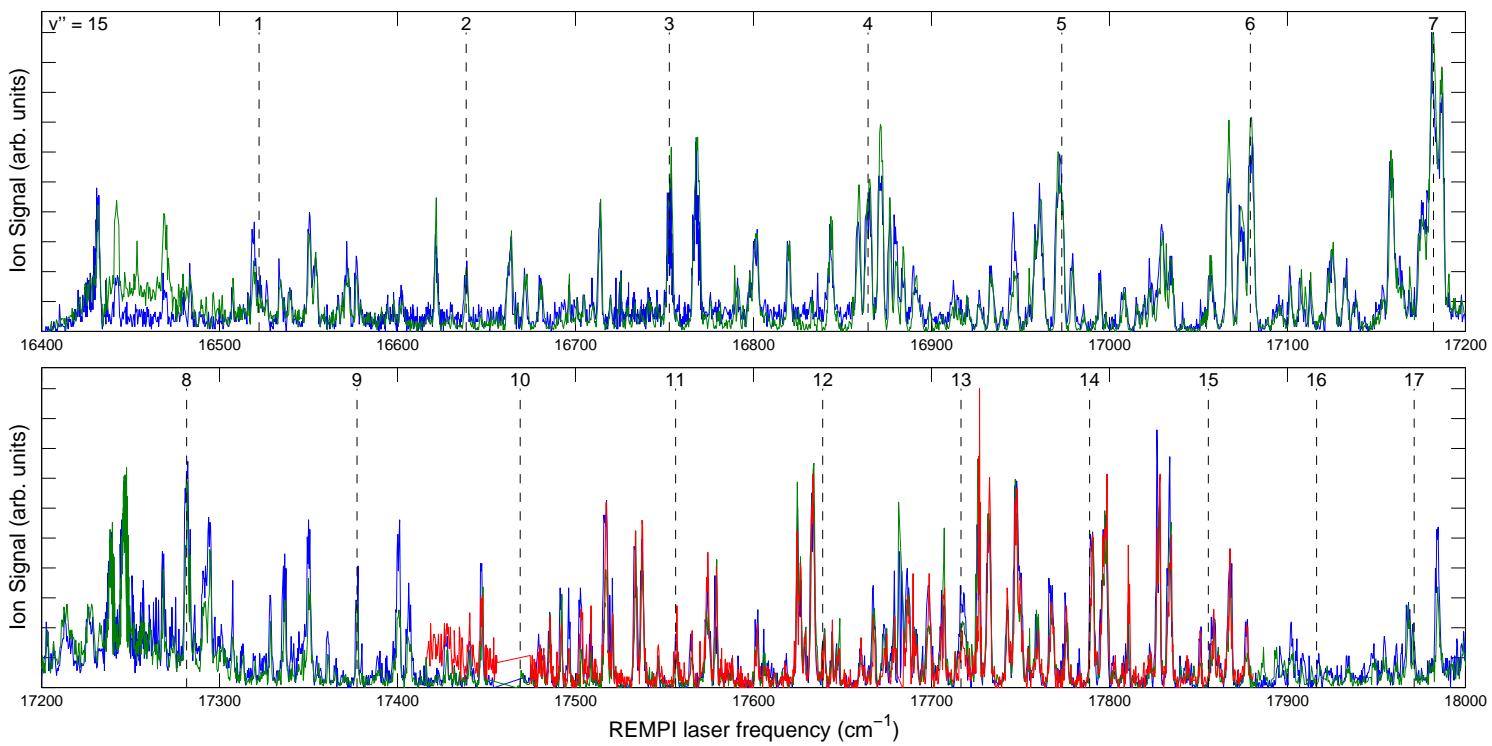
We start our assignment of lines by overlaying the $v'' = 15$ to $D^1\Pi$ energies over the REMPI spectra. There is a clear progression from $v' = 2$ –13. The $v' = 1$ transition is a smaller peak just to the right of a larger peak. There are lines close to the $v' = 14$ –16 energies, but they are either better assigned to other transitions or are too far away in energy to make the assignment. The transition to the $v' = 17$ is observed. The one photon energy for the $v' = 18$ transition is $> 18000 \text{ cm}^{-1}$ and therefore would not be observed. The $v'' = 15$ progression is confirmation that the LiRb^* molecules are decaying to deeply bound states and successfully assigns transitions to several of the strongest lines seen. The $v'' = 15 \rightarrow v' = 1$ line puts a lower limit on D_e for the $X^2\Sigma^+$ state of LiRb^+ of 3900 cm^{-1} . When we examine the energy difference of the strongest lines ($v' = 3$ –9), which are all between 95 – 115 cm^{-1} , they roughly are in line with the maximum from the autocorrelation function (figure 5.6). It is not

a sharp peak because the spacing changes by a few cm^{-1} each level, but it suggests other $X^1\Sigma^+ \rightarrow D^1\Pi$ progressions likely exist.

Other convincing $D^1\Pi$ progressions can be seen originating from other v'' levels of the $X^1\Sigma^+$ potential around $v'' = 15$. They are shown in figures 5.9 and 5.10 along with the $v'' = 15$ state for reference. The progressions are split between two figures so that the spectra can remain clear. Appendix B contains several tables of possible transitions in the 16400–18000 cm^{-1} range, lines that can be assigned in the spectra, and the progressions to which they belong. Not every possible transition marked in the figures is observed. All possible REMPI transitions which would satisfy the one and two photon conditions from section 4.5 for progressions originating from populated v'' levels are marked in the figures, but not all are observed because there may not be sufficient FC overlap.

There are some issues in attempts to assign transitions to the lines that appear in the REMPI spectra. First and foremost, there are 228 possible $X^1\Sigma^+ \rightarrow D^1\Pi$ transitions that would satisfy the two photon ionization conditions. Additionally there are over 150 $X^1\Sigma^+ \rightarrow B^1\Pi$ transitions to be addressed later, although transitions to high v' states of the $B^1\Pi$ may not be resolvable. There could also be transitions to the $C^1\Sigma^+$ state. The $C^1\Sigma^+$ state has not yet been directly observed, but rather only its perturbations on the $B^1\Pi$ and $D^1\Pi$ have been observed. When all possible transitions are viewed at the same time, it becomes difficult to unambiguously assign a line where two or more transitions have nearly the same energy. For example, this can be seen in figure 5.9 where the $v'' = 9 \rightarrow v' = 1$ transition has approximately the same energy as the $v'' = 11 \rightarrow v' = 4$ transition. Plotting progressions on separate figures can make them clearer to the eye, but can also cause lines to be assigned to the wrong progression if all lines are not viewed simultaneously. It is possible that multiple transitions are contributing signal to the same line should they have approximately the same energy and both ground states are populated, so it would also be incorrect to assign the line to a single transition in that case. The progressions shown in figures 5.9 and 5.10 are included because progressions of several lines can

Figure 5.8. Overlay of transitions from the $v'' = 15$ level of the $X^1\Sigma^+$ to $D^1\Pi$ levels.



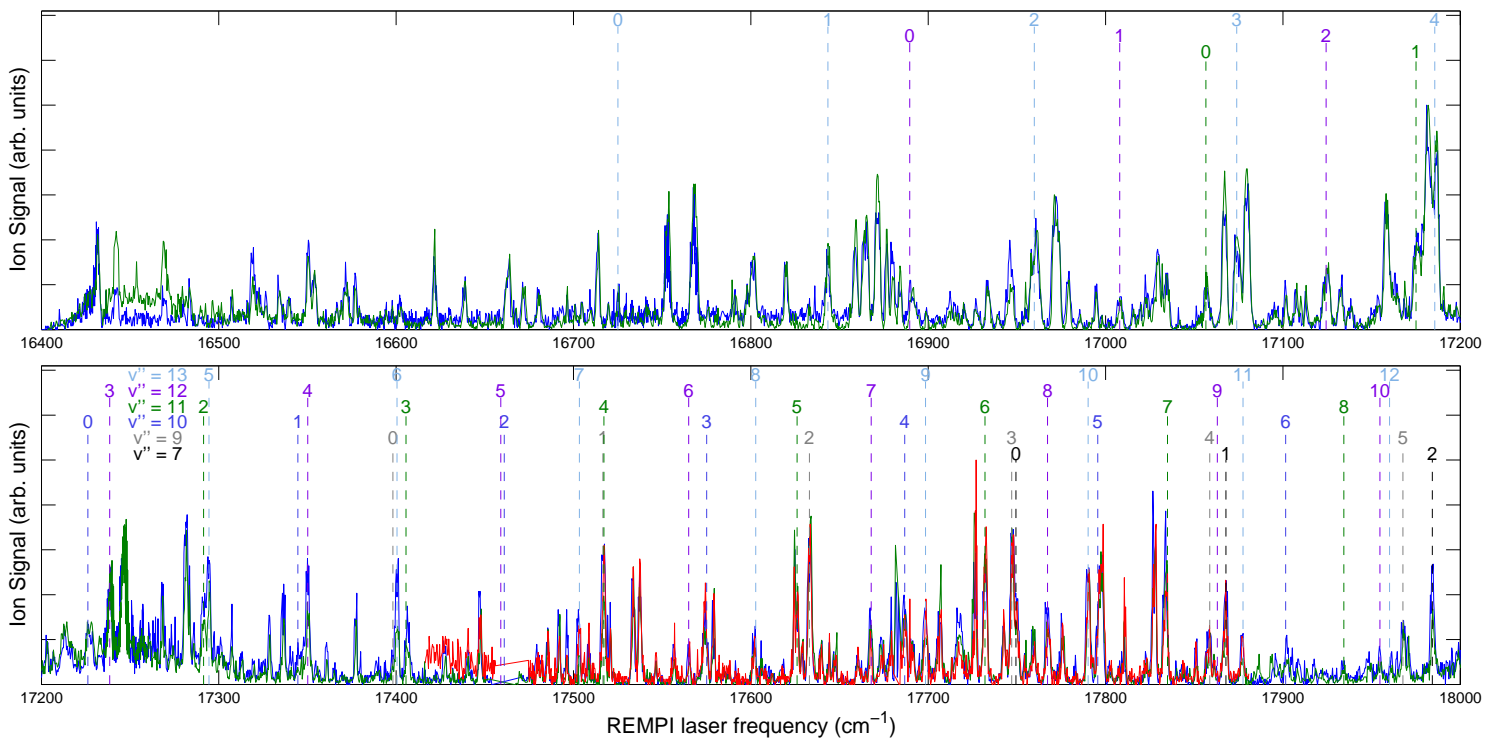


Figure 5.9. Transitions from the $v'' = 7, 9-13$ levels of the $X^1\Sigma^+$ to v' levels of the $D^1\Pi$ potential. Note that not every transition marked is observed.

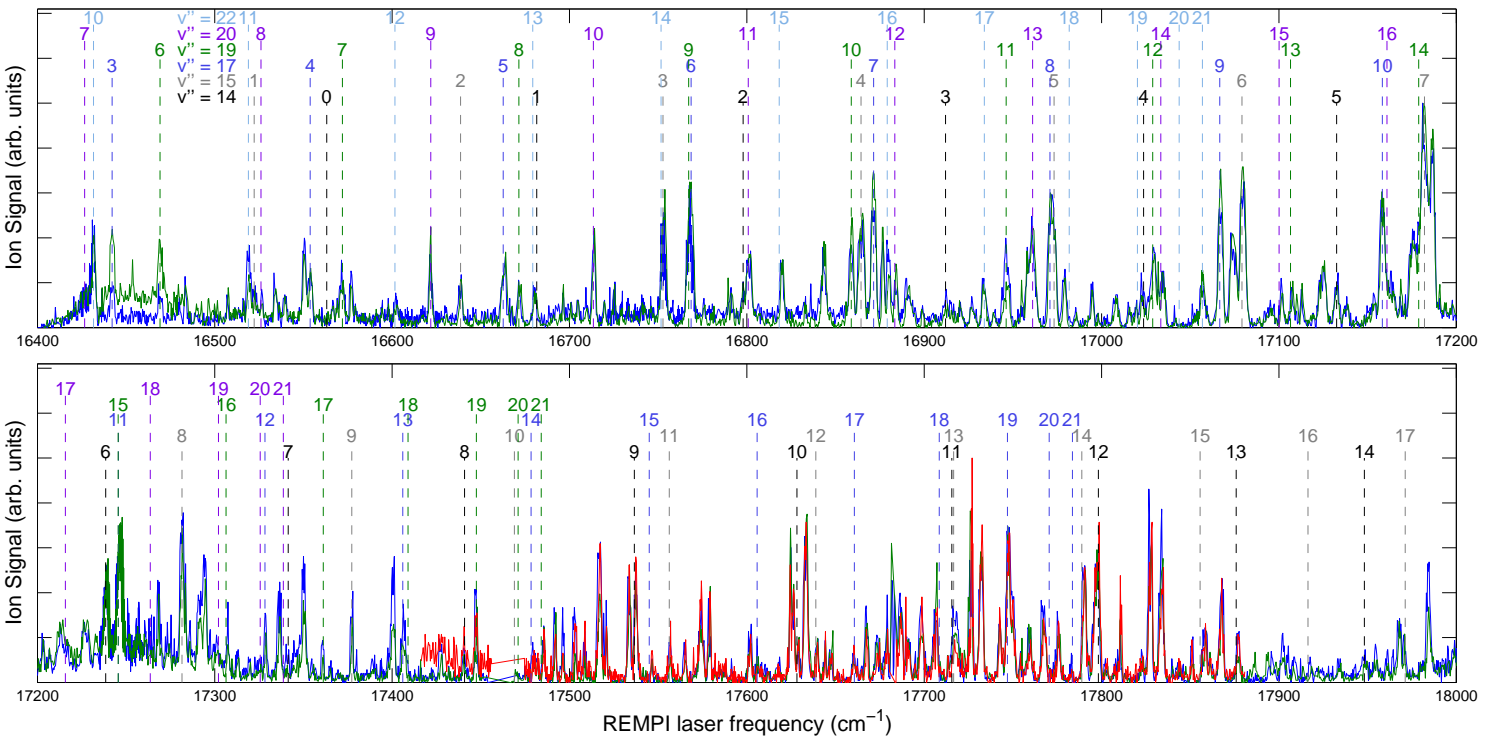


Figure 5.10. Transitions from the $v'' = 14, 15, 17, 19, 20, 22$ levels of the $X^1\Sigma^+$ to v' levels of the $D^1\Pi$ potential. Note that not every transition marked is observed.

be seen — ideally with some lines that can be identified unambiguously because no other known transitions are close. The $v'' = 7$ progression has only three observable lines, but two can be assigned fairly easily without “competition” from other possible assignments and the $v'' = 7 \rightarrow v' = 0$ transition may very well be present, but simply be hard to distinguish from other nearby lines. These issues are not helped by the fact that the PDL has a large linewidth and REMPI is inherently a low resolution process because of power broadening, causing nearby transitions to sometimes merge into a single line. It is sometimes possible to follow an intensity pattern as FCFs increase and decrease over various transitions to confirm progressions. In the $v'' = 15$ progression, the intensity is seen to increase from $v' = 1-7$ before decreasing for higher v' levels.

Another issue, is that transitions shown are based on a calculation for a potential where the previously highest observed vibrational level is $v' = 15$. Thus the transition energies for $v' > 15$ may require a correction from what is shown. As such, these transitions are considered less when establishing progressions to support population of a v'' state. There are some lines which can be assigned to $v' = 16, 17$ transitions with little or no correction, but the $v'' = 17, 19, 20 \rightarrow v' = 18$ transitions all appear at slightly higher energy than an observed line. However in the case of the $v'' = 19 \rightarrow v' = 18$, a correction to a lower energy would cause ambiguity, as it would then essentially have the same energy as the $v'' = 17 \rightarrow v' = 13$ transition. This highlights an issue of analyzing spectra where the initial states have been populated by spontaneous emission and the ground state populations are unknown. The spectra could immediately be made clear if, say, the $v'' = 17$ state had all or at least had a majority of the population. Even thermally excited states would follow a well known population distribution that can help assign transitions.

To contrast with the progressions observed in figures 5.9 and 5.10, figure 5.11 shows $X^1\Sigma^+ \rightarrow D^1\Pi$ possible progressions are not clearly seen. Transitions that would originate from the v'' states shown in figure 5.11 do not exhibit definitive progressions of consecutive lines in agreement with expected transition energies. There is an

occasional line or two that appears to match, but often they are better assigned to transitions from a more definitive progression. For example, there are lines that seem to correspond to $v'' = 16 \rightarrow v' = 15, 16$, but those transitions have similar energies to the $v'' = 13 \rightarrow v' = 9$ and $v'' = 9 \rightarrow v' = 2$ transitions which are part of stronger progressions. Because of a lack of clear progressions, these levels do not seem to be strongly populated after spontaneous emission. It should be noted that transitions originating from $v'' > 20$ would result in progressions to $v' > 15$ states which have not been previously measured and are more likely to be inaccurate. Having said that, if higher v'' states were being populated, one might notice a recurring consistent difference between the expected position of a line and an observed line, as was mentioned being a possibility for transitions to $v' = 18$.

5.3 $X^1\Sigma^+ \rightarrow B^1\Pi$ Transitions

The energy for the $X^1\Sigma^+, v'' = 6 \rightarrow D^1\Pi, v' = 0$ transition is 17928.67 cm^{-1} , making it the only $v'' = 6$ transition that could be observed between the $X^1\Sigma^+$ and the $D^1\Pi$ potentials, which is insufficient for establishing a progression. Transitions to higher v' states or originating from lower v'' states would be outside the range of the R590 dye used. However, transitions through a different potential may be possible. Population residing in $v'' < 7$ can be detected via transitions to the $B^1\Pi$ potentials while still satisfying the REMPI conditions from section 4.5. Because the $B^1\Pi$ is asymptotic to the $\text{Li } 2S_{1/2} + \text{Rb } 5P_{3/2}$ atomic state which lies 2087 cm^{-1} below the $\text{Li } 2P + \text{Rb } 5S_{1/2}$ asymptotic state corresponding to the $D^1\Pi$ potential, ionization through the $B^1\Pi$ involves many more high v' states than $X^1\Sigma^+ \rightarrow D^1\Pi$ transitions. Observed vibrational levels in the $B^1\Pi$ are $v' \leq 22$. For $v'' > 22$, corrections to calculated transition energies may be required as there are known discrepancies in the C_6 coefficient of the potential reported in reference [40] and the measured C_6 from our previous work [13, 55]. Also, uncertainty in the reported value of D_e could require the energy of calculated vibrational levels to be adjusted too.

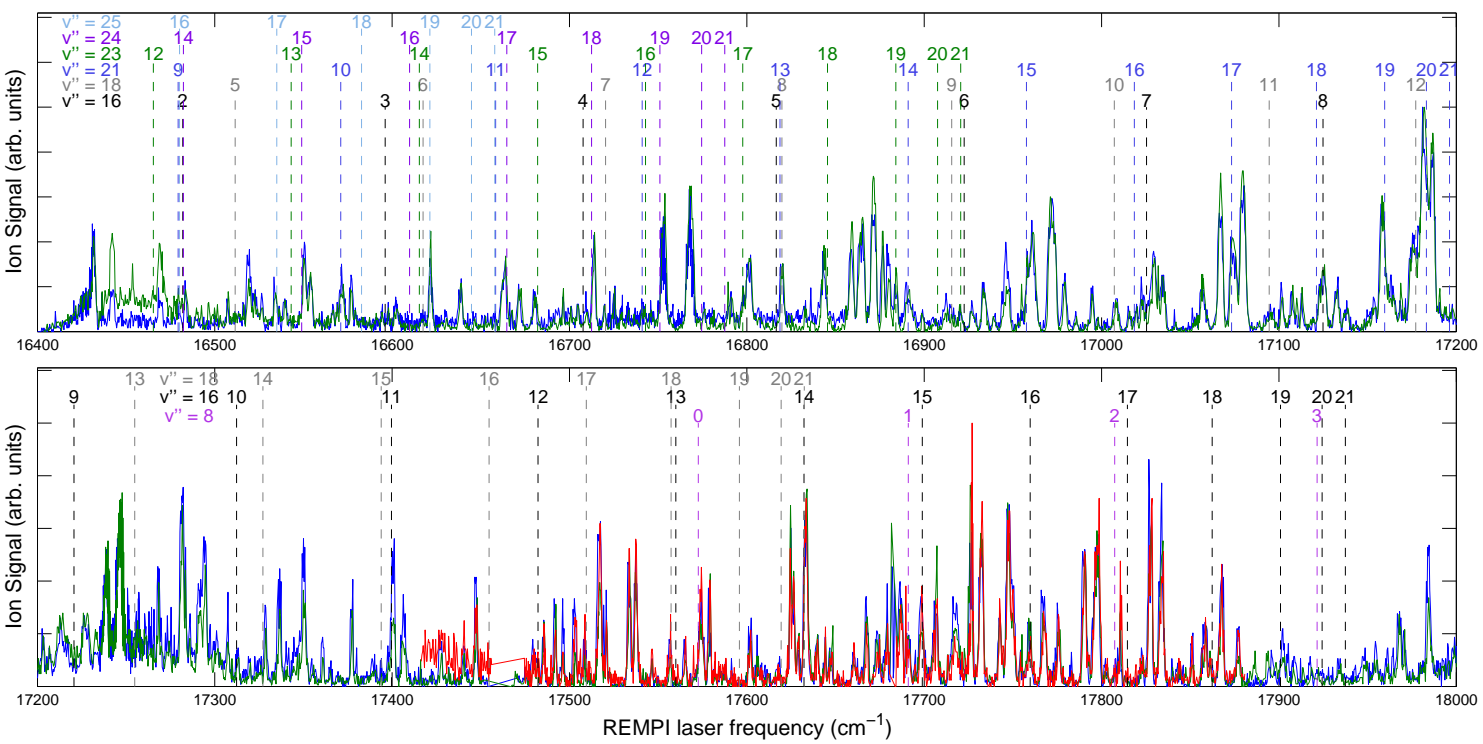


Figure 5.11. Transitions from the $v'' = 8, 16, 18, 21, 23-25$ levels of the $X^1\Sigma^+$ to v' levels of the $D^1\Pi$ potential, for which clear progressions are not seen.

$B^1\Pi$ transitions originating from the $v'' = 0-10$ states of the $X^1\Sigma^+$ could possibly be observed via REMPI between $16400-18000\text{ cm}^{-1}$. However, the number of states accessible can be an issue. At most, 4 transitions from the $v'' = 0$ state would be observable with one color REMPI, $v'' = 0 \rightarrow v' = 7-10$. This leaves a narrow range of lines with which to confirm that the ground state level is populated. This range could be expanded by using two color REMPI, which was not done in this experiment. There are 7 and 10 possible transitions to $B^1\Pi$ states for the $v'' = 1, 2$ states respectively. Many more transitions would be observable for $v'' \geq 3$, but starting with $v'' = 4$ a majority of these transitions would be to $v' > 22$ levels which have not yet been observed. Unlike the $D^1\Pi$, which is repulsive at long range, the $B^1\Pi$ vibrational levels become quite closely spaced close to the atomic asymptote, which can be seen in figure 5.12. The spacing required for levels to be clearly resolvable depends on the width of the line observed, which in turn depends on the strength of the transition, but in general peaks become clearly resolvable if their separation is $> 2\text{ cm}^{-1}$. For $B^1\Pi$, this means that transitions to the highest three v' states may be indistinguishable in a REMPI scan.

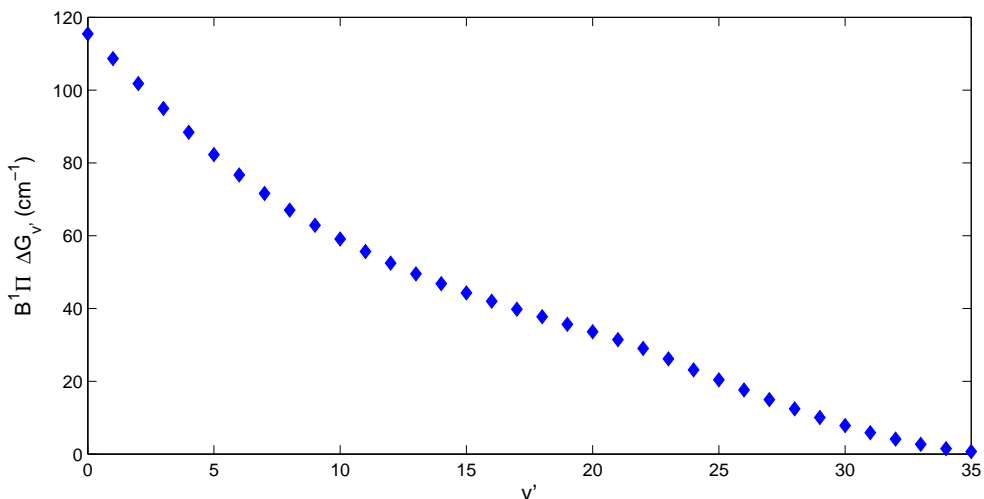


Figure 5.12. Vibrational energy spacing ($\Delta G_{v'}$) as a function of vibrational level (v') of the $B^1\Pi$ potential. Calculation of vibrational energy spacing is based on measurements from reference [40].

Molecules in the $v'' = 7-10$ levels of the $X^1\Sigma^+$ states discussed could ionize through either the $B^1\Pi$ or $D^1\Pi$ and still satisfy the REMPI conditions from section 4.5. We note a clear $v'' = 8$ progression through the $D^1\Pi$ was not observed. A lack of clear $B^1\Pi$ progressions from the $v'' = 7, 9, 10$ states does not contradict assigned $D^1\Pi$ progressions because the observed transitions also depend on the FCFs involved. For $B^1\Pi$ from these states, this would involve a transition from a deeply bound state to a weakly bound state. Roughly speaking this would correspond to a transition from a small to a large internuclear separation, which would be strongly suppressed according to the Franck-Condon Principle. However, there is an apparent internuclear spacing mismatch in the decay from weakly bound states involved in PA and the decay to deeply bound $X^1\Sigma^+$ level, so a better understanding of the FCFs would be required to say for certain what the intensity pattern should look like for $X^1\Sigma^+ \rightarrow B^1\Pi$ transitions.

Figure 5.13 shows transitions from the $X^1\Sigma^+$ state to $B^1\Pi$ state that would be observable through one color REMPI. No clear progressions are seen for $v'' > 5$. Because the observed potential progression are only seen at higher energies, only spectra between 17250–18000 cm^{-1} is shown for clarity. A progression from $v'' = 5 \rightarrow v' = 18-21$ is possible, but the $v' = 20$ would be missing because of a nearby Rb atomic resonance. $v'' = 5 \rightarrow v' = 25-27$ is another possible progression, but the $v' = 25$ transition is perhaps better assigned to the $v'' = 17 \rightarrow v' = 16$ transition through the $D^1\Pi$. The $v' = 26$ transition is also close in energy to either the $v'' = 14 \rightarrow v' = 10$ or $v'' = 11 \rightarrow v' = 5$ transitions, although it is less clear if the line should belong to either of those progressions from the $D^1\Pi$. There is a progression for $v'' = 4 \rightarrow v' = 14-18$, as well as a possible $v'' = 4 \rightarrow v' = 24-27$. Because the latter progression involves $v' > 22$, it is possible that the positions of these resonances do not exactly match the observed lines. There is a possible $v'' = 3$ progression. It is sporadic with possible $v' = 12, 13, 15, 16, 18, 19, 20$ transitions, but of those only the $v' = 16$ is not potentially attributable to $D^1\Pi$ progressions. The $v'' = 2 \rightarrow v' = 11-15$ progression is of particular interest, because $v'' = 2$ would be the lowest populated state, only the

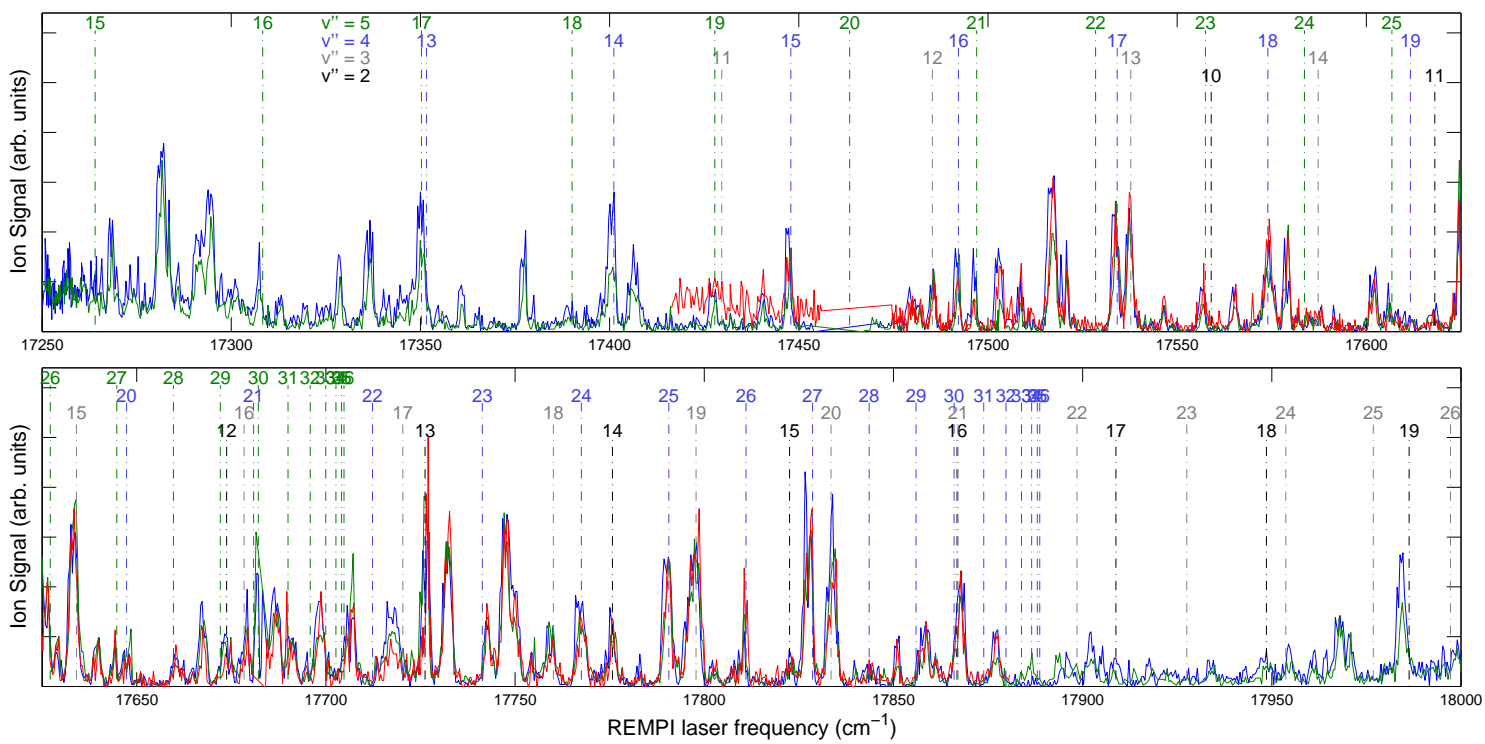


Figure 5.13. Transitions from the $v'' = 2-5$ levels of the $X^1\Sigma^+$ to v' levels of the $B^1\Pi$ potential for which some progressions are seen.

$v'' = 2 \rightarrow v' = 12$ transition is close to another $B^1\Pi$ or $D^1\Pi$ transition, and that is the $v'' = 5 \rightarrow v' = 29$ transition pictured, which is a less convincing assignment. If these assignments are correct, then they increase the lower bound of D_e for the $X^2\Sigma^+$ state of LiRb^+ . A two-photon transition through $v'' = 2 \rightarrow v' = 12$ would be 3902 cm^{-1} below the $\text{Li} + \text{Rb}^+$ asymptote and through the $v'' = 4 \rightarrow v' = 14$ be 3961 cm^{-1} below. Observing these transitions would place lower limits of $D_e = 3970 \text{ cm}^{-1}$ and $D_e = 4030 \text{ cm}^{-1}$ respectively using the theoretical calculation for ω_e from [115].

5.4 $X^1\Sigma^+ \rightarrow C^1\Sigma^+$ Transitions

There are around 500 possible transitions from $X^1\Sigma^+$ vibrational levels to $C^1\Sigma^+$ vibrational levels that satisfy the conditions from section 4.5 between $16400\text{--}18000 \text{ cm}^{-1}$. Attempts to check for all these transitions would likely require more specialized techniques. First, as demonstrated when looking for $B^1\Pi$ and $D^1\Pi$ transitions, there would be much ambiguity over assignments due to the density of possible lines. Resolving this ambiguity would require a method of ensuring that a single vibrational level contains all or a majority of the population to remove other populated states that add to the ambiguity. Secondly, knowledge of the $C^1\Sigma^+$ potential has only been achieved through observation of perturbations on $B^1\Pi$ states [40]. These perturbing states lie only at the bottom of the $C^1\Sigma^+$ potential. As such, only low v' states of the $C^1\Sigma^+$ potential would have trustworthy energy calculations, and these states would only be accessible from low v'' levels of the $X^1\Sigma^+$. We do not find many potential transitions to the $C^1\Sigma^+$ potential that are easily identifiable. Figure 5.15 shows the calculated transitions from the $v'' = 3, 4, 5$ $X^1\Sigma^+$ levels to $C^1\Sigma^+$ vibrational levels. There is a seemingly convincing progression from $v'' = 3$, but cross referencing the energies of those transitions with other possible transitions makes this assignment ambiguous. Transitions from $v'' = 4, 5$ have some lines that match, but perhaps not enough to establish a progression, especially after removing some labels which are, again, perhaps better attributed to other progressions. Two color REMPI could be

used to extend some progressions to lower energy, which could help determine whether these lines belong to $C^1\Sigma^+$ states, but since so few lines from the $C^1\Sigma^+$ potential would be known to accuracy comparable to $B^1\Pi$ or $D^1\Pi$ lines, it is difficult to assign them to $C^1\Sigma^+$ states over those of other potentials. Figure 5.14 shows the calculated spacings of vibrational levels of the $C^1\Sigma^+$ potential for reference. $\Delta G_{v'}$ towards the bottom of the potential is about 110 cm^{-1} , but since a photon to the bottom of the potential has insufficient energy to ionize, many of the possible progressions likely occur when $\Delta G_{v'}$ is decreasing as v' increases.

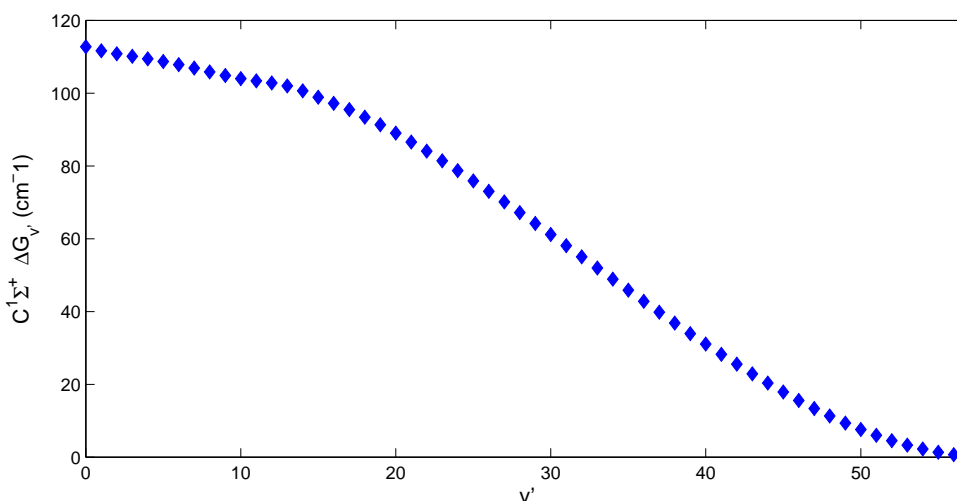


Figure 5.14. Vibrational energy spacing ($\Delta G_{v'}$) as a function of vibrational level (v') of the $C^1\Sigma^+$ potential. Calculation of vibrational energy spacing is based on measurements from reference [40].

5.5 Lack of Evidence for Observing Decay at Large Internuclear Separation

Because PA is, in general, a long range process the strongest PA transitions are those to high vibrational levels and thus the most weakly bound states of a potential. The vibrational wavefunction, ψ_v of these states have large amplitudes at large internuclear separation and thus these states have the best FC overlap with the scat-

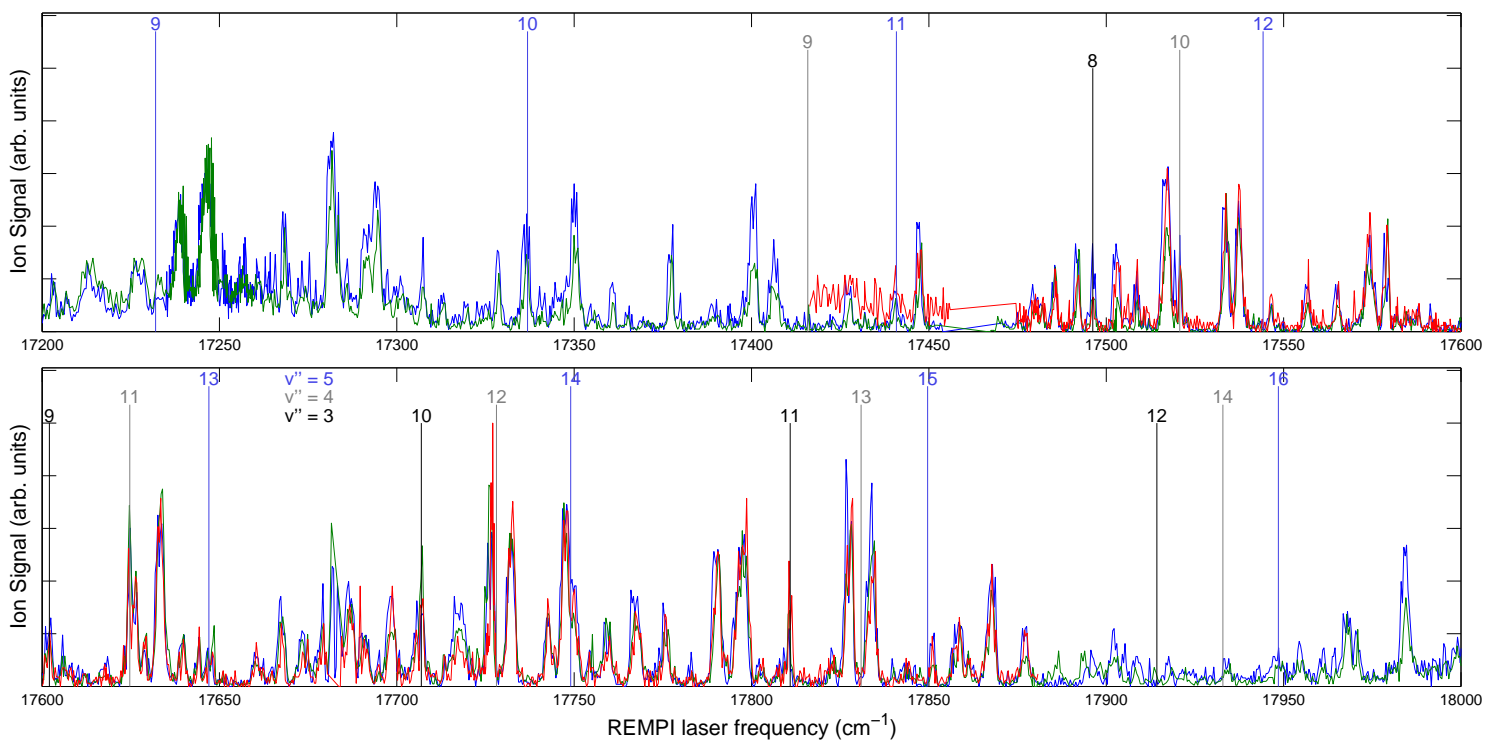


Figure 5.15. Transitions from the $v'' = 3-5$ levels of the $X^1\Sigma^+$ to v' levels of the $C^1\Sigma^+$ potential for which some progressions are seen.

tering state in which the atoms initially started. As such, the expectation is that the majority of molecules formed by PA should decay into a high vibrational levels of the electronic ground state potential because the vibrational wavefunctions of the ground states should have similarly large amplitudes at large internuclear spacing. Also, if the excited molecules are decaying at large internuclear separations, then they should follow selection rules for Hund’s case (c). Molecules in the 4(1) potential could decay into any of the ground state potentials: $1(0^+)$, $1(0^-)$, and $1(1)$. $1(0^+)$ correlates to the $X^1\Sigma^+$ at short range, but the $1(0^-)$ and $1(1)$ correlate to the $a^3\Sigma^+$ state which has already been partially mapped out by our previous work. If any significant portion of the population was decaying into the $a^3\Sigma^+$ potential, then one would expect to see lines that have already been observed. Most notably, one would expect to see the triplets observed due to the spin orbit interaction in the $(3)^3\Pi$ state as shown in figure 4.3. We do not see these triplets which were observed in REMPI spectra for PA to the $2(0^-)$ potential in the spectra for PA to the 4(1) potential. The lack of lines that can be attributed to $a^3\Sigma^+$ suggests that Hund’s case (c) rules may not apply, but rather the Hund’s case (a) in which the only possible decay path is to $X^1\Sigma^+$ states. If true, this means that these 4(1) states are not decaying at large internuclear separations.

5.5.1 FCF Calculations Based on Spectra from Heat Pipe Results

To further examine the issue of internuclear spacing when our LiRb^* molecules decay after PA, we can look to FCF calculations and determine if they are reflected in our spectra. Figure 5.16 shows the FCFs between the states used for PA and the $v'' \geq 48$ levels of the $X^1\Sigma^+$ state. The FCFs were calculated using using potentials derived from heat pipe experiments in LEVEL [39, 40, 106, 116]. These potentials are derived using lower lying vibrational states ($v' \leq 22$ for $B^1\Pi$ and $v'' \leq 45$ for $X^1\Sigma^+$) and thus calculations involving high v states should not be assumed to be numerically accurate. For example the C_6 value used for the potentials at large R

does not match our observed C_6 values found in table 4.3. We might expect that the FCF calculations should reinforce some qualitative expectations. However, the FCFs are calculated by solving for the wavefunctions that arise from two potentials without any information regarding other potentials or states that may perturb or affect the actual wavefunctions. Thus, when measurements deviate from FCF calculations, it is very possible that the wavefunction calculations are missing some important interactions.

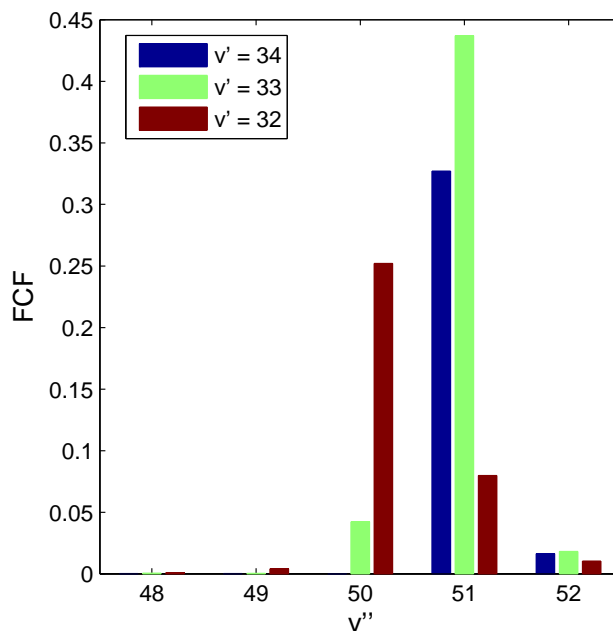


Figure 5.16. The Franck Condon Factors between vibrational $B^1\Pi$ and $X^1\Sigma^+$ levels. The $B^1\Pi$ potential is calculated from reference [40] and the $X^1\Sigma^+$ is calculated from reference [39]. The largest FCF for $v'' < 48$ from these calculations is 3.45×10^{-3} .

Figure 5.16 indicates that the $B^1\Pi$ levels that correlate to our 4(1) levels used in PA should decay to only the top three levels of the $X^1\Sigma^+$ state, with lower levels having FCFs two orders of magnitude smaller. The expectation from these calculations is that the molecules created should decay to high v'' states because the FCFs are dominated by ψ_v at large R where, presumably $|\psi_v|$ is largest for both the $B^1\Pi$ and

$X^1\Sigma^+$ states. If this were the case one should be able to detect a small scale pattern due to the ground vibrational state spacing that is repeated at the vibrational spacing of the excited intermediate state involved in the REMPI process. The spacing of the highest three vibrational levels should only be on the order of $\approx 1 \text{ cm}^{-1}$. We do not observe such a pattern.

5.5.2 Theoretical Properties of the $(4)^1\Sigma^+$ Potential

If we are observing the $(4)^1\Sigma^+$ potential in our spectra, (even after accounting for the fact that levels below the highest v'' are being populated) it would be helpful to know some of its properties. The potential shown in figure 5.5 is an *ab initio* calculation from [106]. It does not follow the typical Morse potential (A.15) often used to approximate molecular potentials. Figure 5.17 shows, the calculated vibrational level energy spacing, $\Delta G_{v'}$, of the $(4)^1\Sigma^+$ potential. Over a very broad range $\Delta G_{v'}$ stays between 40 and 45 cm^{-1} [116]. While the quality of the calculation has not been verified experimentally, there should be some region of fairly equally spaced energy levels. If we are ionizing high v'' states, the intermediate state providing the resonant enhancement should roughly be between $v' = 30\text{--}70$ of the $(4)^1\Sigma^+$ potential for PDL frequencies between 16400–18000 cm^{-1} . However, the autocorrelation function (figure 5.6) of the spectra shows nothing indicative of evenly spaced vibrational levels similar to what was seen in figure 4.4. Even if there were peaks due to the $(5)^1\Sigma^+$ or progressions stated to overlap, one would expect some distinct signal in the autocorrelation function to reveal excited state energy spacing if they are staying fairly constant.

The conclusion to be drawn from figures 5.17 and 5.6 are that either the calculated $(4)^1\Sigma^+$ is wrong or that there is simply little or no ionization occurring through the $(4)^1\Sigma^+$ potential. The lack of a signature from the $(4)^1\Sigma^+$ potential combined with the lack of observation of any transitions that originate from the $a^3\Sigma^+$ potential present strong evidence that the LiRb^* molecules formed via PA to the $4(1)$ at large

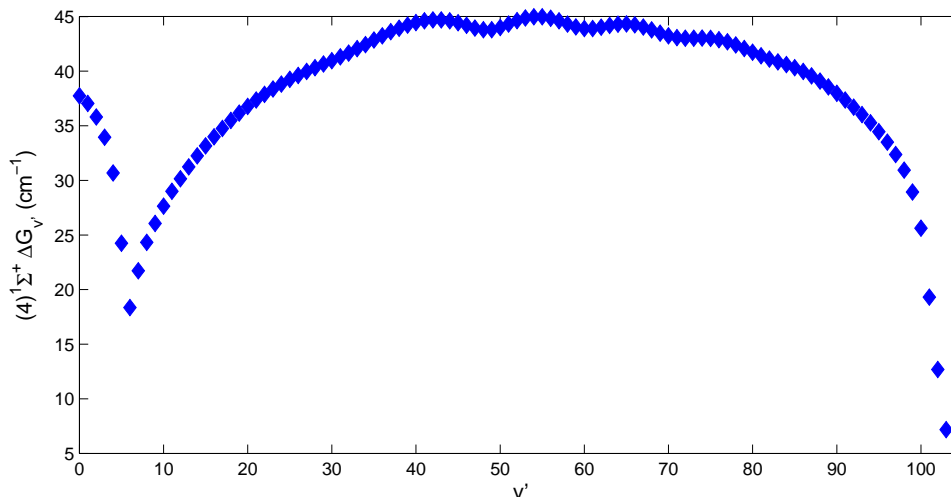


Figure 5.17. Vibrational energy spacing ($\Delta G_{v'}$) as a function of vibrational level (v') of the $(4)^1\Sigma^+$ potential. Calculation of vibrational energy spacing is based on *ab initio* PEC calculation from reference [106].

R are somehow decaying at a much smaller R , where they are obeying Hund's case (a) transition rules. This means that when assigning lines to our spectra, we should essentially ignore expectations of what v'' states are being populated based on FCF calculations. The exact physical reason for why this should be the case is unclear and is beyond the scope of this thesis, but we note that the $C^1\Sigma^+$ potential has a large D_e such that it actually crosses the $B^1\Pi$, potential even though it is asymptotic to the atomic Li 2P + Rb 5S state, while the $B^1\Pi$ potential is asymptotic to the lower Li 2S + Rb 5P state. In the case of mixing between the $C^1\Sigma^+$ and $B^1\Pi$ state, there could be enhancement of ψ_v at smaller R because of the $C^1\Sigma^+$ state have a much smaller outer turning point at these energies.

5.5.3 Observed Differences in REMPI Spectra from Different J states

A final observation that points toward deeply bound population instead of weakly bound, is the difference between the spectra that were taking via PA to a $J = 1$ state

and spectra taken via PA to a $J = 2$. Figure 5.18 shows regions of the spectra where differences in line shapes can be seen depending on whether molecules are formed in a $J = 1$ or $J = 2$ state. Difference in line shapes are seen in peaks occurring close to 17490 cm^{-1} , 17560 cm^{-1} , 17705 cm^{-1} , 17790 cm^{-1} , and in two peaks close to 17830 cm^{-1} . In each of these, either the $J = 1$ peaks appear shifted slightly up in frequency or there is an apparent doublet structure where the peak at higher frequency is larger when the PA laser is on a $J = 1$ line and the peak at lower frequency is larger when the PA laser is on a $J = 2$ line. Because the $J = 2$ can decay to $J = 1, 2, 3$ states, where $J = 1$ can decay to $J = 0, 1, 2$ states that would require a slightly higher frequency for a REMPI transition, a possible explanation for this observed asymmetry is that this is an effect of the rotational states being populated. The distance between the peaks of the doublets is quite large however. In the case of the doublet just below 17830 cm^{-1} , the two peaks are measured at 17826.6 and 17828.2 cm^{-1} . The positions and structure of these doublets are repeatable. The rotational constant, B_v for the $v'' = 0$ state of $X^1\Sigma^+$ potential is 0.216 cm^{-1} [38]. Low vibrational levels $v'' > 1$ have slightly smaller values for B_v , but too small to be resolved by a coarse REMPI scan. High vibrational states have much smaller values for B_v that are $< 0.05\text{ cm}^{-1}$. A spacing of 1.6 cm^{-1} is on the order of the difference between the $J = 2$ and $J = 3$ levels of the ground vibrational state. If rotational structure is the cause of these differences that depend on J , they could only be explained by deeply bound population.

To test if PA to different J states is really affecting ground state population, we performed PA scans while the REMPI laser is on one of the two peaks of the $17826.6/17828.2\text{ cm}^{-1}$ doublet. If they represent different vibrational levels, then a PA scan through the $J = 1$ and $J = 2$ states of the $4(1)\ v' = 3, 4$ levels should look roughly the same, as the rotational state should not affect vibrational level population after decay to the ground state. Figure 5.19 shows that there is a noticeable difference in the relative intensities of the $J = 1$ and $J = 2$ peaks depending on the frequency of the REMPI laser. This suggests that the differences observed in REMPI spectra produced by PA to $J = 1$ versus $J = 2$ states is an effect of the population of ground

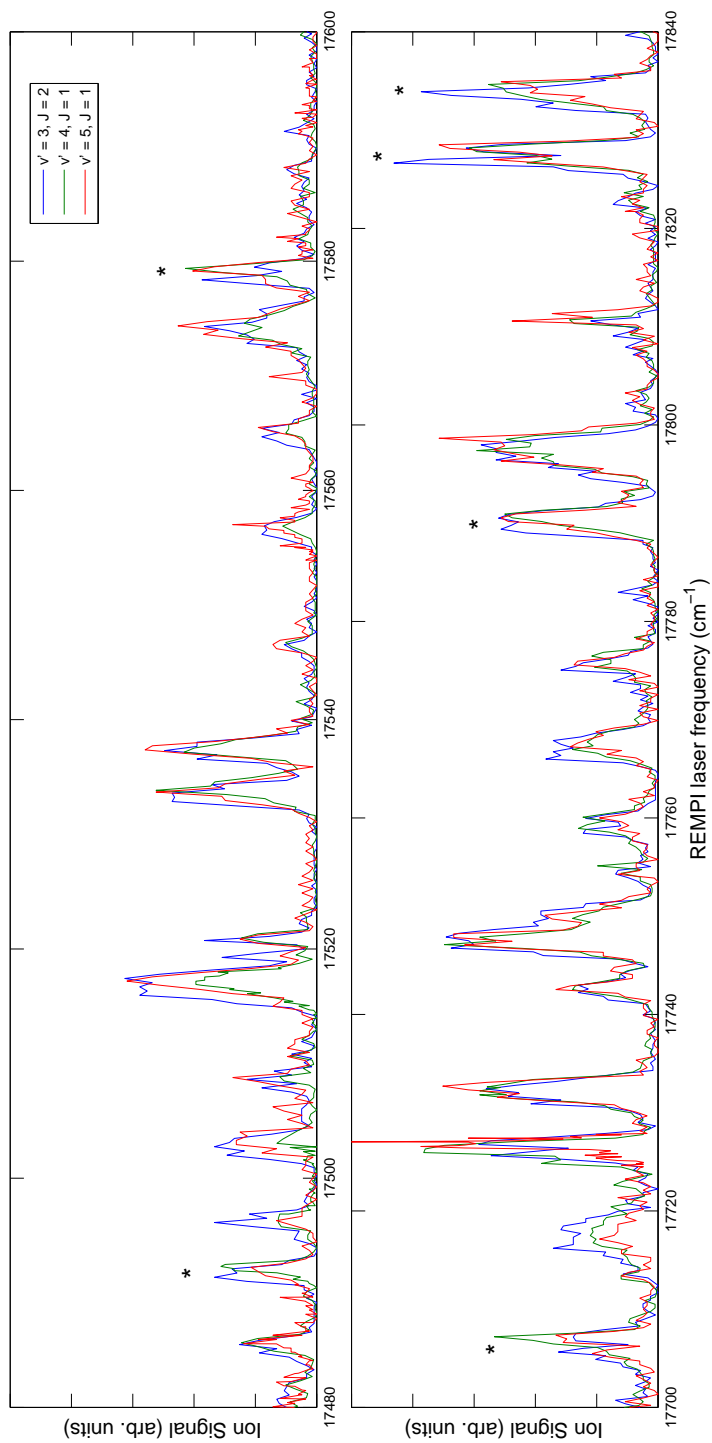


Figure 5.18. Differences in observed line shapes between spectra taken via PA to a $J = 1$ state (red and green) and PA to a $J = 2$ state (blue) of 4(1) vibrational levels. Peaks with differences are noted with an asterisk (*).

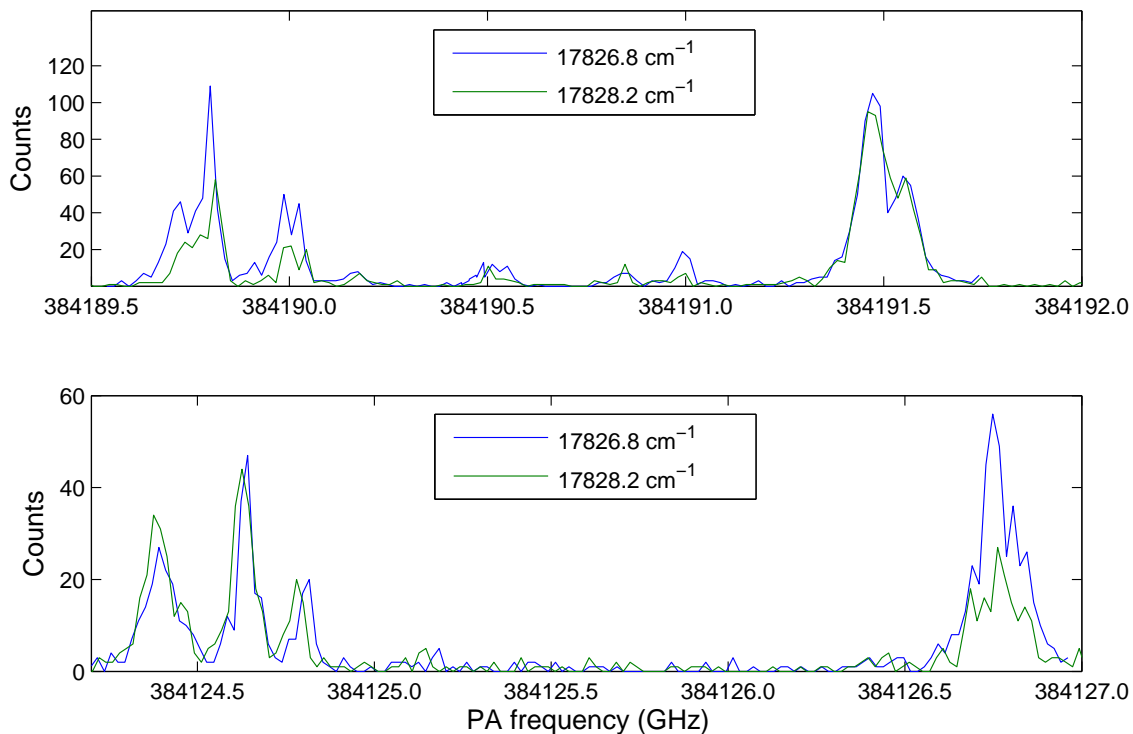


Figure 5.19. PA scans of the $4(1) v' = 3, 4$ levels at different REMPI frequencies. Changing the REMPI frequency changes the relative signal intensities of the $J = 1$ and $J = 2$ lines for the two vibrational levels.

state rotational populations. In this case, the fact that the separation between the doublets is so large is more evidence that deeply bound vibrational levels of the $X^1\Sigma^+$ state are indeed being populated. However, we cannot measure the actual ground state rotational spacing because the REMPI does not produce lines narrow enough to resolve rotational structure. At most, we can say these observations are effects of the rotational structure.

5.6 Production Rates

We attempt to estimate production rate of molecules created via PA to the $v' = 3$ level of $4(1)$ state in the same way demonstrated on Adeel Altaf's thesis [55]. We

choose the $v' = 3$ because that was the strongest PA resonance. The number of ions detected depends on the number of molecules in a given state N_a , the ionization probability p_{ion} , and the detector efficiency, e_d .

$$N_{ion} = N_a p_{ion} e_d \quad (5.1)$$

The ionization probability, $p_{ion} = 1 - e^{-\sigma E \lambda / hc \pi \omega^2}$, where ω is the photoionization cross section. Considering the experimental conditions are nearly identical to the previous calculation ($N_{ion} \approx 2$ for the strongest lines), and the same estimates could be applied to calculate p_{ion} (7×10^{-3} – 7×10^{-4}) and e_d (0.1–0.8). The number of molecules in a given state at the time of ionization is between 10^2 and 10^4 . The rate at which a given level is populated R_p is related to $N_a(t)$ by

$$N_a(t) = \frac{R_p t}{1 - t/\tau} \quad (5.2)$$

where τ is the transit time of a molecule in the beam volume (≈ 9 s at 1 mK). Note that this is not a calculation of the PA rate. The FCF is not included in this analysis, because, as has been discussed, the calculated FCFs do not accurately reflect the observations made. Thus an estimate of the rate at which molecules are produced in in a given level that results in the strongest lines is between 10^4 and 10^6 s $^{-1}$. Since we are populating a number of states, total molecule production rate in all states is likely roughly 10 times higher. The relative population in each state could be estimated by looking at the peak intensities, but because those peak intensities depend on the ground state population and the FCFs for the two REMPI steps, the level of uncertainty would be quite high as the FCFs are not well known. $v'' = 15$ appears to be the most populated state because the D $^1\Pi$ $v'' = 15 \rightarrow v' = 7$ transition is the strongest seen.

5.7 Conclusion

When we examined the REMPI spectra for molecules formed via PA to the $v = 3, 4, 5$ levels of the 4(1) potential, we found all three were remarkably similar spectra.

Apparently, weakly bound levels of the $4(1)$ potential all have quite similar decay paths. We examined the REMPI spectra for possible progressions due to the $D^1\Pi$ and $B^1\Pi$ potentials which have previously been observed in heat pipe experiments. Surprisingly, we discovered many progressions from $X^1\Sigma^+$ to the $D^1\Pi$ potential, and a few to the $B^1\Pi$ potential as well. From these progressions, we conclude that the spontaneous decay of weakly bound LiRb formed by PA to the $(4)1$ potential is somehow forming deeply bound molecules. The most populated level of the $X^1\Sigma^+$ potential is apparently the $v'' = 15$. There is evidence to support population as deeply bound as the $v'' = 2$ level. These progressions also place a lower bound on the depth of the $X^2\Sigma^+$ potential of LiRb^+ , D_e , as these REMPI transitions are not possible without a vibrational level of the ion existed at sufficiently low energy. The $15 \rightarrow 1$ transition of the $D^1\Pi$ potential puts a lower bound of 3900 cm^{-1} on D_e . Observing the $2 \rightarrow 11$ and $4 \rightarrow 14$ transitions to the $B^1\Pi$ potential increases that lower limit to 3970 cm^{-1} and 4030 cm^{-1} respectively, but these assignments are less definitive. All of the assignments run contrary to the expectation that PA to weakly bound molecular states should decay following Hund's case (c) selection rules to weakly bound vibrational levels of the $a^3\Sigma^+$ and $X^1\Sigma^+$ potentials. However we found no triplets that would indicate $a^3\Sigma^+ \rightarrow (3)^3\Pi$ transitions and we saw no evidence of the vibrational structure of the $(4)^1\Sigma^+$ state consistent with previous *ab initio* calculations.

6. Conclusion and Future Work

Finding that PA to weakly bound levels of the 4(1) potential will decay to deeply bound levels of the $X^1\Sigma^+$ potential suggests that there are new directions to be investigated in order to achieve the goal of producing LiRb in the rovibronic ground state. However, progressions with v' belonging to the $B^1\Pi$ potential rely on some assignments to levels that had not yet been observed, and some assignments which are ambiguous because of the possible presence of other transitions of similar energy. Finding other levels of the 4(1)/ $B^1\Pi$ potential through PA would bridge the gap between the $v' = 0-22$ levels observed and the weakly bound $v' = 3, 4, 5$ states of the 4(1) potential to create a complete picture of the $B^1\Pi$ potential. This would also be a way to independently confirm the energies of transitions seen in REMPI believed to be due to deeply bound molecules ionizing through the $B^1\Pi$ potential. Having independent verification of the energies of the $v' = 24-27$ levels of the $B^1\Pi$ would confirm that lines in the REMPI spectra are in fact due to population in the $v'' = 4$ level after spontaneous decay (see figure 5.13).

Some efforts have already been made to find additional PA lines. Figure 6.1(a) shows an attempt to find the $v' = 6$ line of the 4(1) potential. We determined the approximate position of the line by fitting previously observed levels to equation (4.2) and extrapolating to $v' = 6$. In order to accumulate enough shots that any signal is observable above noise, each data point was integrated over 1000 data points with roughly 50 MHz between each data point. At this level of integration it takes over a half hour to scan just 1 GHz. The PA power was 500 mW and the PDL frequency was 17826.7 cm^{-1} . Beam diameters are the same as reported in previous experiments. The peak detection rate near 383853.3 GHz is .04 counts per pulse. Several scans of this region were taken. The scan shown in figure 6.1 shows the cleanest PA peak. Other scans had poorer signal to noise because the number of background counts

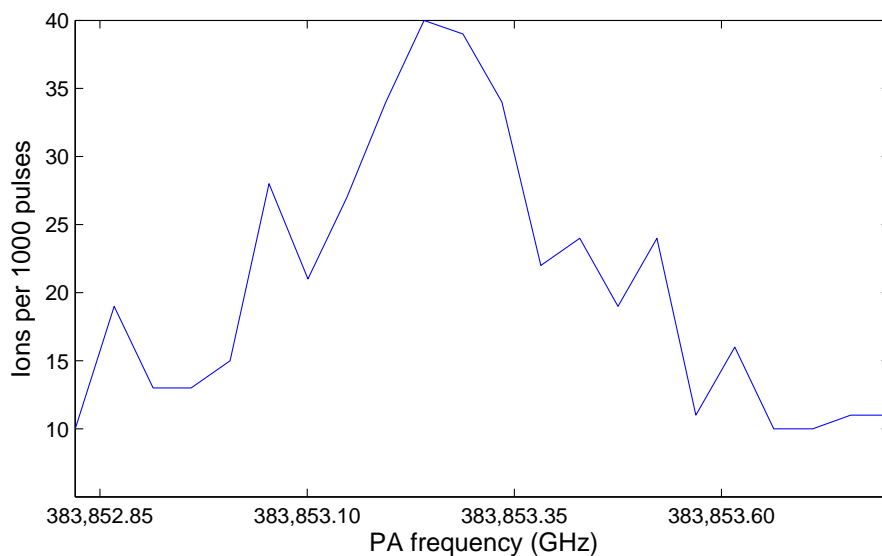
fluctuates, making a distinctive peak difficult to reproduce. Figure 6.1(b) shows how many counts were recorded on other strong REMPI lines, when the PA laser was held fixed at 383853.26 GHz versus when it was blocked. Despite the poor signal to noise that makes it difficult to see a distinct peak for some scans, there is a statistically significant difference in counts when the PA beam is present at 383853.26 GHz compared to when there is no PA beam, indicating that the resonance is likely real. We are uncertain what rotational line to assign because no structure is apparent beyond the main peak and the accompanying other rotational level was not found. ($J = 1$ and $J = 2$ lines were observed for all the other 4(1) PA measurements.) Another rotational line is expected roughly at either 3 GHz above or 3 GHz below this. Based on the extrapolation from equation (4.2), the better assignment is $J = 2$, but the uncertainty in the fit makes this assignment very tentative.

Improving the counting rate could help discover new PA lines. Currently our strongest lines yield 2.5-3 counts per pulse. Optimization of ion counting was done by varying the field plate voltages and the position of permanent magnets around the TOF region to steer ions onto the microchannel plate detectors. Currently the field plate voltages used are limited by the power supplies used and positioning permanent magnets can only be thought of as a coarse correction. It is possible a different power supply for the field plates and/or using magnet coils to finely control the path of the ions may improve the number of ions detected. How much of an improvement is unknown, but considering the weak signal of the $v'' = 6$ line, new PA lines will be difficult to find without some way of enhancing the signal.

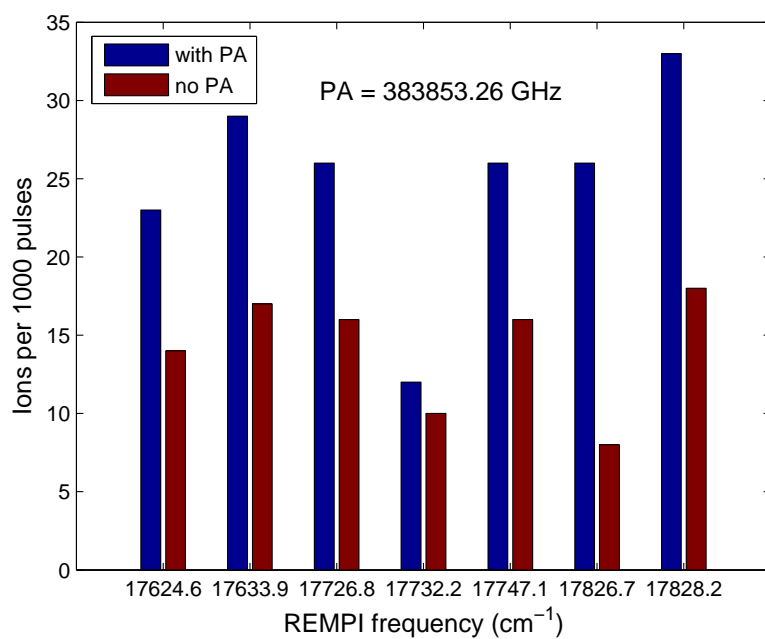
Additional information about the rotational structure of the lines we have already measured could be gathered via depletion spectroscopy [6]. The energy of the rotational levels for each vibrational level is given by

$$F_v(J) = B_v J(J+1) - D_v J^2(J+1)^2 + \dots \quad (6.1)$$

where J is the total angular momentum quantum number, B_v is the rotational constant for a given vibrational level v , and D_v is a correction that accounts for the fact the molecule is not a rigid rotor [112]. The correction term should be quite small for



(a) PA scan showing weak evidence of $v' = 6$ level of 4(1) potential.



(b) Ion counts per 1000 pulses on other REMPI lines with and without the PA laser.

Figure 6.1. PA Evidence of the $v' = 6$ level of the 4(1) potential.

the low J states formed by PA in a system of cold atoms. The constants B_v and D_v have been well measured for many vibrational levels in heat pipe experiments where rotational states can be thermally excited up to $J > 100$. Depletion spectroscopy could be used here to measure the rotational lines that are unresolved in REMPI spectroscopy. Shown in figure 6.2, if the narrow-band depletion laser is resonant with another transition, its population will be pumped out of the ground state vibrational level, reducing the REMPI signal. Depletion spectroscopy would allow for the rotational lines to be measured, which should give an accurate measurement of the rotational spacing F_v and rotational constant B_v . As B_v should be unique for different vibrational states, B_v should act as a fingerprint for the vibrational levels, making depletion spectroscopy another way of verifying the assignments we have made.

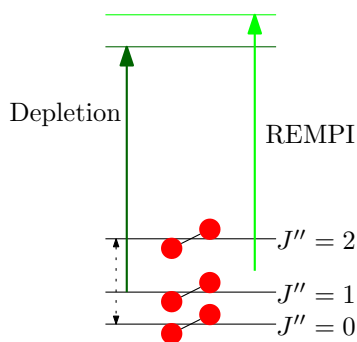


Figure 6.2. A schematic of depletion spectroscopy. Several J states are populated by spontaneous emission. The REMPI laser ionizes all rotational states at the same time through an excited resonance, but a depletion laser selectively removes population from a single rotational state when resonant with a different state, depleting the number of ions seen in the REMPI signal. Scanning the depletion laser gives a measurement of the rotational energy spacing.

Additional PA and depletion spectroscopy would only serve to confirm and refine the measurements and assignments we have made. Most of the current interest in ultracold molecules is focused on proposed experiments that require the molecule to be in the absolute rovibronic ground state — the $v'' = 0, J = 0$ state of the $X^1\Sigma^+$ potential. Perhaps the most intriguing aspect of the experimental results presented

is a possible new efficient pathway to the rovibrational ground state in LiRb. There is a strong PA rate to the $v' = 3$ level of the 4(1) potential. The strong decay to the $v'' = 15$ level indicates strong FC overlap between the two states. Rather than depending on a one-step transition from a scattering state to the rovibrational ground state, which did yield strong ground state production in LiCs via PA to the $v' = 4$ level of the $B^1\Pi$ state [6], it is possible that the most efficient route to the rovibrational ground state in LiRb is a two-step process. First PA to the $v' = 3$ state of the 4(1) potential, which we observe decaying strongly to the $v'' = 15$ level of the $X^1\Sigma^+$ state, followed by a transition that will decay to the $v' = 0$ state. A one step process may not be appropriate for LiRb, as we have observed the PA drop by nearly 2 orders of magnitude when comparing PA to the $v' = 3$ level and the $v' = 6$ level of the 4(1) potential. In LiCs, such a drop in molecule production via PA was not observed allowing them to produce molecules via PA all the way down the $B^1\Pi$ $v' = 0$ level.

To achieve the goal of having cold, trapped molecules that can be used for quantum computation or quantum simulation experiments the molecules will likely need to be formed in a dipole trap or optical lattice. Because decay via spontaneous emission populates a number of vibrational states as we observed, it is an inefficient method of population transfer in molecules. Many cold molecule groups rely on stimulated Raman adiabatic passage (STIRAP) as a method to coherently transfer molecules to a desired state at high efficiency. STIRAP involves a sequence of counterintuitive pulses. The first couples the desired final state with an intermediate state. As that pulse is turning off, a second pulse couples the initial state to the final state through the intermediate coupling. This is shown schematically in figure 6.3. The result is that the population is coherently transferred to the final state without populating the intermediate state. The reverse and more intuitive method is pump-dump (figure 6.3(b)), but by coupling the initial state to the intermediate state first, the intermediate state is populated. While the second pulse serves to enhance the population in the desired final state via stimulated emission, there are still significant losses due to spontaneous emission. If an adequate one step STIRAP path cannot be found,

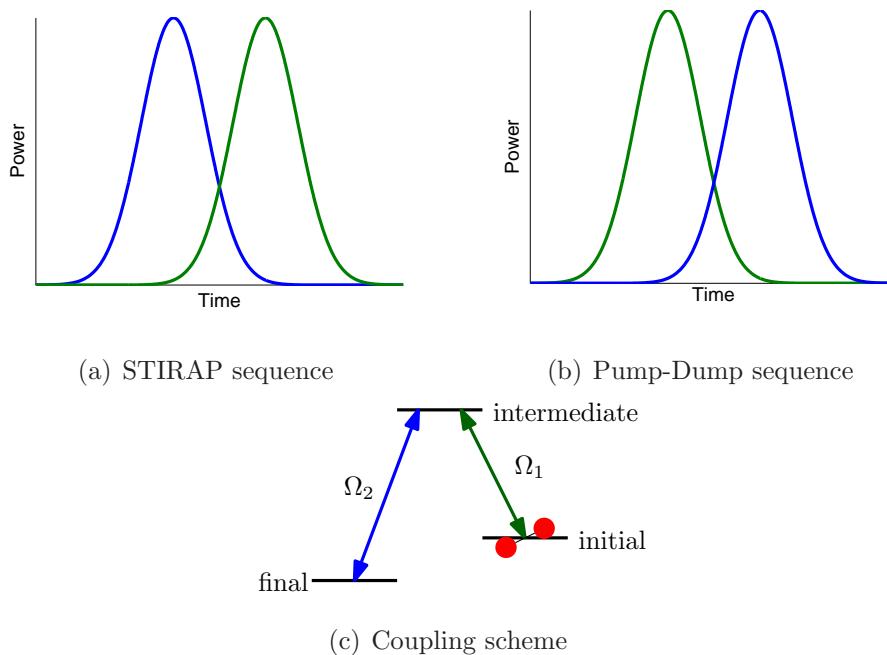


Figure 6.3. Schematic representation of population transfer via STIRAP and Pump-Dump. STIRAP reverses the order of the coupling pulses to avoid and population of the intermediate state.

it is possible to complete a STIRAP transfer in two steps as shown in figure 6.4, as was done in Cs_2 [117]. Note that for two step STIRAP, not all four coupling beams need to be pulsed. Rather only Ω_1 and Ω_4 from figure 6.4 need to be pulsed, while Ω_2 and Ω_3 may be CW. While STIRAP from a scattering state is not yet commonly relied upon, there have been theoretical proposals for STIRAP from the continuum for molecular formation in other species [19].

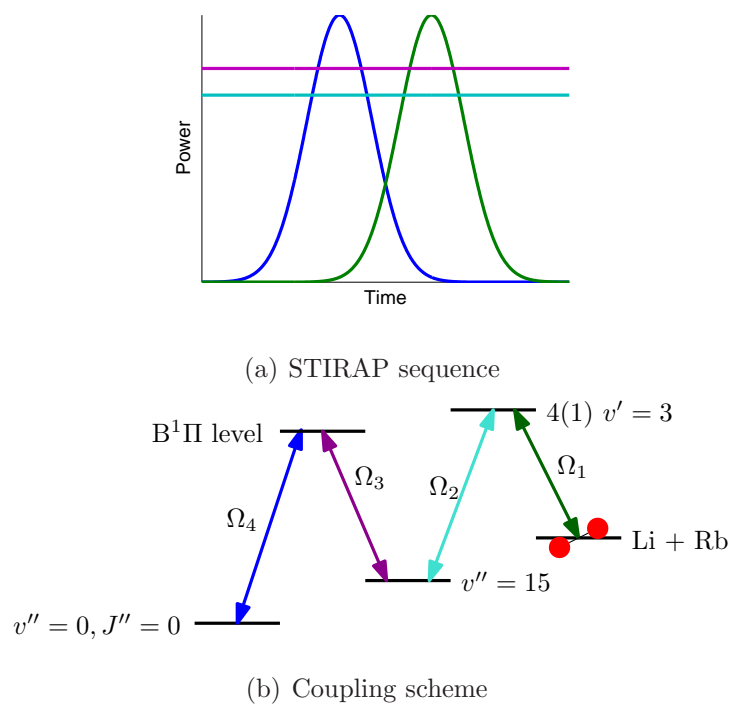


Figure 6.4. Schematic representation of population transfer for LiRb to rovibrational ground state via a two step STIRAP process. Ω_1 and Ω_4 are pulsed while Ω_2 and Ω_3 may be CW.

APPENDICES

A. Electronic Transitions in Diatomic Molecules

In this appendix, we discuss notation and physics general to diatomic molecules required for a discussion of photoassociation, focusing especially on electronic transitions in diatomic molecules. Most of the information comes from reference [112]. Considered separately, the two atoms in a diatomic molecule are completely described by their electronic states. However when they are allowed to interact with each other, new degrees of freedom are introduced, namely the vibrational and rotational motion of the nuclei relative to the center of mass of the system. Whether the atoms are in a bound state (forming a molecule) or a scattering state, these extra degrees of freedom must be considered when defining the quantum state of a molecule and the selection rules for transitions between states.

Any description of electronic transitions in molecules requires knowledge of the various potentials that arise from the sum of Coulomb repulsion between nuclei and the electronic energy which varies with internuclear spacing. The dependence on Coulomb repulsion leads to a potential dependent on internuclear spacing, r . The dependence on electronic energy causes each potential to be different for various electronic states of a molecule. If these potentials have a minimum, they allow for quantized vibrational bound states similar to a harmonic oscillator. Thus each electronic state of a molecule has many vibrational levels denoted by the quantum number v , with the lowest being $v = 0$. The rotational motion of nuclei about the center of mass of the molecule is a component of the total angular momentum, denoted by the quantum number J . J also depends on the angular momentum of electrons and thus the electronic state of the molecule. Whereas non-ionizing transitions between two electronic states in atoms have a fixed energy, a transition between electronic states in a molecule can have many discrete energies because of the various rovibrational states that could be involved.

A.1 Electronic States of Diatomic Molecules

Because diatomic molecules lack the spherical symmetry of atoms, angular momentum vectors that define electronic states are no longer conserved. For instance, the total electronic orbital angular momentum, \vec{L} , will precess around the internuclear axis due to the electric field created by the nuclei and only the component of angular momentum along the axis, M_L is conserved. Like the Stark shift for atoms, this breaks the degeneracy of the different M_L states. Since reversing the electric field does not change the energy of the system, M_L states differing by only a sign are degenerate. Thus, orbital electronic angular momentum is described by the quantum number

$$\Lambda = |M_L| \quad (\text{A.1})$$

Similar to the S, P, D, F, \dots designations for $L = 0, 1, 2, 3, \dots$ in atomic cases, $\Lambda = 0, 1, 2, 3, \dots$ states are designated by $\Sigma, \Pi, \Delta, \Phi, \dots$. Since each nonzero Λ state corresponds to two M_L states, each lambda state is doubly degenerate. Σ states correspond to $M_L = 0$, have a further designation based on symmetry properties. States where the spatial electronic eigenfunction is unchanged upon inversion along the internuclear axis are Σ^+ . States where the sign changes are Σ^- .

Molecular spin is determined by the rules of addition for angular momenta. If two atoms individually have spin S_1 and S_2 then the molecular spin S can be

$$S = S_1 + S_2, S_1 + S_2 - 1, \dots, |S_1 - S_2|. \quad (\text{A.2})$$

As with spectroscopic notation for atoms, a superscript of $2S + 1$ is placed before Λ to express the multiplicity of the state. For example, $^3\Pi$ expresses a state with $S = 1$ and $\Lambda = 1$. While spins are unaffected by electric fields, they will precess around magnetic fields that can arise due to the orbital motion of electrons for states with $\Lambda \neq 0$. Such B-fields are also directed along the internuclear axis and the component of \vec{S} along the axis is also conserved. This component of \vec{S} is labeled Σ when well defined and can take any M_S value.

$$\Sigma = S, S - 1, S - 2, \dots, -S. \quad (\text{A.3})$$

Note for $\Lambda = 0$ molecules, Σ is not well defined as the spin will not be coupled to the internuclear axis when $\Lambda = 0$. Also, the quantum number Σ should not be confused with the notation for the $\Lambda = 0$ molecular state, which is denoted Σ .

The molecular analog to total electronic angular momentum of an atom is $\vec{J}_a = \vec{L} + \vec{S}$. When Σ is well defined, we can define the total about the internuclear axis, $\vec{\Omega}$, the magnitude of which can be found simply by scalar addition of the projections of spin and orbital angular momentum along the axis:

$$\Omega = |\Lambda + \Sigma| \quad (\text{A.4})$$

Just as in atoms, the \vec{L} and \vec{S} are coupled, so that each combination of $\Lambda + \Sigma$ splits into states with $2S + 1$ different energies. Because the coupling is a magnetic field effect, reversal of direction *does* affect spin, $\Lambda + \Sigma$ differing by a sign will have different energies, despite having the same value for Ω . That is, $\Lambda + \Sigma = 1/2$ and $\Lambda + \Sigma = -1/2$ are both $\Omega = 1/2$ states but have different energies. $\Omega = 0$ states have a splitting due to parity, similar to $\Lambda = 0$ states, but this time it is the parity of the whole electronic wavefunction (spatial and spin). They are labeled 0^+ and 0^- , following the same convention as Σ^+ and Σ^- states. If Λ is not well defined, as is the case for large internuclear spacing (see section A.4), electronic states are simply labeled by Ω .

For atoms the complete spectroscopic notation of a state is given by $^{2S+1}L_J$. For molecules, spectroscopic notation takes the form $^{2S+1}\Lambda_{\Lambda+\Sigma}$. Note that the subscript is $\Lambda + \Sigma$ and not Ω because of the ambiguity of Ω . That is the $^4\Pi_{1/2}$ and $^4\Pi_{-1/2}$ states of a molecule are both $\Omega = 1/2$ but are nondegenerate states because of the coupling of \vec{L} and \vec{S} to fields along the internuclear axis. When considering the parity of $\Omega = 0$ states, the notation simply includes the $+$ or $-$ superscript, ie. $^3\Pi_{0+}$ or $^3\Pi_{0-}$.

A.2 Selection Rules for Electronic Transitions in Diatomic Molecules

As this work is concerned with spectra of LiRb, we only present transition rules that apply for heteronuclear molecules of different charges, as there are additional

transition rules for homonuclear dimers. In transitions between molecular electronic states, angular momentum selection rules for dipole radiation apply. That is:

$$\Delta J = 0, \pm 1, J = 0 \leftrightarrow J = 0 \quad (\text{A.5})$$

where J is the total angular momentum of the molecule quantum number. \vec{J} is composed of \vec{L} , \vec{S} and the rotation of nuclei about the center of mass, \vec{R} . Thus

$$\vec{J} = \vec{L} + \vec{S} + \vec{R} \quad (\text{A.6})$$

and the quantum number J can take values

$$J = \Omega, \Omega + 1, \Omega + 2, \dots \quad (\text{A.7})$$

The other selection rule

$$\Delta M_J = 0, \pm 1 \quad (\text{A.8})$$

where M_J is the projection of \vec{J} along a quantization axis. From this it can be deduced that the selection rules for Λ and Ω are

$$\Delta \Lambda = 0, \pm 1, \Delta \Omega = 0, \pm 1 \quad (\text{A.9})$$

There is an additional restriction that

$$\Delta J \neq 0 \text{ for } \Omega = 0 \leftrightarrow \Omega = 0. \quad (\text{A.10})$$

In general the spin of a molecule cannot be changed in an electronic transition. So that we also have as a selection rule

$$\Delta S = 0. \quad (\text{A.11})$$

However perturbations can cause some vibrational states to have both triplet and singlet components due to perturbations. Thus, (A.11) does not strictly hold in all cases. Additionally, if Σ is a good quantum number for both the initial and final state of a transition we have that

$$\Delta \Sigma = 0. \quad (\text{A.12})$$

Transitions between $\Lambda = 0$ states have an additional selection rule. Because the transition moment $\Delta\Lambda = 0$ lies along the internuclear axis, the moment vanishes if the initial and final states are of opposite parity. Thus:

$$\Sigma^+ \leftrightarrow \Sigma^+, \Sigma^- \leftrightarrow \Sigma^-, \Sigma^+ \leftrightarrow \Sigma^-. \quad (\text{A.13})$$

. In cases where Λ is not a good quantum number, but Ω is, the analog

$$\Omega^+ \leftrightarrow \Omega^+, \Omega^- \leftrightarrow \Omega^-, \Omega^+ \leftrightarrow \Omega^- \quad (\text{A.14})$$

applies.

A.2.1 Labeling of Electronic States

Labeling of electronic states can be confusing, as many electronic states have the same angular momentum quantum numbers, but molecules lack a quantum number similar to the principle quantum number in atoms to distinguish among them. To delineate potentials, it is often useful to consider the separate atomic states when the internuclear spacing is large. Each molecular potential is asymptotic to two atomic states at the dissociation energy, such as $\text{Li } 2S_{1/2} + \text{Rb } 5S_{1/2}$ in the ground state or $\text{Li } 2S_{1/2} + \text{Rb } 5P_{3/2}$ for a possible excited states. The system for labeling molecular states does not indicate which atomic states it corresponds to at dissociation, which must often be specified.

An electronic molecular state can be described by its spectroscopic label

$$^{2S+1}\Lambda_{\Lambda+\Sigma}$$

along with the asymptotic atomic states it corresponds to as a substitute for the principle quantum number. However, for brevity one of the two following naming conventions is usually adopted. The traditional convention is that the state with the lowest electronic energy state (measured at R_{eq} , the equilibrium internuclear separation) is labeled X and each potential above it with the same degeneracy is labeled A, B, C, ... in order of increasing energies. States with different degeneracy

are labeled a, b, c, . . . , again in order of increasing energies. For LiRb, $X^1\Sigma^+$ has the lowest potential depth and possible excited singlet states are $A^1\Sigma^+$ and $B^1\Pi$. The lowest triplet state is the ground state $a^3\Sigma^+$ and excited states are $b^3\Pi$ and $c^3\Sigma^+$. An alternate method is simply to label states $(1)^1\Sigma^+$, $(2)^1\Sigma^+$, . . . , $(1)^3\Sigma^+$, $(2)^3\Sigma^+$, . . . , $(1)^1\Pi$, $(2)^1\Pi$, etc. with the number on the left increasing with asymptotic energy. Since authors often mix notations, it is best to simply provide a plot with the potential curves being referred to labeled appropriately.

For molecules where Λ is not a good quantum number (see section A.4) potentials are labeled $n(\Omega)$ to refer to the n th state of quantum number Ω as energy increases. For example, in LiRb the three potentials asymptotic to the ground $\text{Li } 2S_{1/2} + \text{Rb } 5S_{1/2}$ will be labeled $1(0^+)$, $1(0^-)$ and $1(1)$. The first excited atomic asymptote will be the $\text{Li } 2S_{1/2} + \text{Rb } 5P_{1/2}$, which has three potentials labeled $2(0^+)$, $2(0^-)$, and $2(1)$. The next asymptote corresponds to $\text{Li } 2S_{1/2} + \text{Rb } 5P_{3/2}$ which has 5 potentials: $3(0^+)$, $3(0^-)$, $3(1)$, $4(1)$, and $1(2)$. The distinction between $3(1)$ and $4(1)$ is that the $3(1)$ potential has a bigger slope so that when looking at potentials at the same large R internuclear spacing the $3(1)$ potential has lower energy than the $4(1)$ potential to keep the numbering system straight.

A.3 Vibrational Levels in Diatomic Molecules

As noted earlier the electronic and nuclear interactions create the potentials that allow for bound molecules. The motion of nuclei along the internuclear axis of the molecule is described by the vibrational state of the molecule. If the total energy of the molecule lies close to the bottom of a potential, it may be modeled as a quadratic harmonic oscillator with equally spaced energy levels. As the total energy of the molecule increases, the vibrational states become less harmonic. Higher order terms may be added to the potential to account for anharmonicity. However, a close approximation for molecular potentials for all bound energies was proposed by Morse:

$$U(r - r_e) = D_e \left(1 - e^{-\beta(r-r_e)}\right)^2 \quad (\text{A.15})$$

where D_e is the dissociation energy, r_e is the equilibrium atomic separation, and β is a parameter related to the vibrational frequency. The Schrödinger equation can be solved exactly for this potential. The energy levels in terms of wavenumbers $G(v) = E(v)/hc$ are

$$G(v) = \beta \sqrt{\frac{D_e h}{2\pi^2 c \mu}} (v + 1/2) - \frac{h\beta}{c 8\pi^2 \mu} (v + 1/2)^2 \quad (\text{A.16})$$

where v is the vibrational quantum number and μ is the reduced mass of the molecule. An important distinction between the solutions for the Morse potential and the harmonic oscillator potential is the allowed transitions. Since the actual potential is not symmetric, we can think of each v state derived from the Morse potential as a superposition of many harmonic oscillator v states so there is no restriction of $\Delta v = \pm 1$ on molecular transitions between vibrational levels.

A.3.1 Consideration of Vibrational Levels in Electronic Transitions

The Franck-Condon principle describes how vibrational states factor into an electronic transition in a molecule. As in atomic transitions, the electron is assumed to change states instantaneously. The implication is that the position and momentum of the nuclei remain unchanged during the transition. The strength of an electronic transition in a molecule is affected by the initial and final vibrational states involved. Transitions where the initial and final vibrational states have similar classical turning points are stronger because an electron can undergo a transition while the nuclei maintain position and momentum at the turning point. Away from the classical turning points, the momentum would have to abruptly change unless the ground state potential was nearly identical to the excited state potential. While this classical explanation qualitatively explains how electrons behave during transitions, a rigorous quantum mechanical explanation is necessary to explain the precise details since position and momentum cannot be known simultaneously.

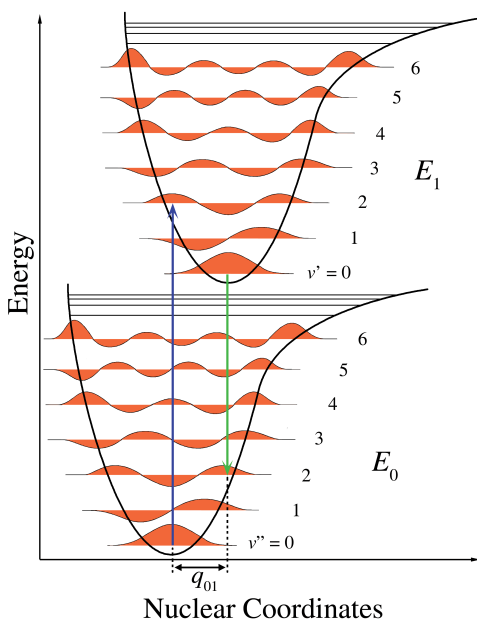


Figure A.1. A schematic representation of how Franck-Condon factors affect electronic transitions. The strongest transitions are those where there is strong overlap of Ψ_v in both the excited and ground state. Usually this corresponds to a shared classical turning point in the molecular potential. Figure adapted from [118].

The quantum formulation of an electronic transition is, again, similar to that of atoms and depends on the molecule's transition dipole moment between initial state ψ' and final state ψ'' ,

$$R = \langle \psi' | \vec{M} | \psi'' \rangle = \int \psi'^* \vec{M} \psi'' d\tau \quad (\text{A.17})$$

The wavefunctions of diatomic molecules can be decomposed into electronic, vibrational, and rotational parts.

$$\psi = \psi_e \psi_v \psi_r \quad (\text{A.18})$$

The dipole moment does not act on the rotational part of the wavefunction, so it may be ignored. The dipole moment can be separated into the electronic and nuclear moments $\vec{M}_e + \vec{M}_n$. The integral can be rewritten

$$R = \int \vec{M}_e \psi_e'^* \psi_e'' \psi_v'^* \psi_v'' d\tau + \int \vec{M}_n \psi_e'^* \psi_e'' \psi_v'^* \psi_v'' d\tau \quad (\text{A.19})$$

The second term is ignored because the nuclear dipole moment operator only acts on the vibrational component and the orthogonal electronic wavefunctions will integrate to zero. The first term can be rewritten

$$R = \int \vec{M}_e \psi_e' \psi_e'' \int \psi_v' \psi_v'' d\tau \quad (\text{A.20})$$

The first integral is the electronic transition moment, while the second vibrational overlap integral is called the Franck-Condon factor (FCF). Often denoted

$$F = \int \psi_v' \psi_v'' dr \quad (\text{A.21})$$

It can be thought of as probability of decaying to a given vibrational level from a given excited state. Note that ψ_v' and ψ_v'' arise from different molecular potentials, and are part of different orthonormal basis sets. That is, there is no orthogonality condition between ψ_v' and ψ_v'' , meaning no selection rules for v in electronic transitions. The quantum formulation explains why transitions are weaker in molecules than atoms because the electronic transition strength, $\int \vec{M}_e \psi_e' \psi_e''$, is now spread across many vibrational levels with favorable FCFs. The quantum mechanical formulation of the Franck-Condon principle is easily extended beyond electric dipole transitions and remains the same for higher order transition moments. For a given transition, usually many values of v produce negligible FCFs. The semi-classical picture can be used to guess at which vibrational levels will have non-negligible Frank-Condon overlap as ψ_v will be in phase and have appreciable amplitude at classical turning points, if they have a classical turning point in common. The connection between classical turning points and wavefunction overlap as pertaining to FCFs is schematically shown in figure A.1.

A.4 Hund's Coupling Cases

In discussion of molecules to this point, it has been assumed that orbital angular momentum and electronic spin are coupled to the internuclear axis of the molecule, causing them to precess around it. In this case, Λ and Σ (for $\Lambda \neq 0$) are well defined.

At large internuclear spacing, where the molecule is closer to two separate atoms, \vec{L} and \vec{S} interact more strongly with each other than the internuclear axis. In this case Λ and Σ are no longer well defined, but the sum $\vec{J}_a = \vec{L} + \vec{S}$ will still precess around the internuclear axis and Ω is defined as the component of \vec{J}_a along the internuclear axis. The various ways in which angular momenta couple with each other are called Hund's cases. When \vec{S} is coupled to \vec{L} , which is in turn coupled to the internuclear axis, it is called Hund's case (a). When \vec{S} is not coupled or only weakly coupled to \vec{L} , such as the $\Lambda = 0$ case and Ω is not defined it is called Hund's case (b). \vec{S} will be slightly coupled to \vec{R} due to a small magnetic moment arising from molecular rotation. Hund's case (b) situations where $\Lambda \neq 0$ generally occurs only for very light molecules. Thus Hund's case (b) likely only applies for $\Lambda = 0$ states of LiRb where $S \neq 0$. ($^1\Sigma$ states can be treated as case (a), because if $S = 0$, the projection of $\Sigma = 0$ is well defined.) When \vec{L} and \vec{S} are coupled, but \vec{L} is no longer strongly coupled to the internuclear axis, it is called Hund's case (c). In Hund's case (c) situations, Λ and Σ is no longer a good quantum numbers and the electronic state of the molecule is given by Ω because the previously described notation does not apply without a defined Λ . When molecules fall under Hund's case (c) the potentials describing their interaction are simply labeled as $n(\Omega)$ for the n th electronic state with a particular Ω quantum number. The $\Omega = 0$ state may either be 0^+ or 0^- depending on the parity of the electronic wavefunction. There are additional Hund's coupling cases (d) and (e), which are not addressed here.

Table A.1 shows when to apply each case, and what the good quantum numbers are for each case. The main importance of Hund's coupling cases, is how they affect electronic transitions. For example, a transitions from a $^3\Sigma$ can go to a $^3\Pi$ state with any Ω because while Σ and Ω are good quantum numbers for the $^3\Pi$, they are not for the $^3\Sigma$ state so there are is no valid selection rule regarding those quantum numbers. Meaning that the spin-orbit splitting in the $^3\Pi$ state will be observed in spectra for this transition. However, a transition from a $^3\Sigma$ to a $^3\Sigma$ will be constrained by the fact that $\Delta\Sigma = 0$, meaning the initial and final values for Σ and Ω will be the same

and no spin-orbit interaction will be observed for this kind of transition. It should be noted however that most LiRb measurements begin with molecules in one of the two electronic ground states with $\Lambda = 0$, either the $a^3\Sigma^+$ or the $X^1\Sigma^+$.

Table A.1

A summary of when Hund's coupling cases apply and what the quantum numbers are good for each case. It should be noted that the effect of molecular rotation is ignored. For cold molecule experiments, this is a safe assumption. Also note that J is always a good quantum number.

Hund's Case	Applicability	Good Quantum numbers
(a)	small internuclear separation $\Lambda \neq 0$ or $S = 0$	$\Lambda, S, \Sigma, \Omega$
(b)	small internuclear separation $\Lambda = 0$ and $S \neq 0$	Λ, S
(c)	large internuclear separation	Ω

While molecules in a Hund's coupling case (a) state can transition to one in a Hund's coupling case (b) state, that is not the case for Hund's coupling case (c). Molecules in a case (c) usually have large internuclear separation. The Franck-Condon principle stipulates that separation will be unchanged during a transition — a vertical transition on an energy versus separation plot. So if a molecule begins in a Hund's case (c) state, it will end in a Hund's case (c) state and likewise for (a) states. This may seem counterintuitive, because one might imagine that for a given vibrational state, it could follow Hund's case (a) or (b) transition rules at close spacings and follow Hund's case (c) at large internuclear spacings and two different sets of selection rules should not govern the same molecular state. The resolution is that the selection rules do not contradict each other because when a molecule enters a regime where a quantum number is no longer good, it can be thought of as an admixture of states described by the now “bad” quantum numbers.

Molecular states that would fall under Hund's case (c) are mostly weakly bound states where the vibrational wave function, $\psi_v(r)$, extends to large internuclear separation. Semi-classically, the molecules will spend more time near the outer turning point than the inner because dV/dr is much smaller. Thus $\psi_v(r)$ has a much larger node at the outer turning point than the inner turning point. A molecule in an excited $\Omega = 1$ could decay to any of the $1(0^+)$, $1(0^-)$, or $1(1)$ potentials. There is a correlation between the long range potentials described by Hund's case (c) and the closer range potentials described by Hund's case (a). If that excited $\Omega = 1$ state correlates to a $^1\Pi$ state, that would indicate that a LiRb molecule in the $B^1\Pi$ states with a high v could decay to either the $X^1\Sigma$ (correlating to the $1(0^+)$) or the $a^3\Sigma^+$ (correlating to the $1(0^-)$ or $1(1)$ state), which seems a violation of the selection rules. The key is that for the high v states Λ is not actually a good quantum number anymore, so selection rules pertaining to Λ no longer apply. We assign them to the $B^1\Pi$ potential by convention because the short range part of the potential has to connect to the long range somehow. Since Λ and S (and thus Σ) are not good quantum numbers for high v states, the electronic part of these states' wavefunction is actually an admixture of Hund's case (a) or (b) states. Roughly speaking, the electronic wavefunction for high v states can be thought of as an admixture of states with different orbital angular momentum and spin, which are not well defined. Thus states, with high v can have both singlet and triplet character. Whether or not to use Hund's case (c) selections for a transition involving a high v state, requires knowledge of both states. If $\psi_v(r)$ is long range for both states, it likely undergoing a transition at a large internuclear distance and Hund's case (c) should be used. If $\psi_v(r)$ for one state is long range, but is short range for the second state, then Hund's case (a) or (b) selection rules should apply, because the transition could only occur in a region where the wavefunction overlap contributes to the Franck-Condon factor. Table A.2 summarizes the transition rules for heteronuclear molecules.

Table A.2

A summary of the selection rules that apply for molecules that undergo transitions. The top row the initial Hund's couple case of the initial and final state for a given transition, as the cases have different selection rules. There selection rules for transitions between other Hund's cases, as well as other quantum numbers used to describe molecules not listed here.

Rule	(a) \leftrightarrow (b)	(a) \leftrightarrow (a)	(c) \leftrightarrow (c)
J	$\Delta J = 0, \pm 1; J = 0 \nrightarrow J = 0$		
symmetry	$+ \leftrightarrow +, - \leftrightarrow -, + \leftrightarrow -$		
Λ	$\Delta \Lambda = 0, \pm 1$	N/A	
S	$\Delta S = 0$	N/A	
Σ	$\Delta \Sigma = 0$	N/A	
Ω	$\Delta \Omega = 0, \pm 1$	N/A	$\Delta \Omega = 0, \pm 1$

B. Observed and Calculated LiRb transitions

This appendix consists of tables of transitions from the $X^1\Sigma^+$ state to excited electronic states. Tables B.1 and B.2 list the possible progressions that might be seen in a one color REMPI process for $X^1\Sigma^+ \rightarrow D^1\Pi$ and $X^1\Sigma^+ \rightarrow B^1\Pi$ transitions. The REMPI photon energy, $\hbar\omega$, is reported in cm^{-1} in all tables. Throughout the appendix, levels which have not been previously observed are listed in **red**. The vibrational number v'' is always assumed to belong to the $X^1\Sigma^+$, which have been observed up to $v'' = 45$, and are thus all listed in black as only transitions up to $v'' = 26$ are considered. Energies of transitions to unobserved states are also listed in **red** to indicate they are calculated values that have not been directly measured, as the transitions in black have been.

Transitions to the $C^1\Sigma^+$ are not included, as there have not been any direct observations $C^1\Sigma^+$. The PEC used to calculate $C^1\Sigma^+$ levels is based only on its perturbative effects on the $B^1\Pi$. Because of this, only a small region of the $C^1\Sigma^+$ can be assumed to be accurate, making it more difficult to make definitive assignments, especially for higher v' states. There are just shy of 500 expected $X^1\Sigma^+ \rightarrow C^1\Sigma^+$ transitions that satisfy the conditions from section 4.5, many of which are certain to be close to $B^1\Pi$ or $D^1\Pi$ transitions. Some of the unassigned lines in the spectra may be attributable to $C^1\Sigma^+$ transitions, but considering the number lines already assigned to $B^1\Pi$ or $D^1\Pi$ transitions, it is left to future work to look for $C^1\Sigma^+$ lines among the spectra.

Tables B.3 and B.4 list all the $B^1\Pi$ and $D^1\Pi$ transitions from tables B.1 and B.2 in order of the transition energy. This is a useful way of organizing the spectra to see which lines are close in energy, which may cause an ambiguity in assignment. In these tables, the first column has a “B” or “D” as a shorthand method of labelling

the potential to which v' belongs. The second and third columns are the vibrational numbers v'' and v' respectively, while the fourth column gives the transition energy.

Tables B.5-B.9 lists all the lines observed in the spectra. Possible lines that are weak or are have poor signal to noise are in *italics*. Some weak lines that are not strongly visible above noise are nonetheless included because they fit into an established progression. The first column gives the energy of the line from the REMPI spectra. The second column gives the assignment for the line in the format $v'' \rightarrow v'$ B/D ($\hbar\omega$), where be B/D/C is again shorthand for the electronic potential and $\hbar\omega$ is the previously measured energy of the transition, or calculated energy for previously unobserved levels listed in red.

The assignments are not simply based on how closely the measured energy of the line matches the expected energy, but also includes factors such as if it is part of an apparent progression. Simply matching the measured energy is a poor method of assignment primarily because some of the lines are quite broad and do not have a simple Gaussian or Lorentzian line shape where the middle of the peak can simply be taken as the energy. Observed lines are actually superpositions of several rovibrational lines that are unresolved in REMPI spectroscopy. The listed transition energies are between the energy between the $|v'', J = 0 \rangle$ and $|v', J = 0 \rangle$, rovibrational levels. (Note that $J = 0 \rightarrow J = 0$ is not actually allowed.) Measuring rotational levels usually involves higher resolution depletion spectroscopy, but rotational level considerations can affect line shape in REMPI spectroscopy. Also, transitions of similar energies can merge into what looks like a single line. Sometimes there is an asymmetry of broad line that has a higher intensity region and a lower intensity region. A possible explanation for lines like this is that a stronger and weaker transition are not completely resolvable, but are still partially distinguishable.

The third column in tables B.5-B.9 lists transitions near the line, but that are not assigned to the line. They have been ruled out for a variety of reasons including not belonging to an apparent progression, simply being too far away from the measured energy of the transition, a lack of confidence in the calculated position of previously

unobserved lines, or any combination of these factors. When assigning lines to levels that have not been previously observed, we assign some lines that deviate a bit from the calculated position because there is strong case that the progression is present and it is quite possible that the PEC used to calculate the line position should be further refined with new measurements. There are some $C^1\Sigma^+$ transitions included in this column. Future work may show some lines better assigned to these $C^1\Sigma^+$ transitions, we refrain from doing so without greater knowledge of the $C^1\Sigma^+$ potential.

Finally, table B.10 summarizes the progressions seen based on the assignments made to the observed lines. The assignments are listed as $v'' \rightarrow v'$ through either the $D^1\Pi$ or $B^1\Pi$ potentials. Assignments that are possibly ambiguous because of multiple possible transition assignments to a single line are noted with an asterisk (*).

Table B.1
Possible one color REMPI transitions sorted by progression (Part I).

v''	v'	$\hbar\omega$	$X^1\Sigma^+ \rightarrow D^1\Pi$ transitions																	
6	0	17928.7	11	8	17934.4	14	5	17132.6	16	5	16816.6	17	16	17605.8	19	13	17106.5	21	15	16957.6
7	0	17749.5	12	0	16889.6	14	6	17238.5	16	6	16922.5	17	17	17660.6	19	14	17178.8	21	16	17018.5
7	1	17867.9	12	1	17008.0	14	7	17341.4	16	7	17025.4	17	18	17708.5	19	15	17245.5	21	17	17073.3
7	2	17984.3	12	2	17124.4	14	8	17440.8	16	8	17124.9	17	19	17746.9	19	16	17306.4	21	18	17121.1
8	0	17572.6	12	3	17238.5	14	9	17536.6	16	9	17220.6	17	20	17770.5	19	17	17361.1	21	19	17159.6
8	1	17691.0	12	4	17350.1	14	10	17628.2	16	10	17312.3	17	21	17783.6	19	18	17409.0	21	20	17183.1
8	2	17807.4	12	5	17459.0	14	11	17715.6	16	11	17399.6	18	5	16511.5	19	19	17447.5	21	21	17196.2
8	3	17921.5	12	6	17565.0	14	12	17798.2	16	12	17482.2	18	6	16617.4	19	20	17471.0	22	10	16431.6
9	0	17398.2	12	7	17667.8	14	13	17875.9	16	13	17559.9	18	7	16720.3	19	21	17484.1	22	11	16519.0
9	1	17516.6	12	8	17767.3	14	14	17948.2	16	14	17632.2	18	8	16819.8	20	7	16426.6	22	12	16601.6
9	2	17633.0	12	9	17863.0	15	1	16522.2	16	15	17698.9	18	9	16915.5	20	8	16526.0	22	13	16679.3
9	3	17747.1	12	10	17954.7	15	2	16638.6	16	16	17759.8	18	10	17007.2	20	9	16621.8	22	14	16751.6
9	4	17858.7	13	0	16725.0	15	3	16752.7	16	17	17814.5	18	11	17094.5	20	10	16713.4	22	15	16818.3
9	5	17967.6	13	1	16843.5	15	4	16864.3	16	18	17862.4	18	12	17177.2	20	11	16800.8	22	16	16879.1
10	0	17226.2	13	2	16959.9	15	5	16973.2	16	19	17900.9	18	13	17254.8	20	12	16883.4	22	17	16933.9
10	1	17344.6	13	3	17074.0	15	6	17079.2	16	20	17924.4	18	14	17327.2	20	13	16961.1	22	18	16981.8
10	2	17461.0	13	4	17185.6	15	7	17182.0	16	21	17937.5	18	15	17393.8	20	14	17033.4	22	19	17020.2
10	3	17575.1	13	5	17294.5	15	8	17281.5	17	3	16442.1	18	16	17454.7	20	15	17100.1	22	20	17043.8
10	4	17686.7	13	6	17400.5	15	9	17377.2	17	4	16553.8	18	17	17509.5	20	16	17160.9	22	21	17056.8
10	5	17795.6	13	7	17503.3	15	10	17468.9	17	5	16662.6	18	18	17557.3	20	17	17215.7	23	12	16465.4
10	6	17901.6	13	8	17602.8	15	11	17556.2	17	6	16768.6	18	19	17595.8	20	18	17263.6	23	13	16543.0
10	7	18004.4	13	9	17698.5	15	12	17638.9	17	7	16871.5	18	20	17619.3	20	19	17302.1	23	14	16615.4
11	0	17056.6	13	10	17790.2	15	13	17716.6	17	8	16970.9	18	21	17632.4	20	20	17325.6	23	15	16682.0
11	1	17175.0	13	11	17877.5	15	14	17788.9	17	9	17066.6	19	6	16469.1	20	21	17338.7	23	16	16742.9
11	2	17291.4	13	12	17960.2	15	15	17855.5	17	10	17158.3	19	7	16572.0	21	9	16479.3	23	17	16797.7
11	3	17405.5	14	0	16563.1	15	16	17916.4	17	11	17245.7	19	8	16671.5	21	10	16571.0	23	18	16845.5
11	4	17517.2	14	1	16681.5	15	17	17971.2	17	12	17328.3	19	9	16767.2	21	11	16658.3	23	19	16884.0
11	5	17626.1	14	2	16797.9	16	2	16481.9	17	13	17406.0	19	10	16858.9	21	12	16741.0	23	20	16907.5
11	6	17732.0	14	3	16912.0	16	3	16596.0	17	14	17478.3	19	11	16946.2	21	13	16818.7	23	21	16920.6
11	7	17834.9	14	4	17023.7	16	4	16707.7	17	15	17545.0	19	12	17028.8	21	14	16891.0	24	14	16482.3

Table B.2
Possible one color REMPI transitions sorted by progression (Part II).

v''	v'	$\hbar\omega$	$X^1\Sigma^+ \rightarrow D^1\Pi$ transitions (cont.)														
24	15	16549.0	24	18	16712.5	24	21	16787.6	25	18	16582.8	25	21	16657.9	26	20	16518.5
24	16	16609.8	24	19	16751.0	25	16	16480.1	25	19	16621.2	26	18	16456.5	26	21	16531.6
24	17	16664.6	24	20	16774.5	25	17	16534.9	25	20	16644.8	26	19	16494.9			
v''	v'	$\hbar\omega$	$X^1\Sigma^+ \rightarrow B^1\Pi$ transitions														
0	7	17741.3	3	17	17720.3	4	30	17866.0	5	35	17704.1	7	24	17222.9	8	35	17166.5
0	8	17812.9	3	18	17760.1	4	31	17873.9	5	36	17704.8	7	25	17246.0	8	36	17167.2
0	9	17879.9	3	19	17797.8	4	32	17879.7	6	17	17168.7	7	26	17266.4	9	24	16871.6
0	10	17942.7	3	20	17833.5	4	33	17883.9	6	18	17208.5	7	27	17284.0	9	25	16894.7
1	8	17619.9	3	21	17867.1	4	34	17886.5	6	19	17246.2	7	28	17298.9	9	26	16915.1
1	9	17686.9	3	22	17898.5	4	35	17888.0	6	20	17281.9	7	29	17311.3	9	27	16932.7
1	10	17749.7	3	23	17927.5	4	36	17888.7	6	21	17315.5	7	30	17321.4	9	28	16947.7
1	11	17808.8	3	24	17953.7	5	15	17264.0	6	22	17346.9	7	31	17329.2	9	29	16960.1
1	12	17864.5	3	25	17976.8	5	16	17308.3	6	23	17375.9	7	32	17335.1	9	30	16970.1
1	13	17916.9	3	26	17997.2	5	17	17350.3	6	24	17402.1	7	33	17339.2	9	31	16977.9
1	14	17966.5	4	13	17351.6	5	18	17390.1	6	25	17425.2	7	34	17341.9	9	32	16983.8
2	10	17559.0	4	14	17401.1	5	19	17427.8	6	26	17445.6	7	35	17343.4	9	33	16987.9
2	11	17618.1	4	15	17447.9	5	20	17463.4	6	27	17463.2	7	36	17344.0	9	34	16990.6
2	12	17673.7	4	16	17492.2	5	21	17497.0	6	28	17478.1	8	21	16959.4	9	35	16992.1
2	13	17726.2	4	17	17534.2	5	22	17528.4	6	29	17490.6	8	22	16990.8	9	36	16992.7
2	14	17775.7	4	18	17573.9	5	23	17557.5	6	30	17500.6	8	23	17019.9	10	29	16788.1
2	15	17822.5	4	19	17611.7	5	24	17583.6	6	31	17508.4	8	24	17046.0	10	30	16798.1
2	16	17866.8	4	20	17647.3	5	25	17606.8	6	32	17514.3	8	25	17069.2	10	31	16805.9
2	17	17908.8	4	21	17680.9	5	26	17627.2	6	33	17518.4	8	26	17089.5	10	32	16811.8
2	18	17948.6	4	22	17712.3	5	27	17644.7	6	34	17521.1	8	27	17107.1	10	33	16815.9
2	19	17986.3	4	23	17741.4	5	28	17659.7	6	35	17522.6	8	28	17122.1	10	34	16818.6
3	11	17429.6	4	24	17767.5	5	29	17672.1	6	36	17523.2	8	29	17134.5	10	35	16820.1
3	12	17485.3	4	25	17790.6	5	30	17682.1	7	19	17067.0	8	30	17144.5	10	36	16820.7
3	13	17537.7	4	26	17811.0	5	31	17690.0	7	20	17102.7	8	31	17152.4			
3	14	17587.3	4	27	17828.6	5	32	17695.9	7	21	17136.3	8	32	17158.2			
3	15	17634.1	4	28	17843.6	5	33	17700.0	7	22	17167.7	8	33	17162.4			
3	16	17678.4	4	29	17856.0	5	34	17702.6	7	23	17196.7	8	34	17165.0			

Table B.3
Possible one color REMPI transitions sorted by energy (Part I).

D 20 7	16426.6	D 15 2	16638.6	D 16 5	16816.6	B 9 29	16960.1	B 8 26	17089.5	B 7 23	17196.7
D 22 10	16431.6	D 25 20	16644.8	D 22 15	16818.3	D 20 13	16961.1	D 18 11	17094.5	B 6 18	17208.5
D 17 3	16442.1	D 25 21	16657.9	B 10 34	16818.6	B 9 30	16970.1	D 20 15	17100.1	D 20 17	17215.7
D 26 18	16456.5	D 21 11	16658.3	D 21 13	16818.7	D 17 8	16970.9	B 7 20	17102.7	D 16 9	17220.6
D 23 12	16465.4	D 17 5	16662.6	D 18 8	16819.8	D 15 5	16973.2	D 19 13	17106.5	B 7 24	17222.9
D 19 6	16469.1	D 24 17	16664.6	B 10 35	16820.1	B 9 31	16977.9	B 8 27	17107.1	D 10 0	17226.2
D 21 9	16479.3	D 19 8	16671.5	B 10 36	16820.7	D 22 18	16981.8	D 21 18	17121.1	D 12 3	17238.5
D 25 16	16480.1	D 22 13	16679.3	D 13 1	16843.5	B 9 32	16983.8	B 8 28	17122.1	D 14 6	17238.5
D 16 2	16481.9	D 14 1	16681.5	D 23 18	16845.5	B 9 33	16987.9	D 12 2	17124.4	D 19 15	17245.5
D 24 14	16482.3	D 23 15	16682.0	D 19 10	16858.9	B 9 34	16990.6	D 16 8	17124.9	D 17 11	17245.7
D 26 19	16494.9	D 16 4	16707.7	D 15 4	16864.3	B 8 22	16990.8	D 14 5	17132.6	B 7 25	17246.0
D 18 5	16511.5	D 24 18	16712.5	D 17 7	16871.5	B 9 35	16992.1	B 8 29	17134.5	B 6 19	17246.2
D 26 20	16518.5	D 20 10	16713.4	B 9 24	16871.6	B 9 36	16992.7	B 7 21	17136.3	D 18 13	17254.8
D 22 11	16519.0	D 18 7	16720.3	D 22 16	16879.1	D 18 10	17007.2	B 8 30	17144.5	D 20 18	17263.6
D 15 1	16522.2	D 13 0	16725.0	D 20 12	16883.4	D 12 1	17008.0	B 8 31	17152.4	B 5 15	17264.0
D 20 8	16526.0	D 21 12	16741.0	D 23 19	16884.0	D 21 16	17018.5	B 8 32	17158.2	B 7 26	17266.4
D 26 21	16531.6	D 23 16	16742.9	D 12 0	16889.6	B 8 23	17019.9	D 17 10	17158.3	D 15 8	17281.5
D 25 17	16534.9	D 24 19	16751.0	D 21 14	16891.0	D 22 19	17020.2	D 21 19	17159.6	B 6 20	17281.9
D 23 13	16543.0	D 22 14	16751.6	B 9 25	16894.7	D 14 4	17023.7	D 20 16	17160.9	B 7 27	17284.0
D 24 15	16549.0	D 15 3	16752.7	D 23 20	16907.5	D 16 7	17025.4	B 8 33	17162.4	D 11 2	17291.4
D 17 4	16553.8	D 19 9	16767.2	D 14 3	16912.0	D 19 12	17028.8	B 8 34	17165.0	D 13 5	17294.5
D 14 0	16563.1	D 17 6	16768.6	B 9 26	16915.1	D 20 14	17033.4	B 8 35	17166.5	B 7 28	17298.9
D 21 10	16571.0	D 24 20	16774.5	D 18 9	16915.5	D 22 20	17043.8	B 8 36	17167.2	D 20 19	17302.1
D 19 7	16572.0	D 24 21	16787.6	D 23 21	16920.6	B 8 24	17046.0	B 7 22	17167.7	D 19 16	17306.4
D 25 18	16582.8	B 10 29	16788.1	D 16 6	16922.5	D 11 0	17056.6	B 6 17	17168.7	B 5 16	17308.3
D 16 3	16596.0	D 23 17	16797.7	B 9 27	16932.7	D 22 21	17056.8	D 11 1	17175.0	B 7 29	17311.3
D 22 12	16601.6	D 14 2	16797.9	D 22 17	16933.9	D 17 9	17066.6	D 18 12	17177.2	D 16 10	17312.3
D 24 16	16609.8	B 10 30	16798.1	D 19 11	16946.2	B 7 19	17067.0	D 19 14	17178.8	B 6 21	17315.5
D 23 14	16615.4	D 20 11	16800.8	B 9 28	16947.7	B 8 25	17069.2	D 15 7	17182.0	B 7 30	17321.4
D 18 6	16617.4	B 10 31	16805.9	D 21 15	16957.6	D 21 17	17073.3	D 21 20	17183.1	D 20 20	17325.6
D 25 19	16621.2	B 10 32	16811.8	B 8 21	16959.4	D 13 3	17074.0	D 13 4	17185.6	D 18 14	17327.2
D 20 9	16621.8	B 10 33	16815.9	D 13 2	16959.9	D 15 6	17079.2	D 21 21	17196.2	D 17 12	17328.3

Table B.4
Possible one color REMPI transitions sorted by energy (Part II).

B 7	31	17329.2	B 4	15	17447.9	D 15	11	17556.2	B 5	29	17672.1	B 4	24	17767.5	D 13	11	17877.5
B 7	32	17335.1	D 18	16	17454.7	D 18	18	17557.3	B 2	12	17673.7	D 17	20	17770.5	B 4	32	17879.7
D 20	21	17338.7	D 12	5	17459.0	B 5	23	17557.5	B 3	16	17678.4	B 2	14	17775.7	B 0	9	17879.9
B 7	33	17339.2	D 10	2	17461.0	B 2	10	17559.0	B 4	21	17680.9	D 17	21	17783.6	B 4	33	17883.9
D 14	7	17341.4	B 6	27	17463.2	D 16	13	17559.9	B 5	30	17682.1	D 15	14	17788.9	B 4	34	17886.5
B 7	34	17341.9	B 5	20	17463.4	D 12	6	17565.0	D 10	4	17686.7	D 13	10	17790.2	B 4	35	17888.0
B 7	35	17343.4	D 15	10	17468.9	D 8	0	17572.6	B 1	9	17686.9	B 4	25	17790.6	B 4	36	17888.7
B 7	36	17344.0	D 19	20	17471.0	B 4	18	17573.9	B 5	31	17690.0	D 10	5	17795.6	B 3	22	17898.5
D 10	1	17344.6	B 6	28	17478.1	D 10	3	17575.1	D 8	1	17691.0	B 3	19	17797.8	D 16	19	17900.9
B 6	22	17346.9	D 17	14	17478.3	B 5	24	17583.6	B 5	32	17695.9	D 14	12	17798.2	D 10	6	17901.6
D 12	4	17350.1	D 16	12	17482.2	B 3	14	17587.3	D 13	9	17698.5	D 8	2	17807.4	B 2	17	17908.8
B 5	17	17350.3	D 19	21	17484.1	D 18	19	17595.8	D 16	15	17698.9	B 1	11	17808.8	D 15	16	17916.4
B 4	13	17351.6	B 3	12	17485.3	D 13	8	17602.8	B 5	33	17700.0	B 4	26	17811.0	B 1	13	17916.9
D 19	17	17361.1	B 6	29	17490.6	D 17	16	17605.8	B 5	34	17702.6	B 0	8	17812.9	D 8	3	17921.5
B 6	23	17375.9	B 4	16	17492.2	B 5	25	17606.8	B 5	35	17704.1	D 16	17	17814.5	D 16	20	17924.4
D 15	9	17377.2	B 5	21	17497.0	B 4	19	17611.7	B 5	36	17704.8	B 2	15	17822.5	B 3	23	17927.5
B 5	18	17390.1	B 6	30	17500.6	B 2	11	17618.1	D 17	18	17708.5	B 4	27	17828.6	D 6	0	17928.7
D 18	15	17393.8	D 13	7	17503.3	D 18	20	17619.3	B 4	22	17712.3	B 3	20	17833.5	D 11	8	17934.4
D 9	0	17398.2	B 6	31	17508.4	B 1	8	17619.9	D 14	11	17715.6	D 11	7	17834.9	D 16	21	17937.5
D 16	11	17399.6	D 18	17	17509.5	D 11	5	17626.1	D 15	13	17716.6	B 4	28	17843.6	B 0	10	17942.7
D 13	6	17400.5	B 6	32	17514.3	B 5	26	17627.2	B 3	17	17720.3	D 15	15	17855.5	D 14	14	17948.2
B 4	14	17401.1	D 9	1	17516.6	D 14	10	17628.2	B 2	13	17726.2	B 4	29	17856.0	B 2	18	17948.6
B 6	24	17402.1	D 11	4	17517.2	D 16	14	17632.2	D 11	6	17732.0	D 9	4	17858.7	B 3	24	17953.7
D 11	3	17405.5	B 6	33	17518.4	D 18	21	17632.4	B 0	7	17741.3	D 16	18	17862.4	D 12	10	17954.7
D 17	13	17406.0	B 6	34	17521.1	D 9	2	17633.0	B 4	23	17741.4	D 12	9	17863.0	D 13	12	17960.2
D 19	18	17409.0	B 6	35	17522.6	B 3	15	17634.1	D 17	19	17746.9	B 1	12	17864.5	B 1	14	17966.5
B 6	25	17425.2	B 6	36	17523.2	D 15	12	17638.9	D 9	3	17747.1	B 4	30	17866.0	D 9	5	17967.6
B 5	19	17427.8	B 5	22	17528.4	B 5	27	17644.7	D 7	0	17749.5	B 2	16	17866.8	D 15	17	17971.2
B 3	11	17429.6	B 4	17	17534.2	B 4	20	17647.3	B 1	10	17749.7	B 3	21	17867.1	B 3	25	17976.8
D 14	8	17440.8	D 14	9	17536.6	B 5	28	17659.7	D 16	16	17759.8	D 7	1	17867.9	D 7	2	17984.3
B 6	26	17445.6	B 3	13	17537.7	D 17	17	17660.6	B 3	18	17760.1	B 4	31	17873.9	B 2	19	17986.3
D 19	19	17447.5	D 17	15	17545.0	D 12	7	17667.8	D 12	8	17767.3	D 14	13	17875.9	B 3	26	17997.2

Table B.5
Observed lines and assignments (Part I).

Line	Line Assignment	Other Lines	Line	Line Assignment	Other Lines
16431.7	22→10 D (16431.6)		16725.4	13→0 D (16725.0)	
16442.2	17→3 D (16442.1)		16729.6		
16453.6			16733.4		
16469.1	19→6 D (16469.1)		16736.4		
16483.3			16741.1		21→12 D (16741.0)
16519.2	22→11 D (16519.0)		16745.8		
16522.5	15→1 D (15522.2)		16753.8	15→3 D (16752.7)	22→14 D (16751.6)
16526.4	20→8 D (16526.0)				24→19 D (16751.0)
16534.3		25→17 D (16534.9)	16768.2	17→6 D (16768.6)	
16536.2				19→9 D (16767.2)	
16539.7			16775.9		24→20 D (16774.5)
16550.3		24→15 D (16549.0)	16789.5		
16554.1	17→4 D (16553.8)		16791.1		
16566.5			16797.9	14→2 D (16797.9)	23→17 D (16797.7)
16569.0			16801.3	20→11 D (16800.8)	
16571.5	19→7 D (16572.0)	21→10 D (16571.0)	16820.3	18→8 D (16819.8)	21→13 D (16818.7)
16576.8					22→15 D (16818.3)
16594.5			16832.6		
16597.8			16836.0		
16602.0	22→12 D (16601.6)		16843.5	13→1 D (16843.5)	23→18 D (16845.5)
16621.8	20→9 D (16621.8)	25→19 D (16621.2)	16859.3	19→10 D (16858.9)	
16638.9	15→2 D (16816.6)		16865.3	15→4 D (16864.3)	
16664.0	17→5 D (16662.6)	24→17 D (16664.6)	16871.3	17→7 D (16871.5)	9→24 B (16871.6)
16671.5	19→8 D (16671.5)		16876.9		
16680.2	14→1 D (16681.5)	23→15 D (16682.0)	16879.9	22→16 D (16879.1)	
	22→13 D (16679.3)		16884.1	20→12 D (16883.4)	23→19 D (16884.0)
16696.6			16891.8		
16704.5			16899.0		
16709.3		16→4 D (16707.7)	16912.3	14→3 D (16912.0)	
16714.1	20→10 D (16713.4)	24→18 D (16712.5)	16915.3	18→9 D (16915.5)	
16719.6	18→7 D (16720.3)		16920.0		23→21 D (16920.6)

Table B.6
Observed lines and assignments (Part II).

Line	Line Assignment	Other Lines	Line	Line Assignment	Other Lines
16926.8			17110.0		
16933.3	22→17 D (16933.9)	9→27 B (16932.7)	17113.1		
16939.3			17125.3	12→2 D (17124.4)	16→8 D (17124.9)
16946.3	19→11 D (16946.2)	9→28 B (16947.7)	17133.0	14→5 D (17132.6)	
16954.9			17138.8		7→21 B (17136.3)
16958.1		21→15 D (16857.6)	17153.7		8→31 B (17152.4)
16961.4	13→2 D (16959.9)	9→29 B (16960.1)	17158.1	17→10 D (17158.3)	21→19 D (17159.6)
	20→13 D (16961.1)			20→16 D (17160.9)	
16971.6	17→8 D (16970.9)	9→30 B (16970.1)	17164.3		
	15→5 D (16973.2)		17168.7		6→17 B (17168.7)
16979.4		9→31 B (16977.9)	17175.3	11→1 D (17177.2)	
16985.9			17181.9	15→7 D (17182.0)	21→20 D (17183.1)
16994.6			17186.8	13→4 D (17185.6)	
17008.0	12→1 D (17008.0)		17190.8		
	18→10 D (17007.2)		17203.2		
17015.9			17212.6		20→17 D (17215.7)
17020.2	22→19 D (17020.2)	8→23 B (17019.9)	17226.3	10→0 D (17226.2)	
17022.4	14→4 D (17023.7)		17232.7		5→9 C (17232.0)
17029.8	19→12 D (17028.8)		17239.1	12→3 D (17238.5)	
17031.9				14→6 D (17238.5)	
17034.6	20→14 D (17033.4)		17246.9	19→15 D (17245.5)	7→25 B (17246.0)
17041.1				17→11 D (17245.7)	6→19 B (17246.2)
17051.1			17250.8		
17056.8	11→0 D (17056.6)	22→21 D (17056.8)	17256.6		
17067.1	17→9 D (17066.6)	7→19 B (16067.0)	17260.9		
		8→25 B (17069.2)	17268.4		
17074.2	13→3 D (17074.0)	21→17 D (17073.3)	17274.2		
17079.9	15→6 D (17079.2)		17281.7	15→8 D (17281.5)	6→20 B (17281.9)
17095.2	18→11 D (17094.5)		17283.5		7→27 B (17284.0)
17101.8		20→15 D (17100.1)	17286.0		
17107.8	19→13 D (17106.5)	7→20 B (17102.7)	17291.4	11→2 D (17291.4)	

Table B.7
Observed lines and assignments (Part III).

Line	Line Assignment	Other Lines	Line	Line Assignment	Other Lines
17294.6	13→5 D (17294.5)				6→28 B (17478.1)
17301.8	20→19 D (17302.1)		17482.0		16→16 D (17482.2)
17307.4		19→16 D (17306.4)	17485.7	3→12 B (17485.3)	19→21 D (17484.1)
		5→16 B (17308.3)	17489.6		
17313.3		16→10 D (17312.3)	17492.3	4→16 B (17492.2)	
17320.1		7→30 B (17321.4)	17496.5	5→21 B (17497.0)	3→8 C (17496.2)
17328.7	17→12 D (17328.3)	18→14 D (17327.2)	17502.7	13→7 D (17503.3)	
		7→31 B (17329.2)	17508.8	18→17 D (17509.5)	6→31 B (17508.4)
17336.7		7→32 B (17335.1)	17510.7		
		20→21 D (17338.7)	17512.1		
		7→33 B (17339.2)	17516.9	9→1 D (17516.6)	11→4 D (17517.2)
		5→10 C (17336.8)	17519.3		
17340.3		7→33 B (17339.2)	17520.7		6→33 B (17518.4)
17349.9	12→4 D (17350.1)	5→17 B (17350.3)			4→10 C (17520.7)
		4→13 B (17351.6)	17533.8	4→17 B (17534.2)	
17361.1	19→17 D (17361.1)		17537.2	3→13 B (17537.7)	
17365.1				14→9 D (17536.6)	
17377.4	15→9 D (17377.2)	6→23 B (17375.9)	17546.7		17→15 D (17545.0)
17380.0			17556.9	15→11 D (17556.2)	
17390.1	5→18 B (17390.1)			18→18 D (17557.3)	
17394.0	18→15 D (17393.8)			5→23 B (17557.5)	
17400.9	13→6 D (17400.5)	16→11 D (17399.6)	17565.0	12→6 D (17565.0)	
	4→14 B (17400.1)		17574.3	4→18 B (17573.9)	10→3 D (17575.1)
		6→24 B (17402.1)			8→0 D (17572.6)
17406.3	17→13 D (17406.0)		17579.4		
17416.1			17588.0		
17427.8	5→19 B (17427.8)		17591.3		
17440.6	14→8 D (17440.8)	5→11 C (17440.8)	17602.4	13→8 D (17602.8)	3→9 C (17602.1)
17447.9	4→15 B (17447.9)	19→19 D (17447.5)	17605.8	17→16 D (17605.8)	
17479.7		17→14 D (17478.3)	17618.5	2→11 B (17618.1)	18→20 D (17619.3)

Table B.8
Observed lines and assignments (Part IV).

Line	Line Assignment	Other Lines	Line	Line Assignment	Other Lines
17624.6		4→11 C (17624.7)	17747.9		
17626.5		11→5 D (17626.1)	17750.1	7→0 D (17749.5)	1→10 B (17749.7)
		5→26 B (17627.2)	17755.1		
17629.5		14→10 D (17628.2)	17758.9		
17633.9	3→15 B (17634.1)	16→14 D (17632.2)	17760.1	3→18 B (17760.1)	16→16 D (17559.8)
	9→2 D (17633.0)	18→21 D (17632.4)	17767.0	12→8 D (17767.3)	
17639.9	15→12 D (17638.9)			4→24 B (17767.5)	
17644.3		5→27 B (17644.7)	17776.0	2→14 B (17775.7)	
17646.6		4→20 B (17647.3)	17778.4		
17648.5		4→20 B (17647.3)	17783.0		17→21 D (17783.6)
17660.0	17→17 D (17660.6)	5→28 B (17659.7)	17790.5	13→10 D (17790.2)	15→14 D (17788.9)
17662.4				4→25 B (17790.6)	
17665.1			17797.4	14→12 D (17798.2)	
17667.8	12→7 D (17667.8)			3→19 B (17797.8)	
17673.4	2→12 B (17673.7)			10→5 D (17795.6)	
17674.9	3→16 B (17678.4)		17803.5		
17679.2			17807.7		8→2 D (17807.4)
17686.2	10→4 D (17686.7)	1→9 B (17686.9)	17809.1		1→11 D (17808.8)
17689.7		5→31 B (17690.0)	17810.7	4→26 B (17811.0)	3→11 C (17810.9)
17691.0		8→1 D (17691.0)	17822.4	2→15 B (17822.5)	
17698.1	13→9 D (17698.5)	16→15 D (17698.9)	17826.6		
17707.2	17→18 D (17708.5)	3→10 C (17706.9)	17828.8	4→27 B (17828.6)	
17713.1			17834.6	11→7 D (17834.6)	
17717.5	15→13 D (17716.6)	14→11 D (17715.6)		3→20 B (17833.5)	
17722.6			17840.1		
17725.9	2→13 B (17726.2)		17851.5		
17732.2	11→6 D (17732.0)		17856.9		15→15 D (17855.5)
17742.5					4→29 B (17856.0)
17747.1	9→3 D (17747.1)		17858.8	9→4 D (17858.7)	
	17→19 D (17746.9)		17861.1		

Table B.9
Observed lines and assignments (Part V).

Line	Line Assignment	Other Lines	Line	Line Assignment	Other Lines
17867.6	7→1 D (17867.9)	4→30 B (17866.0)	17934.9	11→8 D (17934.3)	
	3→21 B (17867.1)		17948.6	14→14 D (17948.2)	
	2→16 B (17866.8)			2→18 B (17948.6)	
17877.4	13→11 D (17877.5)	14→13 D (17875.9)	17954.4	12→10 D (17954.7)	3→24 B (17953.7)
17886.6		4→34 B (17668.5)	17961.4	13→12 D (17960.2)	
17893.9			17964.5		
17895.7			17967.8	9→5 D (17967.6)	1→14 B (17966.5)
17898.3	3→22 B (17898.5)		17970.9	15→17 D (17971.2)	
17902.2	10→6 D (17901.6)	16→19 D (17900.9)	17984.5	7→2 D (17984.3)	
17905.3			17999.0		
17908.1	2→17 B (17908.8)				

Table B.10
Observed progressions in REMPI spectra.

D ¹ Π	11→0	12→10	13→12	15→3	17→5	18→7	19→11	20→19	2→15	4→14*
7→0	11→1	13→0	14→1*	15→4	17→6*	18→8	19→12	22→10	2→16*	4→15
7→1*	11→2	13→1	14→2	15→5*	17→7	18→9	19→13	22→11	2→17	4→16
7→2	11→6	13→2*	14→3	15→6	17→8*	18→10*	19→15*	22→12	2→18*	4→17
9→1	11→7*	13→3	14→4	15→7	17→9	18→11	19→17	22→13*	3→12	4→18
9→2	11→8	13→4	14→5	15→8	17→10*	18→15	20→8	22→16	3→13*	4→24*
9→3*	12→1*	13→5	14→6*	15→9	17→11*	18→17	20→9	22→17	3→15	4→25*
9→4	12→2	13→6*	14→8	15→11*	17→12	18→18*	20→10	22→19	3→16	4→26
9→5	12→3*	13→7	14→9*	15→12	17→13	19→6	20→11	B ¹ Π	3→18	4→27
10→0	12→4	13→8	14→12*	15→13	17→16	19→7	20→12	2→11	3→19*	5→18
10→4	12→6	13→9	14→14*	15→17	17→17	19→8	20→13*	2→12	3→20*	5→19
10→5*	12→7	13→10*	15→1	17→3	17→18	19→9*	20→14	2→13	3→21*	5→21
10→6	12→8*	13→11	15→2	17→4	17→19*	19→10	20→16*	2→14	3→22	5→23*

LIST OF REFERENCES

LIST OF REFERENCES

- [1] L. D. Carr, D. DeMille, R. V. Krems, and J. Ye, *New Journal of Physics* **11**, 055049 (2009).
- [2] K. Aikawa et al., *New J. Phys.* **11**, 055035 (2009).
- [3] K. Aikawa et al., *Physical Review Letters* **105**, 203001 (2010).
- [4] J. Banerjee et al., *Phys. Rev. A* **86**, 053428 (2012).
- [5] T. Bergeman, A. J. Kerman, J. Sage, S. Sainis, and D. DeMille, *European Physical Journal D* **31**, 179 (2004).
- [6] J. Deiglmayr et al., *Physical Review Letters* **101**, 133004 (2008).
- [7] J. Deiglmayr et al., *New Journal of Physics* **11**, 055034 (2009).
- [8] J. Deiglmayr et al., *Faraday Discuss.* **142**, 335 (2009).
- [9] J. Deiglmayr et al., *New Journal of Physics* **12**, 079802 (2010).
- [10] J. Deiglmayr et al., *Journal of Physics: Conference Series* **264**, 012014 (2011).
- [11] D. DeMille, *Physical Review Letters* **88**, 067901 (2002).
- [12] S. Dutta, D. S. Elliott, and Y. P. Chen, *EPL (Europhysics Letters)* **104**, 63001 (2013).
- [13] S. Dutta, J. Lorenz, A. Altaf, D. S. Elliott, and Y. P. Chen, *Phys. Rev. A* **89**, 020702 (2014).
- [14] J. K. Freericks et al., *Physical Review A* **81**, 011605 (2010).
- [15] A. Grochola et al., *Journal of Chemical Physics* **131**, 054304 (2009).
- [16] C. Haimberger, J. Kleinert, P. Zabawa, A. Wakim, and N. P. Bigelow, *New Journal of Physics* **11** (2009).
- [17] A. J. Kerman, J. M. Sage, S. Sainis, T. Bergeman, and D. DeMille, *Phys. Rev. Lett.* **92**, 033004 (2004).
- [18] J. Kleinert, C. Haimberger, P. J. Zabawa, and N. P. Bigelow, *Physical Review Letters* **99**, 143002 (2007).
- [19] E. Kuznetsova, M. Gacesa, P. Pellegrini, S. F. Yelin, and R. Côté, *New Journal of Physics* **11**, 055028 (2009).
- [20] M. Marinescu and H. R. Sadeghpour, *Phys. Rev. A* **59**, 390 (1999).

- [21] K.-K. Ni et al., *Science* **322**, 231 (2008).
- [22] S. Ospelkaus et al., *Nature Physics* **4**, 622 (2008).
- [23] S. Ospelkaus et al., *Science* **327**, 853 (2010).
- [24] P. Pellegrini, M. Gacesa, and R. Cote, *Physical Review Letters* **101**, 053201 (2008).
- [25] A. Ridinger et al., *Europhysics Letters* **96** (2011).
- [26] S. D. Kraft et al., *J. Phys. B-atomic Mol. Opt. Phys.* **39**, S993 (2006).
- [27] J. M. Sage, S. Sainis, T. Bergeman, and D. DeMille, *Physical Review Letters* **94**, 203001 (2005).
- [28] E. S. Shuman, J. F. Barry, and D. DeMille, *Nature* **467**, 820 (2010).
- [29] B. K. Stuhl, B. C. Sawyer, D. Wang, and J. Ye, *Phys. Rev. Lett.* **101** (2008).
- [30] W. C. Stwalley, *European Physical Journal D* **31**, 221 (2004).
- [31] W. C. Stwalley, M. Bellos, R. Carollo, J. Banerjee, and M. Bermudez, *Molecular Physics* **110**, 1739 (2012).
- [32] J. Ulmanis, J. Deiglmayr, M. Repp, R. Wester, and M. Weidemüller, *Chemical Reviews* **112**, 4890 (2012).
- [33] D. Wang et al., *Physical Review A* **81**, 061404 (2010).
- [34] D. Wang et al., *Phys. Rev. Lett.* **93**, 243005 (2004).
- [35] H. Wang and W. C. Stwalley, *J. Chem. Phys.* **108**, 5767 (1998).
- [36] P. Zabawa, A. Wakim, M. Haruza, and N. P. Bigelow, *Phys. Rev. A* **84**, 061401 (2011).
- [37] P. S. Zuchowski and J. M. Hutson, *Physical Review A* **81**, 060703 (2010).
- [38] S. Dutta, A. Altaf, D. S. Elliott, and Y. P. Chen, *Chemical Physics Letters* **511**, 7 (2011).
- [39] M. Ivanova, A. Stein, A. Pashov, H. Knockel, and E. Tiemann, *J. Chem. Phys.* **134**, 024321 (2011).
- [40] M. Ivanova, A. Stein, A. Pashov, H. Knockel, and E. Tiemann, *The Journal of Chemical Physics* **138**, 094315 (2013).
- [41] M. Gehm, Properties of ^6Li , <http://www.phy.duke.edu/research/photon/optics/techdocs/>, 2003.
- [42] J. P. Gordon and A. Ashkin, *Physical Review A* **21**, 1606 (1980).
- [43] J. Dalibard and C. Cohentannoudji, *J. Opt. Soc. Am. B-optical Phys.* **2**, 1707 (1985).

- [44] J. Dalibard and C. Cohentannoudji, *J. Opt. Soc. Am. B-optical Phys.* **6**, 2023 (1989).
- [45] W. Ketterle, K. B. Davis, M. A. Joffe, A. Martin, and D. E. Pritchard, *Physical Review Letters* **70**, 2253 (1993).
- [46] P. D. Lett et al., *Physical Review Letters* **61**, 169 (1988).
- [47] P. D. Lett et al., *J. Opt. Soc. Am. B-optical Phys.* **6**, 2084 (1989).
- [48] C. Monroe, W. Swann, H. Robinson, and C. Wieman, *Physical Review Letters* **65**, 1571 (1990).
- [49] C. G. Townsend et al., *Phys. Rev. A* **52**, 1423 (1995).
- [50] P. J. Ungar, D. S. Weiss, E. Riis, and S. Chu, *J. Opt. Soc. Am. B-optical Phys.* **6**, 2058 (1989).
- [51] D. S. Weiss, E. Riis, Y. Shevy, P. J. Ungar, and S. Chu, *J. Opt. Soc. Am. B-optical Phys.* **6**, 2072 (1989).
- [52] A. L. Migdall, J. V. Prodan, W. D. Phillips, T. H. Bergeman, and H. J. Metcalf, *Physical Review Letters* **54**, 2596 (1985).
- [53] P. D. Lett et al., *Phys. Rev. Lett.* **71**, 2200 (1993).
- [54] F. Masnou-Seeuws and P. Pillet, *Advances In Atomic, Molecular, Optical Physics* **47**, 53 (2001).
- [55] A. Altaf, *Spectroscopy of ultracold LiRb molecules using ionization detection*, PhD thesis, Purdue University, 2014.
- [56] C. Chin, R. Grimm, P. Julienne, and E. Tiesinga, *Review of Modern Physics* **82**, 1225 (2010).
- [57] J. D. Jackson, *Classical Electrodynamics*, Wiley, 3rd edition, 1998.
- [58] I. V. Litvinyuk et al., *Phys. Rev. Lett.* **90**, 233003 (2003).
- [59] E. Gershnabel and I. S. Averbukh, *Phys. Rev. Lett.* **104**, 153001 (2010).
- [60] H. Soifer et al., *Phys. Rev. Lett.* **105**, 143904 (2010).
- [61] S. Fleischer, Y. Zhou, R. W. Field, and K. A. Nelson, *Phys. Rev. Lett.* **107**, 163603 (2011).
- [62] M. Lu, N. Q. Burdick, S. H. Youn, and B. L. Lev, *Physical Review Letters* **107** (2011).
- [63] C. Gerry and P. Knight, *Introductory Quantum Optics*, Cambridge University Press, 2005.
- [64] D. Kielpinski, C. Monroe, and D. J. Wineland, *Nature* **417**, 709 (2002).
- [65] R. P. Feynman, *Int. J. Theoretical Phys.* **21**, 467 (1982).

- [66] D. Deutsch and R. Jozsa, Proc. Royal Soc. London Series A-mathematical Phys. Engineering Sciences **439**, 553 (1992).
- [67] *Proceedings of the 35th Symposium on Foundations of Computer Science, Los Alamitos*, 1994.
- [68] L. M. K. Vandersypen et al., Nature **414**, 883 (2001).
- [69] M. L. Bellac, *A Short Introduction to Quantum Information and Quantum Computation*, Cambridge University Press, 2006.
- [70] A. Lupascu, C. J. M. Verwijs, R. N. Schouten, C. J. P. M. Harmans, and J. E. Mooij, Phys. Rev. Lett. **93**, 177006 (2004).
- [71] E. Urban et al., Nat. Phys. **5**, 110 (2009).
- [72] K.-A. B. Soderberg, N. Gemelke, and C. Chin, New Journal of Physics **11** (2009).
- [73] A. S. Arnold, J. S. Wilson, and M. G. Boshier, Rev. Scientific Instruments **69**, 1236 (1998).
- [74] C. C. Bradley, J. Chen, and R. G. Hulet, Rev. Scientific Instruments **61**, 2097 (1990).
- [75] S. Dutta, D. Elliott, and Y. Chen, Applied Physics B **106**, 629 (2012).
- [76] C. J. Hawthorn, K. P. Weber, and R. E. Scholten, Rev. Scientific Instruments **72**, 4477 (2001).
- [77] G. P. T. Lancaster, W. Sibbett, and K. Dholakia, Rev. Scientific Instruments **71**, 3646 (2000).
- [78] K. G. Libbrecht and J. L. Hall, Rev. Scientific Instruments **64**, 2133 (1993).
- [79] K. B. Macadam, A. Steinbach, and C. Wieman, Am. J. Phys. **60**, 1098 (1992).
- [80] C. E. Wieman and L. Hollberg, Rev. Scientific Instruments **62**, 1 (1991).
- [81] M. Aymar and O. Dulieu, Journal of Chemical Physics **122**, 204302 (2005).
- [82] M.-S. Heo et al., Phys. Rev. A **86**, 021602 (2012).
- [83] S. Dutta, *Experimental Studies of LiRb: Spectroscopy and Ultracold Molecule Formation by Photoassociation*, PhD thesis, Purdue University, 2013.
- [84] C.-H. Wu, J. W. Park, P. Ahmadi, S. Will, and M. W. Zwierlein, Phys. Rev. Lett. **109**, 085301 (2012).
- [85] R. Ferber et al., The Journal Of Chemical Physics **128** (2008).
- [86] G. N. Price, S. T. Bannerman, K. Viering, E. Narevicius, and M. G. Raizen, Physical Review Letters **100** (2008).
- [87] A. Mills, *Nonlinear ground state pump-probe spectroscopy in ultracold rubidium: Raman-coupled dressed state spectroscopy*, PhD thesis, Purdue University, 2007.

- [88] J. R. de Laeter et al., *Pure and Applied Chemistry* **75**, 1365 (2003).
- [89] K. Ladouceur et al., *Journal of Optical Society of America B* **26**, 210 (2009).
- [90] D. A. Steck, Rubidium 85 D line data, <http://steck.us/alkalidata/>, 2010.
- [91] J. Walls, R. Ashby, J. Clarke, B. Lu, and W. van Wijngaarden, *The European Physical Journal D - Atomic, Molecular, Optical And Plasma Physics* **22**, 159 (2003).
- [92] K. Strecker, *Tunable Interaction in Quantum Degenerate Lithium*, PhD thesis, Rice University, 2004.
- [93] K. E. Gibble, S. Kasapi, and S. Chu, *Optics Letters* **17**, 526 (1992).
- [94] S. Dutta, A. Altaf, J. Lorenz, D. S. Elliott, and Y. P. Chen, *Journal of Physics B: Atomic, Molecular and Optical Physics* **47**, 105301 (2014).
- [95] A. Yariv, *Quantum Electronics*, Wiley, 1989.
- [96] D. Antypas, *Spectroscopy of ultracold LiRb molecules using ionization detection*, PhD thesis, Purdue University, 2013.
- [97] J. Goldwin, S. B. Papp, B. DeMarco, and D. S. Jin, *Phys. Rev. A* **65**, 021402 (2002).
- [98] G. Ferrari, M.-O. Mewes, F. Schreck, and C. Salomon, *Opt. Lett.* **24**, 151 (1999).
- [99] J. L. Booth, J. V. Dongen, P. Lebel, B. G. Klappauf, and K. W. Madison, *J. Opt. Soc. Am. B* **24**, 2914 (2007).
- [100] H. S. Margolis, *Chem. Soc. Rev.* **41**, 5174 (2012).
- [101] C. Gabbanini, A. Fioretti, A. Lucchesini, S. Gozzini, and M. Mazzoni, *Phys. Rev. Lett.* **84**, 2814 (2000).
- [102] A. R. L. Caires, V. A. Nascimento, D. C. J. Rezende, V. S. Bagnato, and L. G. Marcassa, *Phys. Rev. A* **71**, 043403 (2005).
- [103] E. Flaxler, *Meas. Sci. Technol.* **17**, N37 (2006).
- [104] J. Kleinert, C. Haimberger, P. J. Zabawa, and N. P. Bigelow, *Review of Scientific Instruments* **78**, 113108 (2007).
- [105] M. Korek et al., *Chemical Physics* **256**, 1 (2000).
- [106] M. Korek, G. Younes, and S. Al-Shawa, *Journal of Molecular Structure: THEOCHEM* **899**, 25 (2009).
- [107] M. Movre and R. Beuc, *Phys. Rev. A* **31**, 2957 (1985).
- [108] B. Bussery, Y. Achkar, and M. Aubert-Frécon, *Chemical Physics* **116**, 319 (1987).
- [109] R. J. Leroy and R. B. Bernstein, *Chemical Physics Letters* **5**, 42 (1970).

- [110] C. Zener, Proc. R. Soc. Lond. A **137**, 696 (1932).
- [111] L. Landau, Phys. Z. **2**, 46 (1932).
- [112] G. Herzberg, *Spectra of Diatomic Molecules*, D. Van Nostrand Company, Inc, 2nd edition, 1950.
- [113] A. Kramida, Yu. Ralchenko, J. Reader, and NIST ASD Team, NIST Atomic Spectra Database (ver. 5.1), [Online]. Available: <http://physics.nist.gov/asd> [2014, May 26]. National Institute of Standards and Technology, Gaithersburg, MD., 2013.
- [114] L. von Szentpály, P. Fuentealba, H. Preuss, and H. Stoll, Chemical Physics Letters **93**, 555 (1982).
- [115] S. Azizi, *Etude des propriétés électroniques de dimères d'alcalins. Application à la formation de molécules froides.*, PhD thesis, Université Paris Sud, 2013.
- [116] R. J. L. Roy, Level 8.0: *A Computer Program for Solving the Radial Schrödinger Equation for Bound and Quasibound Levels*, University of Waterloo Chemical Physics Research Report CP-663 (2007); see [http://leroy.uwaterloo.ca/programs/.](http://leroy.uwaterloo.ca/programs/), 2007.
- [117] H.-C. Naegerl et al., 22nd International Conference On Atomic Physics **264**, 012015 (2011).
- [118] M. M. Somoza, Depiction of Franck Condon principle in absorption and fluorescence., <http://en.wikipedia.org/wiki/File:Franck-Condon-diagram.png>, 2006.

VITA

VITA

John Lorenz was born in Covington, Kentucky in 1983. He graduated from Covington Catholic High School in 2002. He received a B.S. in Physics and Mathematics from the University of Louisville in 2006. His focus in those respective subjects was Computational Physics and Pure Mathematics. He received an M.S. in Physics from Purdue University in 2011. The focus of his PhD work was cold atom and molecule experiments and molecular spectroscopy. His teaching activities included acting as co-instructor for both calculus and algebra based introductory electricity and magnetism courses and as a teaching assistant for the introductory mechanics for incoming Physics majors.